

STRANGE PARTICLE PRODUCTION IN  $\pi^+p$  INTERACTIONS

AT 4 GEV/C

BY

JANET MARGOT BROWNLEE

A Thesis presented for the degree  
of Doctor of Philosophy in the  
University of London.

Department of Physics,  
Imperial College of Science and Technology,  
London, S.W.7.

May 1965

## ABSTRACT

This thesis presents a study of the strange particle production in  $\pi^+p$  interactions at an incident pion momentum of 4 Gev/c. The Saclay 81 cms. liquid hydrogen bubble chamber was exposed to a beam from the CERN proton synchrotron and 70,000 pictures were obtained. The analysis of those events with at least one observed strange particle decay is presented, with reference to the non-strange interactions at this energy.

Chapter 1 reviews the background to the experiment. In Chapter 2 an account is given of the apparatus and processes used to analyse the events. Chapters 3 and 4 describe the methods used to analyse the  $V^0$  and charged V events. Cross-sections results and a brief discussion of the strange particle events with four charged secondaries are considered in Chapter 5. In Chapter 6 all the strange particle reactions with two charged secondaries are considered in detail and in Chapter 7 details of the Gottfried and Jackson analysis are given and the results for two reactions considered.

Finally in Chapter 8, the Buddha meson and the possible  $K\bar{K}$  decay modes of non-strange mesonic resonances are discussed.

CONTENTS

	<u>Page</u>
CHAPTER 1	
<u>BACKGROUND TO THE EXPERIMENT</u>	
1.1 Introduction.	4
1.2 Earlier experiments studying strange particle production in $\pi^+p$ interactions.	5
1.3 The 4 Gev/c $\pi^+p$ experiment.	7
1.4 The experimental observation of Resonances.	10
1.5 The quantum numbers of Resonances.	12
CHAPTER 2	
<u>EXPERIMENTAL PROCEDURE</u>	
2.1 Introduction.	15
2.2 The Beam	15
2.3 The Hydrogen Bubble Chamber.	16
2.4 Scanning Procedure.	17
2.5 Measurement of Events.	20
2.6 Data Processing.	22
CHAPTER 3	
<u>INTERPRETATION OF EVENTS WITH ONE OR TWO <math>V^0</math>'S</u>	
3.1 The Fiducial Volume.	32
3.2 Scanning Efficiencies.	33
3.3 Use of Ionization in the identification of tracks.	35
3.4 Probability of ( $\chi^2$ ) distribution for $V^0$ events.	36

	<u>Page</u>
3.5 Scanning Biases for $V^0$ events.	38
3.6 The analysis of 201 events.	39
3.7 Analysis of 202 and 401 events.	41

CHAPTER 4

INTERPRETATION OF EVENTS WITH ONE OR TWO CHARGED V'S

4.1 Introduction.	53
4.2 Probability of ( $\chi^2$ ) distributions.	53
4.3 Scanning Losses for $V^\pm$ events.	54
4.4 Lifetime plots for charged V's.	57
4.5 The analysis of the event types 210, 220, 211.	57
4.6 The analysis of $41^\pm 0$ , $41^\pm 1$ , $42^{\pm\pm} 0$ events.	59
4.7 Ambiguous events.-	60

CHAPTER 5

CROSS-SECTION CALCULATIONS FOR STRANGE PARTICLE PRODUCTION

5.1 The determination of the weights.	70
5.2 Corrections for $V^0$ events.	71
5.3 Corrections for $V^\pm$ events.	73
5.4 Cross-section determinations.	75
5.5 Strange particle production in 4 Gev/c $\pi^+p$ and $\pi^-p$ interactions.	77
5.6 The 4-prong strange particle reactions.	78

	<u>Page</u>
CHAPTER 6	<u>DISCUSSION OF TWO PRONG STRANGE PARTICLE REACTIONS</u>
6.1	The reaction $\pi^+ p \rightarrow K^+ \pi^+ \lambda \pi^0$ 82
6.2	The reaction $\pi^+ p \rightarrow \pi^+ \pi^+ \lambda \pi^0$ 86
6.3	The reaction $\pi^+ p \rightarrow p \pi^+ K^0 \bar{K}^0$ 88
6.4	The reaction $\pi^+ p \rightarrow \Sigma^+ \pi^0 K^+$ 90
CHAPTER 7	<u>EXCHANGE MECHANISMS</u>
7.1	Introduction. 110
7.2	Gottfried and Jackson analysis. 111
7.3	The reaction $\pi^+ p \rightarrow N^{*++} + \rho^0$ 114
7.4	The reaction $\pi^+ p \rightarrow N^{*++} + \omega^0$ 119
7.5	The effect of Absorption on the peripheral model. 123
CHAPTER 8	<u>K<math>\bar{K}</math> DECAY MODES OF SOME NON-STRANGE MESONIC RESONANCES</u>
8.1	Introduction. 140
8.2	The Buddha meson. 141
8.3	The reaction $\pi^+ p \rightarrow p B^+$ . 142
8.4	The determination of the spin and parity of the Buddha. 144
8.5	The search for the decay mode $B \rightarrow 2\pi$ . 146
8.6	The search for the $K\bar{K}$ decay mode of the B-meson. 147
8.7	The observation of the decay mode $A_2 \rightarrow K\bar{K}$ . 150
	ACKNOWLEDGEMENTS. 158
	REFERENCES. 159
	FIGURE CAPTIONS. 163

## CHAPTER 1

### BACKGROUND TO THE EXPERIMENT

#### 1.1 Introduction

Strange particle production has been studied in 4 GeV/c  $\pi^+$ p interactions in order to determine the cross sections which are unknown in this energy region. It was also possible within the limited statistics, to study the production of resonances and the possible exchange mechanisms producing quasi-two body final states. Quasi-two body final states are those with three or more particles, where one or more resonances are formed, in such a way that it is possible to consider them as two-body final states.

It is of interest to compare the results with those found in the  $\pi^-$ p interactions <sup>(1)</sup> at the same energy. The resonance production is much more copious in the  $\pi^+$ p interactions than in the  $\pi^-$ p interactions. This observation was not entirely expected. The  $\pi^-$ p system is in a pure isospin state of  $I = 3/2$ , while the  $\pi^+$ p system is a mixed  $I = 1/2, 3/2$  state. It is perhaps possible to argue that although this restricts the number of resonances that can be produced in  $\pi^+$ p interactions, the number of channels is decreased so that the statistics are improved.

This work constitutes a small part of the whole 4 GeV/c  $\pi^+$ p experiment, so that the data relevant to the possible

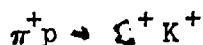
production mechanisms is considered with some of the other results obtained in this experiment (2-9).

It was found that the quasi-two body final states could generally be described by the peripheral model (10), (one meson exchange). It was a feature of the strange particle production processes that these were less peripheral than those where non-strange resonances were produced. In fact the peripheral process only explains some of the results and some other model has to be invoked to describe the rest, a possibility is the statistical model (11, 12). In this thesis only the peripheral processes are considered.

## 1.2 Earlier experiments studying strange particle production in $\pi^+p$ interactions

Although there is a large quantity of published data for strange particle production in  $\pi^-p$  interactions over a wide range of energies (14), few results have been published for the production of strange particles in  $\pi^+p$  collisions.

Most of the available results are for incident  $\pi^+$  momenta of 1 - 1.5 GeV/c (15), where the only available reaction is



which enabled the behaviour at the  $\Sigma^+K^+$  threshold to be studied

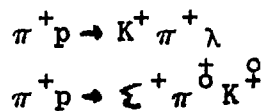
and the triangular inequalities

$$\sqrt{\frac{d\sigma(\pi^+ p \rightarrow \xi^+ K^+)}{d\Omega}} + \sqrt{\frac{d\sigma(\pi^+ p \rightarrow \xi^- K^+)}{d\Omega}} \geq \sqrt{\frac{2d\sigma(\pi^- p \rightarrow \xi^0 K^0)}{d\Omega}}$$

to be verified.

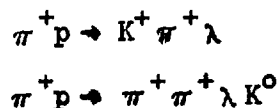
At higher energies, results are available for only three experiments at incident  $\pi^+$  momenta of 2.08 <sup>(16)</sup>, 2.77 <sup>(17)</sup> and 3.55 <sup>(18)</sup> GeV/c; all these experiments determine the cross-sections for the possible three and four body final states, but results for resonance production are presented for the first two energies only.

At 2.08 GeV/c <sup>(16)</sup> the available centre of mass energy is such that three body final states



can also be discussed. Strong  $Y_1^*$  (1385) <sup>(19)</sup> production was found in the first of these reactions and strong  $K^*$  (888) <sup>(20)</sup> in the others but there was not sufficient data for the exchange mechanisms for these reactions to be determined.

Both three and four body final states are possible at 2.77 GeV/c <sup>(17)</sup> and it is possible to describe the reactions in terms of the peripheral model. The reactions



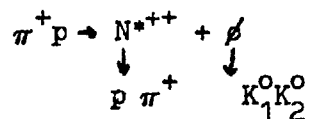
were dominated by strong  $Y_1^*$  (1385) production, while  $K^*$ (888)

was copiously produced in the reactions

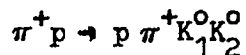


where the exchange mechanism was found to be an equal mixture of K and K\* exchange, in agreement with the results of Smith et al. (20).

There was also some evidence for the reaction



which was observed in the channel



where 66% of the events lay in the overlap region for the N\*<sup>++</sup> and the  $\phi$  bands on the Dalitz plot.

### 1.3 The 4 GeV/c $\pi^+ p$ Experiment

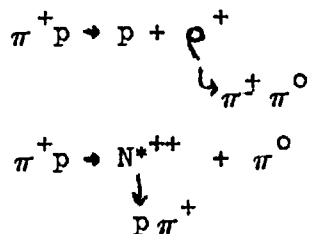
This experiment was carried out in collaboration with six other departments in Aachen, Berlin, Birmingham, Bonn, Hamburg and Munich.

Altogether 9231 events with two charged secondary particles, 6655 events with four charged secondaries, and 1063 strange particle events have been analysed and the results published (2-9).

Nearly all the possible interactions are dominated by

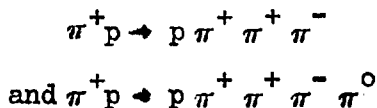
strong resonance formation; in most cases it is possible to describe these processes by the peripheral model.

In the non-strange reactions with two charged secondaries, copious  $N^{*++}$  (1238) (21) and  $\rho^0$  (22) production was seen; and it was possible to determine the exchange mechanisms operating for the two reactions

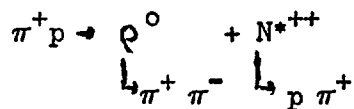


which were almost pure  $\pi$  and  $\rho$  exchange respectively (3,7).

In reactions with four charged secondaries, there were two important reactions. These were

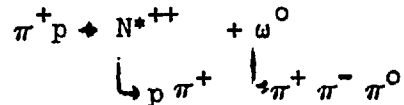


The first of these was dominated by  $\rho$  and  $N^{*++}$  formation, some 20% of which was by associated production of these two resonances. It was possible to determine that  $\pi$ -exchange was the responsible mechanism for the reaction



and this will be discussed in detail in Chapter 7 (8). The  $f^0$  was also seen associated with  $N^{*++}$  production.

It was also in this reaction that the  $\rho\pi$  enhancement observed by Goldhaber (23) was resolved into two distinguishable resonances, the  $A_1$  at 1090 Mev and the  $A_2$  at 1310 Mev, both of which were produced preferentially with low momentum transfer to the proton. In the second of these two reactions there was copious  $N^{*++}$  and  $\omega^0$  (24) production and some  $\eta$  formation (26). 10% of the events were of the channel



but an attempt to determine the exchange mechanisms gave inconclusive results; this will be discussed in Chapter 7 (8).

There was also some B-meson production (25) and the attempt to determine its spin and parity will be discussed in Chapter 8 (9), together with the results for the search for the  $K\bar{K}$  decay modes of some non-strange mesonic resonances.

The strange particles reactions are discussed in detail in the following chapters. These reactions are dominated by  $Y_1^*$  (1385) and  $K^*(888)$  production, but there is some evidence for the production of the  $K^*(1400)$  (64, 65). It is also suggested that the enhancement observed in the  $\lambda \pi^+ \pi^0$  effective mass distribution in the reaction



for those events where the  $\lambda \pi^+$  effective mass was consistent

with the  $Y_1^*$  (1385), was due to the formation of a resonance of Mass 1.88 Gev and width 80 Mev.

#### 1.4 The Experimental Observation of Resonances

In this section some techniques for observing resonance production in bubble chamber experiments will be discussed.

Consider (for example) the reaction



then the effective mass of the  $\lambda\pi^+$  combination is defined by

$$M_{\lambda\pi^+}^2 = (E_\lambda + E_{\pi^+})^2 - (\vec{p}_\lambda + \vec{p}_{\pi^+})^2$$

where  $(E, \vec{p})$  are the total energy and momentum of a particle; in a similar manner all other effective masses can be calculated.

In order to study the variation of the differential cross-section with the effective mass for particular secondary particle combinations, histograms are made for the number of events against the effective mass, and any resonance production is indicated by an enhancement in the differential cross-section for a particular effective mass value.

The probability per unit time that the above reaction will take place is given by

$$W = \frac{2\pi}{\hbar} |M|^2 \rho(E)$$

where  $M$  = matrix element for a transition between the initial and final states

and  $\rho(E)$  is the density of states (phase space) factor.

This expression is invariant under Lorentz transformations and generally  $M$  is completely unknown.

The statistical model <sup>(11,12)</sup> introduced by Fermi assumes that  $M$  is constant so that the transition rate is determined by the phase space factor alone.

The statistical significance of any enhancements in the effective mass distributions is then determined by comparison with the theoretical distributions calculated using this statistical model i.e. they are compared with a Lorentz invariant phase space which is defined <sup>(27)</sup> as

$$\rho_n(E) = \int \prod_{n=1}^n \left[ d^4 q_i \delta(q_i^2 - m_i^2) \right] \delta^4\left(\sum_{n=1}^n q_i - Q\right)$$

where  $n$  = total number of final state particles

$q_i = (E_i, \vec{q}_i)$  = the four vector defining any particle

$Q = (E, \vec{p})$  = the four vector defining the whole final state.

Any significant enhancement can only be interpreted as a resonance after further analysis, or the observation of a similar enhancement in another experiment at a different energy. This effectively removes the possibility of the enhancement being purely a kinematic effect. It is often possible for the production of a resonance in a reaction to influence the other possible effective mass distributions. If, for example, in the above reaction, strong  $Y^*(1385) \rightarrow \lambda + \pi^+$  is observed, then this can

result in an enhancement in the high values of the  $K^+ \pi^+$  system.

The influence of one distribution on another can be well determined by the study of scatter diagrams. For a three body final state with all the final state particles having different masses, a Dalitz plot <sup>(28)</sup> is made by plotting two of the kinetic energies calculated in the overall centre of mass along the x and y axes of a cartesian coordinate system. Total energy and momentum conservation imposes a certain boundary for this plot and it can be shown that equal areas on the Dalitz plot correspond to equal probabilities in Lorentz Invariant Phase Space.

This plot can also be made by plotting any two effective mass combinations along the x and y coordinates which makes comparison between experiments at different energies easier.

It is also possible to apply this method to four-body final states <sup>(29)</sup> where the kinematic limits define an allowed region which is a right angled isosceles triangle but equal areas of the diagram no longer represent equal areas in Lorentz invariant phase space.

### 1.5 The Quantum Numbers of Resonances

In order to classify and understand the behaviour of the resonances found, their quantum numbers have to be determined.

The most important quantum numbers are the Spin (J),

Parity (P), Isospin (I), Charge ( $Q \cong I_3$ ), Hypercharge (Y) and G-parity (G).

Of these, Q and Y can immediately be found by inspection of the reaction in which the resonance is produced. The determination of Q leads to restrictions in the possible values of I, because if  $Q = \pm 1$ , then

$$\text{as } Q = I_3 + Y/2 \quad \text{if } Y = 0 \quad I_3 = \pm 1 \text{ so that } I \geq 1,$$

and similarly for other values of Q and Y.

G-parity can only be defined for particles that have  $S = B = 0$  i.e. the non-strange mesons and mesonic resonances.

G is defined as

$$G = (\text{charge independence}) \times (\text{charge symmetry } (c))$$

$$\text{or } G = (-1)^{l+1}$$

where  $l$  is the orbital angular momentum of the decay products.

For particles with  $Q = S = B = 0$  only C-parity (charge symmetry) is defined and

$$C = (-1)^l$$

These identities for G and C-parity are particularly useful in determining the expected  $K\bar{K}$  decay mode of a resonance. As individual G or C-parities cannot be determined for the K or  $\bar{K}$ , these quantum numbers are determined for the pair; for positive C, the neutral  $K^0\bar{K}^0$  system has to decay through  $K_1^0 K_1^0$  or  $K_2^0 K_2^0$  and for negative C through  $K_1^0 K_2^0$ .

The quantum numbers that have been discussed so far can all be obtained in principle by inspection of the decay of the resonance through the strong interaction or through consideration of the whole final state. The determination of the spin and parity, however, is much more difficult and there are several approaches all of which are well discussed in the literature <sup>(30)</sup>.

As more resonances have been found it has become essential to find some scheme whereby all these particles can be classified. The most recent generally successful scheme has been that of Unitary Symmetry <sup>(31)</sup> which supposes that a super-strong interaction is violated by a medium strong interaction so that singlets, octets and a decuplet of definite spin and parity ( $J^P = 0^-, 1^-, \frac{1}{2}^+, 3/2^+$ ) are formed with the individual members being defined by Y and  $I_3$ .

As it has not been possible to classify all particles using  $SU_3$ , nor have all the predictions been correct, higher symmetries are being sought which may be even more successful in classifying and describing the elementary particles.

## CHAPTER 2

### EXPERIMENTAL PROCEDURE

#### 2.1 Introduction

A flow diagram for the experiment is shown in Figure 2.1.

The 81 cms. Saclay Hydrogen Bubble Chamber was exposed to the 4 Gev/c  $\pi^+$  beam from the C.E.R.N. synchrotron.

70,000 pictures were obtained, which were scanned for all events. After scanning the events were measured and processed using the Program chain developed at C.E.R.N. for Bubble Chamber Film Analysis which will be discussed in Section 2.6.

#### 2.2 The Beam

The experimental arrangement for the 4 Gev/c  $\pi^+$  beam is shown in Figure 2.2.

Circulating protons of 20.14 Gev/c momentum at the rate of one pulse every two seconds struck an internal Beryllium target of dimensions 3 x 4 x 38 mms. which was aligned along the pion beam.

The particles at an angle of  $12\frac{1}{4}^{\circ}$  to the circulating protons within a solid angle of  $5.9 \times 10^{-5}$  steradians were accepted by the first quadropole which formed the entrance of the focussing system.

The beam passed through a series of bending magnets, and magnetic quadropoles before arriving at the momentum slit with a momentum dispersion of 1 Mev/c per centimetre. As the slit was 2 cms. wide the resultant momentum bite was  $\pm 1$  Mev/c.

After passing through more bending magnets and quadrupoles and an electrostatic separator, the beam arrived at the mass slit with angular spreads of 1.3 and 1.4 milliradians in the horizontal and vertical planes, which increased to 3 and 4 milliradians at the bubble chamber entrance.

The mean beam momentum was found from the measurement of many beam tracks to be  $4.0 \pm 0.03$  Gev/c.

The proton and kaon contamination were estimated to be less than 1% but the muon contamination, due to pions decaying in flight was uncertain, but from comparison with the 4 Gev/c  $\pi^-$  experiment was known to be less than 5%.

### 2.3. The Hydrogen Bubble Chamber

The full description of the design and operation of the Saclay 81 cms. Hydrogen Bubble Chamber can be found in an article<sup>(32)</sup> published by the designing group.

The chamber had dimensions 81 x 40 x 31.5 cm<sup>3</sup> and a capacity of 127 litres. It was filled with liquid hydrogen at a pressure of 75 p.s.i.g. and a temperature of 27°k.

The magnetic field used had a value of  $20.7 \pm 0.2\%$  kilogauss at the centre of the chamber, and varied by  $\pm 5\%$  near the edge of the illuminated volume.

The  $\pi^+$  beam entered through a 4 mm. aluminium window and after

a one second delay, three Xenon Flash Tubes were discharged. These gave straight through illumination in an illuminated volume 70 cms. long, 28 cms. wide and 30 cms. deep.

Photographs were taken simultaneously by three cameras  $C_1$ ,  $C_2$  and  $C_3$ , mounted in such a way that their objectives formed an equilateral triangle in a plane about one metre from the front glass.

Photographs were on 35 millimetre unperforated film with a demagnification at the centre of the chamber of about 10:1.

Fiducial marks etched on the inside surfaces of the windows were used as reference points in the chamber. The relative positions of these points were known to an accuracy of 10 microns.

Figure 2.3 shows the coordinate system used in all further discussion.

#### 2.4 Scanning Procedure

Scanning was carried out using the British National tables with a magnification (x10) so that the projected picture had bubble chamber dimensions and two views could be projected side by side.

70,000 pictures were scanned for all events, i.e. 2-prongs, 4-prongs, 6-prongs and strange particle events. A strange particle event was defined as one which had at least one visible particle decay.

For strange particle events 20,000 pictures were studied in Imperial College. All events were recorded irrespective of their

position in the chamber.

The pictures were scanned twice; on the first scan a beam count was carried out on every tenth frame. All pictures on which no beam tracks were seen (due to accelerator failure) and on which the illumination failed in either half of the chamber were recorded for cross-section calculations.

A scan card was completed on the first scan for all interesting events, on which was recorded the event number, event type, any associated electron pairs, stopping protons or secondary scatters. An estimate of the bubble density for each track was recorded and a labelled sketch made for use by the measurer.

The event was classified by a three figure number, e.g. abc

where a = total number of charged secondary tracks

b = total number of observed decaying charged tracks

c = total number of observed neutral V decays.

for example, a 41<sup>+</sup>1 was an event with four charged secondaries, where one of the positive tracks decayed and there was one visible neutral V decay.

In the second scan only the event number and type were recorded so that scanning efficiencies could be calculated.

After both scans, a checkscan was carried out to make sure all events were genuine. Events which had to be rejected were those produced by particles not forming part of the beam, and those where

a recorded  $V^0$  was in fact an electron pair, or had a  $\pi^+ \mu^+ e^+$  decay. The criteria used were as follows:-

Off-Beam:- Any event whose beam track made an angle of 10 milliradians or greater with the  $\pi^+$  beam was rejected.

$\pi^+ \rightarrow \mu^+ e^+$  decay: The decay at rest is characterised by the unique energy of the  $\mu$  and was easily identified on the scanning table using the following guide from (Figure 2.4)

$$p_T = p \sin \theta$$

where  $p_T$  = Transverse momentum perpendicular to AB.

$p$  = Momentum of the decay product

$\theta$  = Angle of emission with respect to the  $V^+$  line of flight

$$\text{now } p = 300H\rho$$

where  $H$  = Magnetic field (kilogauss)

$\rho$  = radius of curvature (metres)

$$P_T = 300H \rho \sin \theta = \frac{300Hl}{2}$$

for  $\pi^+ \mu^+$   $p_T = 20 \text{ Mev/c}$  and for  $K^+ \mu^+$   $p_T = 234 \text{ Mev/c}$  so that if all events where  $l \ll 10 \text{ cms.}$  are rejected, all  $\pi^+ \mu^+$  decays at rest are removed leaving an almost pure sample of  $K^+$  and  $\Sigma^+$  decays.

Electron-pair criterion:- Any  $V^0$  which had zero opening angle could be confused with a fast electron pair.

From Figure 2.5 it can be seen that up to certain momenta of the secondary tracks the decay could be recognised from bubble density estimates. These limits corresponded to a proton momentum of 1.5 Gev/c

and 0.95 Gev/c for protons emitted forwards or backwards in the centre of mass respectively. To try and detect these events where the  $V^0$  simulated an electron pair all electron pairs which had a positive track of a momentum 0.95 Gev/c or greater were selected as  $V^0$ 's.

For  $K^0 \rightarrow \pi^+ \pi^-$  all events could be detected by Ionization up to a momentum of 1.5 Gev/c for one of the pions, so any electron pairs with a track of momentum greater than 1.5 Gev/c were selected as  $V^0$ 's.

## 2.5 Measurement of Events

Measurements were made using three measuring machines. One was built at Imperial College and has been described by Powell (33). The other two were British National measuring machines, built commercially, but with optical systems designed and installed by the Technical Optics group of Imperial College.

The basic design consisted of two horizontal perpendicular stages with the three films to be measured clamped on the x-stage and the projection lenses on the y-stage. These stages were moved by hydraulic rams, whose velocity was determined by the appropriate component of a sine-cosine resolver controlled by the measurer.

The relative motion between the stages was measured using the principle of Moire Fringes with equipment built by Ferranti Ltd. A diffraction grating was fitted to each stage so that there was a small angle between them, and the line spacing of both gratings was

identical and equal to 8 microns. On illuminating the gratings a band pattern was formed at right angles to the bisector of this angle, where the band separation was a function of this angle.

The sinusoidal pattern of light formed by the band pattern was large enough for four photocells to count, using a binary scalar, the passage of the fringes and so the stage displacement.

When the stage moved through one line spacing so the fringe system moved through one band. Four counts were generated per cycle so that one count of the digitiser was equivalent to a distance of 2 microns on the film (20 microns in the chamber).

For measurement the selected view was illuminated by a mercury lamp and a magnified ( $\times 30$ ) image thrown on to a ground glass screen. Interesting points were measured by bringing the central cross on the screen to the point so that its position was recorded with respect to the reference system set up by measuring four back glass fiducials.

All measured points were recorded on 5-hole paper tape as a pair of octal numbers, together with the labels for the tracks and all necessary information required for the book-keeping.

The errors in measurement arise mainly from turbulence in the chamber, multiple coulomb scattering and systematic errors due to the measuring machine. For the present experiment these have been described by Ibbotsen. (34)

## 2.6 Data Processing

All the data were processed using the series of programs developed at C.E.R.N. These were REAP, THRESH, GRIND, BAKE, SLICE and SUMX.

### 2.6.1 REAP <sup>(35)</sup>

REAP is a program written for the Ferranti Mercury computer which re-orders the data on the measurement tapes and punches the data on paper tape in a format suitable for conversion to cards using an IBM 041. The cards are then read on to a magnetic tape which is used as the input to THRESH.

### 2.6.2 THRESH <sup>(35)</sup> Geometrical Reconstruction

As a uniform magnetic field is assumed to be acting at right angles to the front glass all charged particles describe helices. These are reconstructed by THRESH.

A reference system is first constructed; this is defined by the apparent positions  $(x_0, y_0)$  of all the measured fiducials on the inside of the front glass ( $z = 0$  plane).

The apparent positions of the fiducials are computed using the geometrical and optical constants of the chamber. Then from the measured values of the fiducials  $(x_m, y_m)$  the transformation coefficients are calculated using

$$x_0 = \alpha_1 + \alpha_2 x_m + \alpha_3 y_m$$

$$y_0 = \alpha_4 + \alpha_5 x_m + \alpha_6 y_m$$

where the  $\alpha_i$  are determined by least squares for each view. These values are then used to calculate the apparent positions in the  $z = 0$  plane of all measured points.

The line joining a point in the chamber to the nodal point of the camera lens system is now constructed for each view. For a measured point (e.g. the apex) the true point in the chamber is where two of the reconstruction lines from different views intersect. For tracks corresponding points were obtained by interpolation.

For each track in turn and using two views a first approximate helix is fitted through all the coordinates and the apex. If the parameters found were within the specified tolerance, they were improved by least squares fitting to give the final geometrical parameters for the helix (Figure 2.6) described by

$$\begin{aligned}x' &= \rho (\cos \theta - 1) \\y' &= \rho \sin \theta \\z' &= \rho \theta \tan \alpha\end{aligned}$$

From this the parameters sent to GRIND for each track were

$$1/\rho; \lambda; \phi; \text{ and their errors}$$

where

$$1/\rho = \text{curvature}$$

$$\lambda = \alpha = \text{dip angle}$$

$$\phi = \beta = \text{azimuthal angle}$$

### 2.6.3 GRIND <sup>(35)</sup> Kinematical fitting

In GRIND each event is tested by kinematic calculations for

consistency with all hypotheses appropriate to its event type.

From the relation

$$p = 300H\rho$$

p = momentum of the track

H = magnetic field in kilogauss

$\rho$  = curvature of the track.

the energy and momentum of each track is calculated from the curvatures compiled by THRESH. Corrections for energy loss are made by transforming the value of the momentum previously calculated at the centre of the track back to the apex.

At any vertex there are four constraint equations, three for momentum conservation and one for overall energy conservation. If there are fewer than four unknown quantities the equations are overdetermined and the possibility of satisfying all the equations tests the goodness of the fit. The solution is then calculated by the method of least squares which, if the variables are normally distributed, is equivalent to the solution for which the  $\chi^2$ -function had a minimum value.

The  $\chi^2$ -function is defined by

$$\chi^2 = \sum_{j=1}^I \sum_{i=1}^I (m_i - m_i^0)(G_m)_{ij}(m_j - m_j^0) \quad (i)$$

$m_i$  ( $i=1 \rightarrow I$ ) are the fitted variables

$m_i^0$  ( $i=1 \rightarrow I$ ) are the unfitted variables

$m_j, m_j^0$  ( $j = 1 \dots J$ ) are the variables for the unmeasured quantities.  $(G_m^{-1})_{ij}$  is the covariance of the elements  $m_i, m_j$  of the error matrix, of which the inverse  $G_m$  is called the weighting matrix.

If there are  $K$  restraint equations to be satisfied then  $K - J = n$  and  $n$  is defined as the number of degrees of Freedom.

Obviously if, for a particular  $n$ , a limit on the acceptable value for  $\chi^2$  is set, all badly fitted events are rejected.

A more convenient way of doing this is to set a lower limit on the value of the probability for  $\chi^2$ . This is independent of  $n$  so that the same limit can be used for all event types. In particular, for this experiment where the number of events in any channel is small, overall probability of  $\chi^2$  plots can be made, which if the input errors are correct, should be isotropic between 0 and +1.

The probability of  $\chi^2$  is the probability of getting that  $\chi^2(\chi_0^2)$  or greater and is defined by

$$P_n(\chi^2 \geq \chi_0^2) = \int_{\chi_0^2}^{\infty} f_n(\chi^2) d\chi^2$$

where

$$f_n(\chi^2) d\chi^2 = \frac{(\chi^2)^{\frac{n}{2} - 1} e^{-\chi^2/2} d(\chi^2)}{2^{n/2} \Gamma(n/2)}$$

In fitting a strange particle event, GRIND takes three steps. First the apex of the V is considered and fitted, then the primary apex is considered and the event fitted from the geometrical quantities without using the information obtained from the V-fit. This is the

Single vertex fit. After this the final step is an attempt to make an overall fit using all available information, starting from geometrical values and carrying it out in a certain order. This is the Multivertex fit.

For events with a  $V^0$ , fitting is simple and nearly all events give a multivertex fit. For those with charged V's, the fitting is much more difficult. At the  $V^+$ -vertex only one decay product is observed and usually the  $V^+$ -track is very short so that for  $V^+$ -tracks shorter than 6 cms. a zero degree of freedom fit has to be made assuming the momentum of the  $V^+$  is unmeasured.

This leads to many spurious fits being given and generally GRIND can not find a multivertex fit.

GRIND produces a library tape which records for every measurement the geometry, possible hypotheses and the Summary Bank of GRIND.

#### 2.6.4 Post-kinematic programs

(35)  
BAKE

This program has the GRIND library tape as input. BAKE contains subroutines to calculate additional kinematical quantities, effective masses, potential lengths and weights.

BAKE also makes a tentative interpretation of the event from examination of the probabilities of  $\chi^2$  of the successful fits. A punched card is produced which suggests the event is to be studied,

rejected or accepted. These cards, one for each successful measurement of an event are used to guide SLICE.

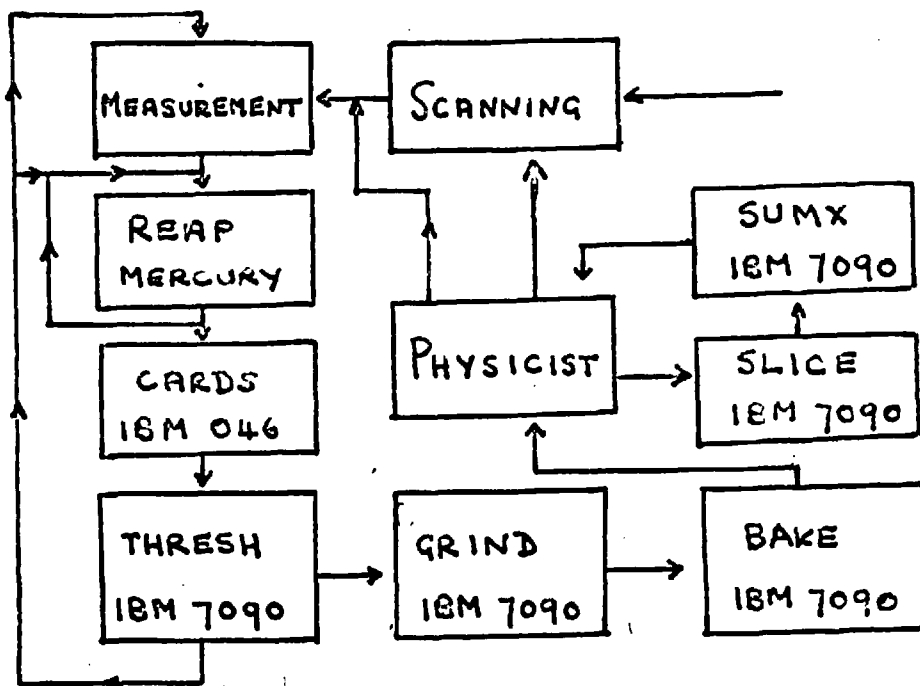
SLICE (35)

SLICE is a program which reads the BAKE library tape and by comparison with the list of required events and hypotheses formed from the SLICE cards, writes a new data summary tape, containing all information about the event, which is used in SUMX.

SUMX (35)

This is the final program in the series and contains subroutines which enables the physicist to use the computer to draw the histograms and two-dimensional plots required.

SUMX is completely guided by the physicist who has to specify the type of graph wanted, the lowest point to be plotted, the interval size, the number of intervals, and the locations of the data on the SLICE library tape.



FLOW DIAGRAM FIG. 2.1

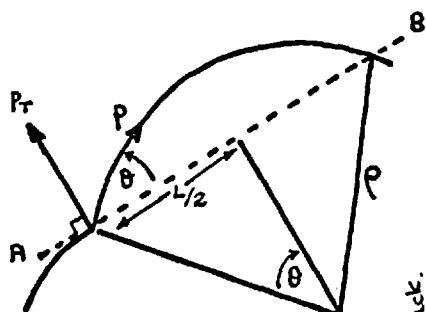


FIG 2.4

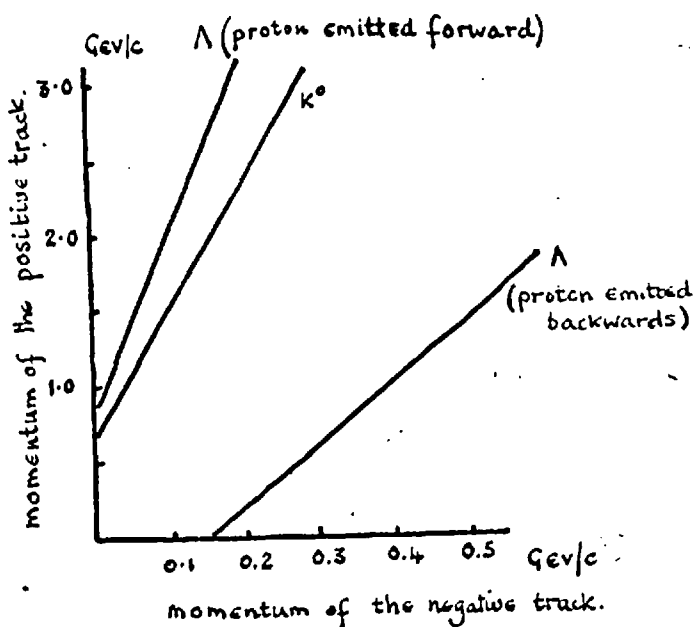
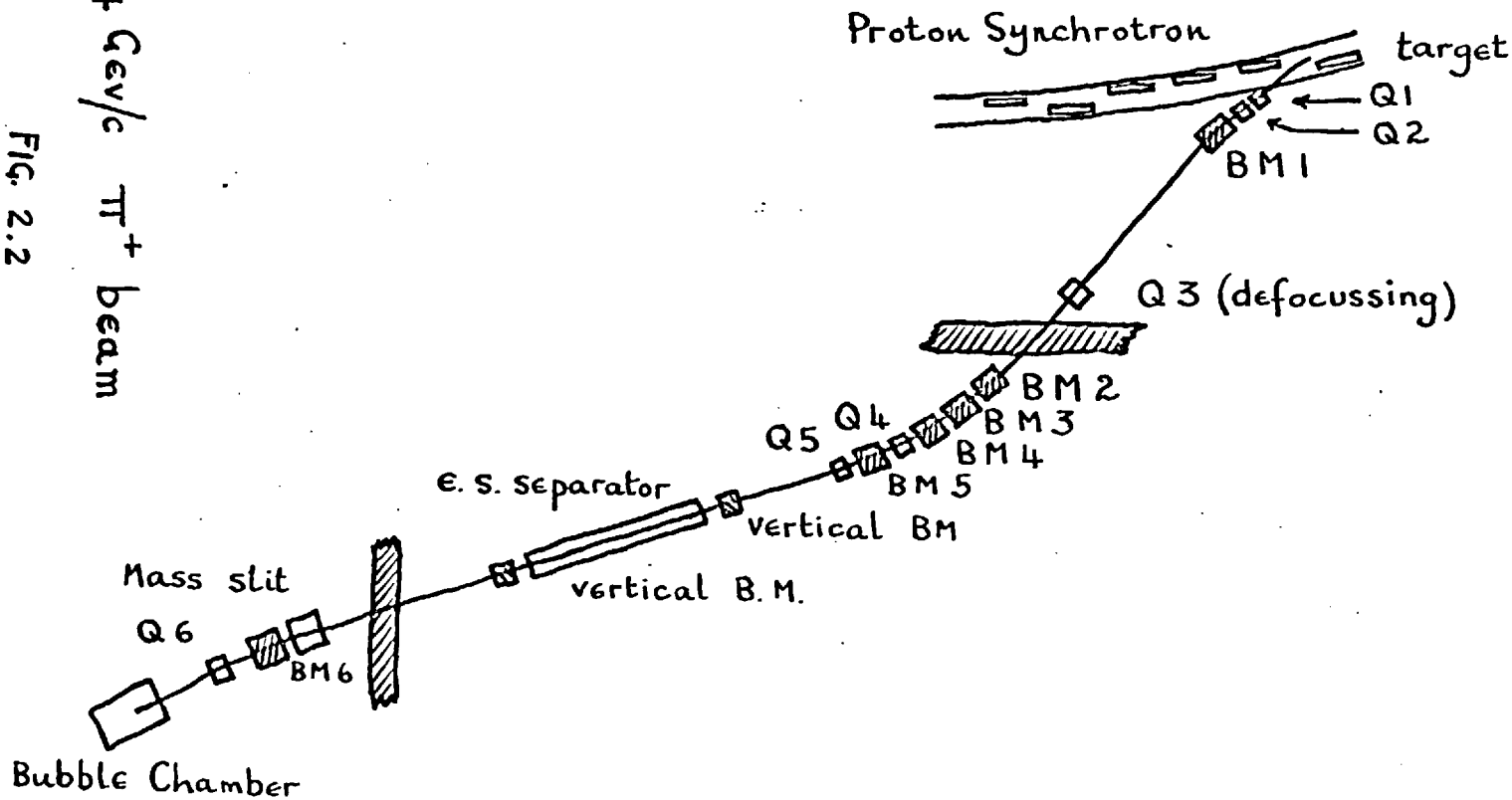


FIG 2.5

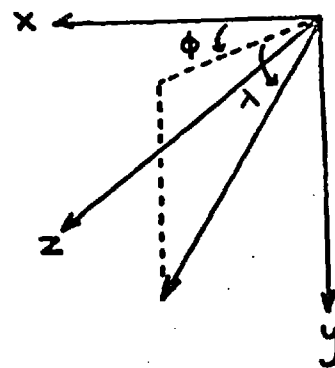
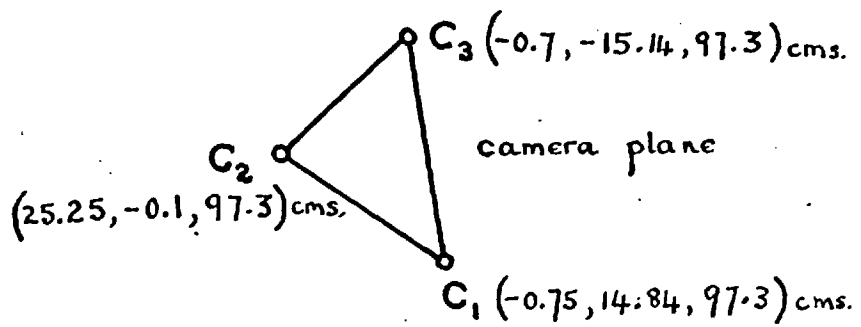
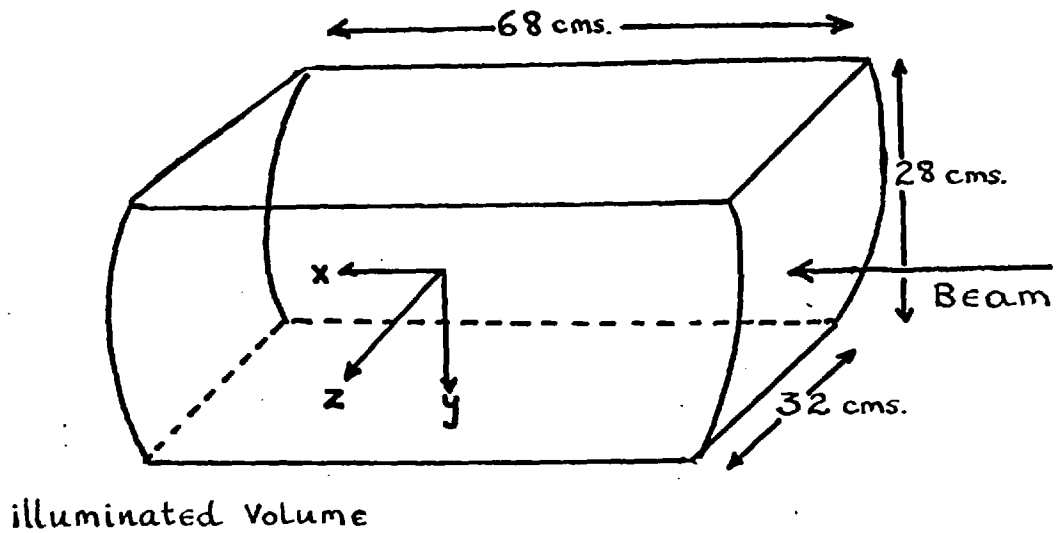
4 GeV/c  $\pi^+$  beam

FIG. 2.2



81 cm. CHAMBER GEOMETRY

FIG. 2.3



X Camera 1

X Camera 2

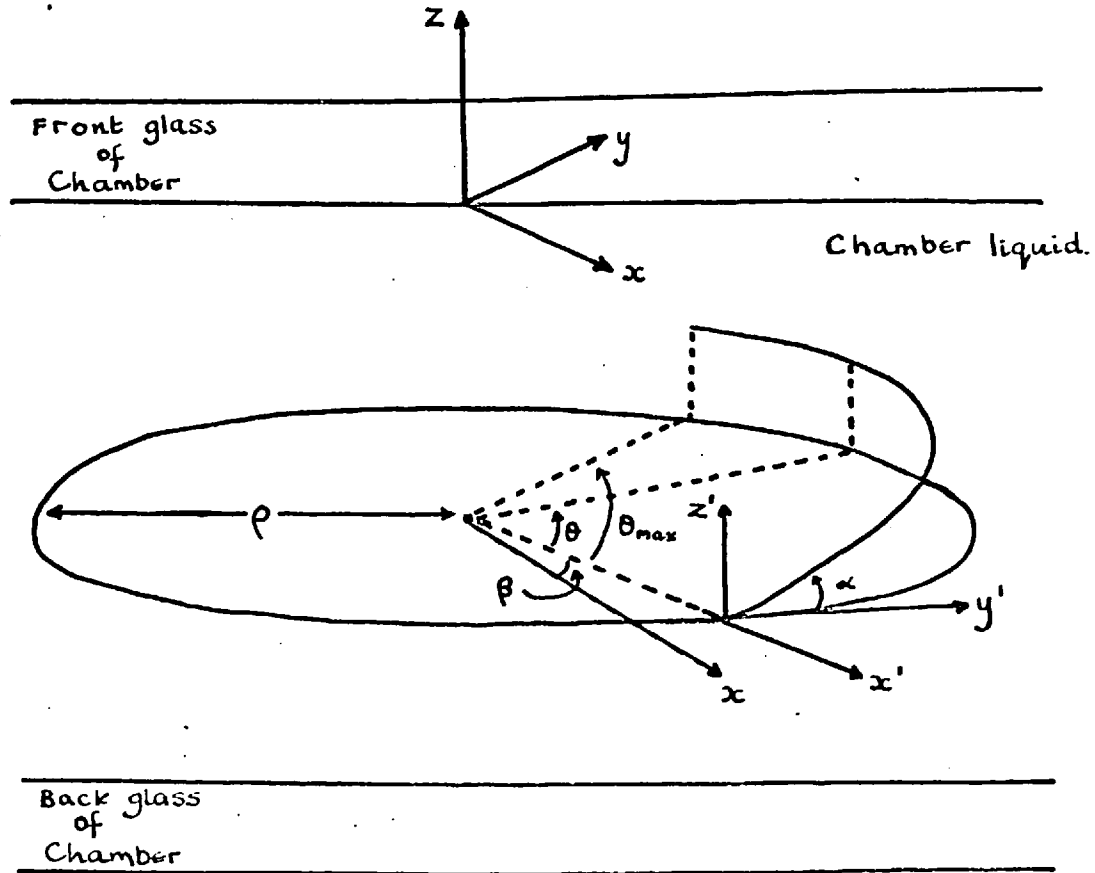


DIAGRAM OF THE RECONSTRUCTED HELIX

FIG. 2.6

### CHAPTER 3

#### INTERPRETATION OF EVENTS WITH ONE OR TWO $V^0$ 'S.

##### 3.1 The Fiducial Volume

The Fiducial Volume was the selected volume of the chamber within which the apex of the event had to occur. No decision was taken on its size until after all the events were measured.

It was obvious that the best possible statistics were required which meant using the largest possible fiducial volume.

All events that had a beam track of length greater than about 1 cm. and no secondary track shorter than 5 cms. were measured.

The limits to the fiducial volume were decided after analysing all the 201 events. No limitations were required in the y and z directions as the beam was extremely well defined (see Figures 3.1 and 3.2).

The limits in the x-direction were set after making a distribution of the x-coordinate of the apex (Figure 3.3) for all events and three plots for the 201 events for the cases:

- (1) events which gave an unique fit
- (2) ambiguous events
- (3) no fit events.

From these plots it was seen that 13% of the ambiguous events had a x-coordinate of greater than 32cms. which coincided with the

point where there was a large fall off of events in the overall plot. From this the lower limit was set at  $x \geq + 32$ cms. The upper limit was determined by the minimum length of beam track needed for an event to be fitted. The  $\pi^+$  beam had extremely well defined momentum and angles (Figure 3.4, 3.5 and 3.6) so that the momentum was set to 4.000 Gev/c in GRIND and no measurement was necessary. For a good angles determination 2 - 2.5 cms. of beam track was required so the upper limit on the x-coordinate was set at  $x \leq - 22$ cms, giving a large fiducial volume 50 cms. in length.

### 3.2 Scanning Efficiencies

From the two scans, scanning efficiencies could be estimated.

20,000 pictures had been studied at Imperial College.

These had been scanned in two sets (a and b) of 10,000 pictures in slightly different ways so a check had to be made to ensure they were consistent.

The efficiencies of the two scans, the total efficiency and true number of events were calculated in the following way:

$$\begin{aligned} \text{let } N_1 &= Ne_1 & N_2 &= Ne_2 & N_{12} &= Ne_{12} = Ne_1e_2 \\ \text{where } N_1 &= \text{number of events found in the first scan} \\ N_2 &= \text{" " " " " " " second scan} \\ N_{12} &= \text{" " " " " " " both scans} \\ N &= \text{true number of events.} \end{aligned}$$

$e_1, e_2, e_{12}$  were the respective efficiencies and  $e$  was the total efficiency.

Then, the probability of missing an event on the first scan =  $(1 - e_1)$

" " " " " " " " second " =  $(1 - e_2)$

so that the probability of finding an event in either scan was given by

$$e = [1 - (1 - e_1)(1 - e_2)]$$
$$e = \frac{N_{12} [N_1 + N_2 - N_{12}]}{N_1 N_2}$$
$$N = \frac{N_1 N_2}{N_{12}}$$

N does not represent the total number of events, because, for example, all those events which had  $V^0$ 's with neutral decay modes, would not have been detected on either scan. Further corrections have to be made before cross-section can be calculated.

The results are given in Table 1, separately for one  $V^0$  events, one  $V^+$  events and two V events.

From Table 1 it can be seen that for events with one  $V^0$  the two sets are identical and so can be treated together, and the same is true for the two V events. For events with one charged V there appears to be a slight discrepancy between the two sets, so the average of the two total efficiencies has been used. As was expected the scanning efficiency for the detection of charged V's is much lower than for  $V^0$  events; this is because during scanning a kink in a track can easily be missed, particularly if the beam is dense.

Table 2 shows the numbers and types of the events for Imperial College and the whole collaboration.

### 3.3 Use of Ionization in Identification of Tracks

From the Ionization Density estimates made at the scanning table, pions, kaons and protons could be distinguished. In a few cases gap counting was necessary.

It is well known that bubble density is proportional to  $1/\beta^2$ <sup>(57)</sup> (where  $\beta = \vec{p}/E$  and  $\vec{p}, E$  are the momentum and energy of the particle.) up to 1 - 2 Gev/c. Curves for all particles for the Hydrogen Bubble Chamber are shown in Figure 3.7.

As the chamber conditions were not known for each photograph, a comparison had to be made between the track in question and a minimum ionizing beam track. These estimates could distinguish between minimum, 1.5x minimum, up to 4x minimum; above this density estimates were impossible.

As Figure 7 shows, a proton and pion can be distinguished up to a momentum of 1.5 Gev/c; a pion and a kaon up to 0.95 Gev/c and a proton and a kaon up to 1.5 Gev/c. Because of the good separation for pions and protons, no  $V^0$ 's were ambiguous between  $\lambda$ 's and  $K^0$ 's. Many of the ambiguous events were due to the positive track in question having a momentum greater than 0.95 Gev/c and so compatible with either a pion or a kaon.

Gap counting was generally not very useful in aiding the identification of strange particle events and it has been discussed fully by F. Campayne. (38)

#### 3.4 Probability of $\chi^2$ distribution for $V^0$ events

A total of 178 events with one or two  $V^0$ 's were measured and analysed at Imperial College.

To check that the analysis and input errors were correct  $P_n(\chi^2)$  distributions are given for the  $V^0$ , single vertex and multivertex fits in Figure 3.8, 3.9, 3.10, 3.11. As the statistics are poor,  $\chi^2$  distributions are not given for the different hypotheses separately but they are consistent with the theoretical normalised curves.

Figures 3.8, 3.9 show the  $P_n(\chi^2)$  distributions for the  $\lambda$  and  $K^0, V^0$  fits respectively. These plots are for all 202, 201, and 401 events. If the analysis and errors are correct then these distributions should be flat between 0 and +1; however, Figure 3.8 shows there is a considerable excess of events between +0.7 and +1.0 for the  $\lambda$  fit. This effect is much more apparent for the  $\lambda$  than the  $K^0$ .

The ratio of  $\lambda$  to  $K^0$  production is roughly 3:2 so that a comparison was made between normalised plots of  $P_n(\chi^2)$  for  $\lambda$  and  $K^0$  (Figure 3.12). These plots are identical between +0.5 and +1.0 but a depletion of  $\lambda$ 's than  $K^0$ 's with  $0 \leq P_n(\chi^2) < 0.5$

is observed. This indicates that the departure from an isotropic distribution is a feature of both the  $K^0$  and  $\lambda$  fits and requires a general explanation.

There are two possible explanations for an excess of highly probable fits.

If the input apex errors are too large then too many very probable fits are obtained which will result in some excess. This could be so here as the apex errors were chosen to be  $\pm 0.017$  cms. in the x and y directions and  $\pm 0.10$  in the z direction, from the distribution of the apex errors for primary vertices; as it is much easier to get a good measurement for the  $V^0$  apex than for a primary vertex or  $V^+$  vertex, a smaller error would have been preferable.

The other explanation which could lead to highly probable events being favoured is that because half the events were measured twice with both measurements giving acceptable fits, a choice had to be made and the measurement which gave the best multivertex fit was taken. Invariably this led to the best  $F_{\text{M}}(\chi^2)$  being taken for the  $V^0$  fit.

These two effects are both present and qualitatively explain the observed features of the plot.

Figures 3.10, 3.11 give the  $P_{\text{M}}(\chi^2)$  distribution for the single vertex and multivertex fits for the uniquely fitted 201's

only. As expected these are in good agreement with an isotropic distribution confirming that the input errors and analysis are correct.

### 3.5 Scanning Biases for $V^0$ events

The criterion used to distinguish  $V^0$ 's from electron pairs was given in Section 2.4.

Figures 3.13, 3.14 show the  $\text{Cos}\theta^*$  distributions for the proton and positive pion in the  $\lambda$  and  $K^0$  rest frames respectively. If there was no systematic loss of events due to the configuration of the  $V^0$ , these distributions should be isotropic. This is essentially true for both the  $\lambda$  and  $K^0$  distribution.

Other biases were due to the loss of events where the  $V^0$  decays within a few millimetres of the apex. The minimum distinguishable distance was set at 2 mms. for the calculation of potential weights and no evidence has been found for loss of events at a length greater than this.

As a further check on the interpretation of the  $V^0$  the lifetime was calculated from

$$N = N_0 \exp\left[-Lm/pc\tau\right] \quad (i)$$

where  $N$  = Number of undecayed  $V^0$ 's

$N_0$  = Total number of  $V^0$ 's

$L$  = Distance travelled before decay

$M$  = Mass of the  $V^0$

$p$  = Momentum of the  $V^0$

$\tau$  = Lifetime of the  $V^0$

$c = 3 \times 10^{10}$  cms/sec<sup>2</sup>

Figures 3.15, 3.16 show the distribution for  $\ln N'$  versus  $(L/p)$ .  $N'$  was the number of events decaying within a certain value of  $L/p$  and is directly related to  $N$ . The great disadvantage of this type of plot is that it is momentum dependent and can give no real insight into the loss of events. The values of the lifetimes obtained were

$$\tau_{\lambda} = 2.34 \pm 30\% \times 10^{-10} \text{ secs.}$$

$$\tau_{K^0} = 0.92 \pm 30\% \times 10^{-10} \text{ secs.}$$

which are in agreement with the known values (39).

Apart from the scanning biases, corrections had to be made for the neutral decay modes of the  $V^0$  and other biases which will be discussed in Chapter 5.

### 3.6 The Analysis of 201 events

The possible channels giving events of the type 201 were

$$\pi^+ p \rightarrow K^+ \pi^+ \lambda / \Sigma^0 \quad (1)$$

$$\pi^+ p \rightarrow K^+ \pi^+ \lambda \pi^0 \quad (2)$$

$$\pi^+ p \rightarrow \pi^+ \pi^+ \lambda K^0 \quad (3)$$

$$\pi^+ p \rightarrow \pi^+ \pi^+ K_1^0 \lambda / \Sigma^0 \quad (4)$$

$$\pi^+ p \rightarrow p \pi^+ K_1^0 K^0 \quad (5)$$

$$\pi^+ p \rightarrow K^+ p K_1^0 \quad (6)$$

$$\pi^+ p \rightarrow K^+ p K_1^0 \pi^0 \quad (7)$$

$$\pi^+ p \rightarrow K^+ \pi^+ K_1^0 n \quad (8)$$

After the  $V^0$  had been identified the bubble density of the two positive tracks and the probability of  $\chi^2$  of the multivertex fit were considered. If the momentum of the track was such that no track could definitely be identified as a  $K^+$  or a proton then the probability of  $\chi^2$  for the possible multivertex fits was examined. Any fit with a  $P_n(\chi^2) \leq 1\%$  was rejected; if several fits had acceptable probabilities of  $\chi^2$ , then those that had a  $P_n(\chi^2)$  less than an eighth of the most probably fit were rejected.

Using this criterion only 2% of the assignments were incorrect; this had been determined from a detailed examination of the analysis of the 2-prong events in the 4 GeV/c  $e \pi^- p$  experiment <sup>(40)</sup> where no comparison of probability  $\chi^2$  had been made in the analysis.

Table 3 shows the total number of 201, 202 and 401 events found in each channel by Imperial College and the whole collaboration.

For each channel the missing mass squared given by

$$(\overline{M}_m)^2 = (\sum_{f_{vis}} E_f - E_{in})^2 - (\sum_{f_{vis}} \vec{p}_f - \vec{p}_{in})^2$$

was plotted as an ideogram (Figure 3.17 and 3.22). These plots should peak at the missing mass squared for the unobserved neutral particle in a particular hypothesis. These values are

0.02 Gev<sup>2</sup> for the  $\pi^0$

0.247 Gev<sup>2</sup> for the  $K^0$

0.88 Gev<sup>2</sup> for the n

1.243 Gev<sup>2</sup> for the  $\lambda$

1.42 Gev<sup>2</sup> for the  $\xi^0$ .

From these ideograms it can be seen that the analysis of the 201 events was correct, as the peaks of the distributions are consistent with the required hypothesis.

These distributions were also used to determine the contamination in these fitted channels due to channels where more than one neutral particle (and so unfittable) was produced. In all cases the contamination was very small

### 3.7 Analysis of 202 and 401 events

The analysis of two prong events with two  $V^0$ 's or four prong events with one  $V^0$  was carried out in exactly the same way as described in the last section.

As there are so few events of these types no probability of  $\chi^2$  distributions are given, but they are flat.

The possible channels for events of the type 202 were

$\pi^+ p \rightarrow \pi^+ \pi^+ K_1^0 \lambda / \Sigma^0$	1
$\pi^+ p \rightarrow \pi^+ \pi^+ K_1^0 \lambda / \Sigma^0 \pi^0$	2
$\pi^+ p \rightarrow p \pi^+ K_1^0 K_1^0$	3
$\pi^+ p \rightarrow p \pi^+ K_1^0 K_1^0 \pi^0$	4
$\pi^+ p \rightarrow \pi^+ \pi^+ K_1^0 K_1^0 n.$	5

Table 3 shows the number of events found in each channel.

As these are so few 202 events, no missing mass squared distributions are given but these were consistent with the chosen hypothesis.

The possible 401 channels were

$\pi^+ p \rightarrow \pi^+ \pi^+ \pi^+ \pi^- \lambda K^0$	1
$\pi^+ p \rightarrow p \pi^+ \pi^+ \pi^- K_1^0 \bar{K}^0$	2
$\pi^+ p \rightarrow \pi^+ \pi^+ \pi^+ K^+ K^0 n$	3
$\pi^+ p \rightarrow p \pi^+ \pi^+ K^+ K^0$	4
$\pi^+ p \rightarrow p \pi^+ \pi^+ K^+ K^0 \pi^0$	5
$\pi^+ p \rightarrow K^+ \pi^+ \pi^+ \pi^- \lambda / \Sigma$	6
$\pi^+ p \rightarrow K^+ \pi^+ \pi^+ \pi^- \lambda / \Sigma \pi^0$	7

and about 50% of the events proceeded by reaction (6).

Again, as statistics are poor, no missing mass squared distributions are given but they are consistent with the chosen hypothesis.

TABLE 1  
SCANNING EFFICIENCIES

EVENT TYPE	$N_1$	$N_2$	$N_{12}$	$e_1\%$	$e_2\%$	$e\%$	N
201(a)	76	75	68	90.7	89.5	99.05	83.8
201(b)	62	62	56	90.4	90.4	99.13	68.6
201	138	137	124	90.49	89.84	99.02	152.5
401	13	13	12	92.33	92.33	99.43	14.08
Total IV <sup>o</sup>	151	150	136	90.69	90.09	99.1	166.5
202	14	14	13	93.3	93.3	99.47	15.08
2V <sup>+</sup> <sub>n</sub> (V <sup>+</sup> V <sup>o</sup> )	18	16	15	93.75	83.3	98.96	19.2
Total 2V	32	30	28	93.32	87.49	99.15	34.29
210(a)	36	29	27	93.02	74.94	98.3	38.7
210(b)	25	24	20	83	80	96.7	30
Total 210	61	53	47	88.68	77.05	97.4	68.79
410(a)	35	34	26	76.47	74.28	93.95	45.77
410(b)	16	13	11	84.66	68.78	95.24	18.9
Total 410	51	47	37	78.74	72.56	94.18	64.77
Total IV <sup>+</sup>	112	100	84	84.02	75.02	96.02	133.3

TABLE 2

	Total Number of Events	% Immeasurable	% Curiosity	% No Fit	% Good Fit
I.C.	317	8	4	13	76
MUNICH	358	8	3	17	73
HAMBURG	120	10	15	20	55
AACHEN	268	5	7	18	70
	<u>1,063</u>	<u>7.8%</u>	<u>7.3%</u>	<u>17%</u>	<u>69.5%</u>

TABLE 3

201	$K^+\pi^+\lambda/\Sigma$	$K^+\pi^+\lambda\pi^0$	$\pi^+\pi^+K^0/\Sigma^0$	$p\pi^+K_1^0K_2^0$	$K^+pK_1^0$	$K^+pK_1^0\pi^0$	$K^+\pi^+K_1^0n$
I.C.	17	30	30	14	6	8	7
MUNICH	20	32	24	7	7	5	9
HAMBURG	4	6	2	2	2	3	2
AACHEN	<u>17</u>	<u>17</u>	<u>9</u>	<u>12</u>	<u>4</u>	<u>3</u>	<u>3</u>
Total	58	85	65	35	19	19	21

202	$\pi^+\pi^+\lambda K_1^0$	$\pi^+\pi^+\lambda K_1^0\pi^0$	$p\pi^+K_1^0K_1^0$	$p\pi^+K_1^0K_1^0\pi^0$	$\pi^+\pi^+K_1^0K_1^0n$	401	$K^+\pi^+\pi^+\pi^-\lambda$
I.C.	5	1	3	1	0	I.C.	5
MUNICH	3	1	3	1	2	Mu.	2
HAMBURG	2	?~0	0	~0	~0	Ha.	1
AACHEN	<u>3</u>	<u>?~0</u>	<u>4</u>	<u>~0</u>	<u>~0</u>	Aa.	<u>5</u>
Total	13	2	10	2	2		13

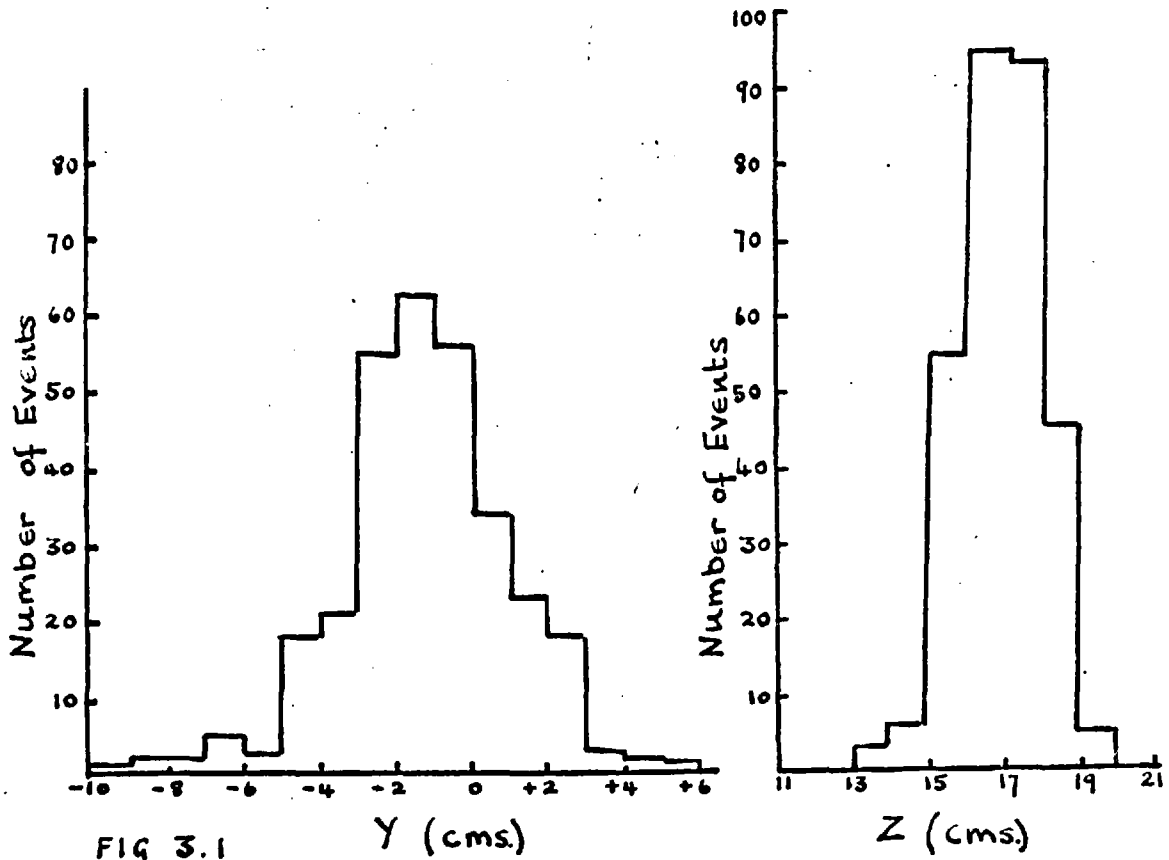


FIG 3.1

Y (cms)

Z (cms)

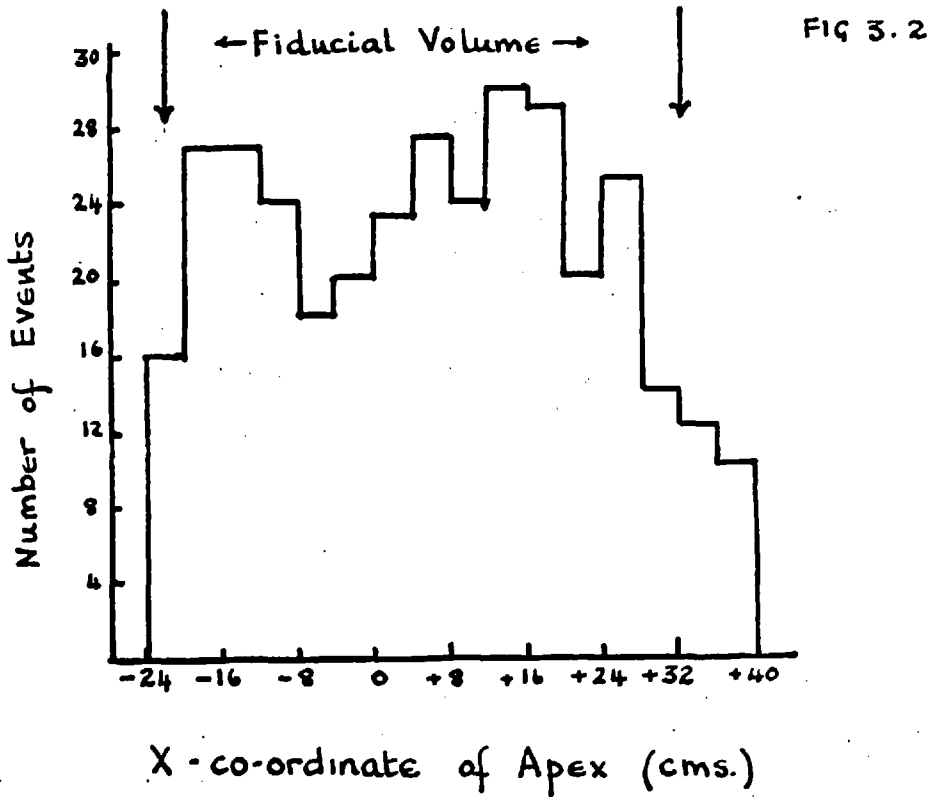
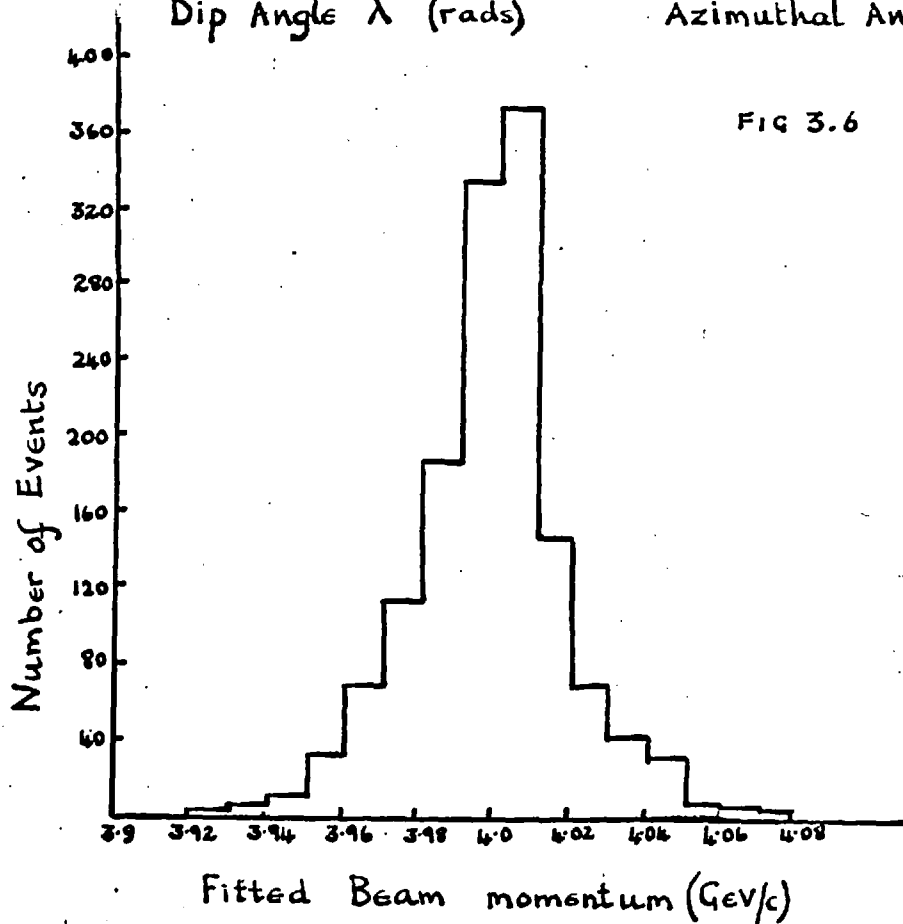
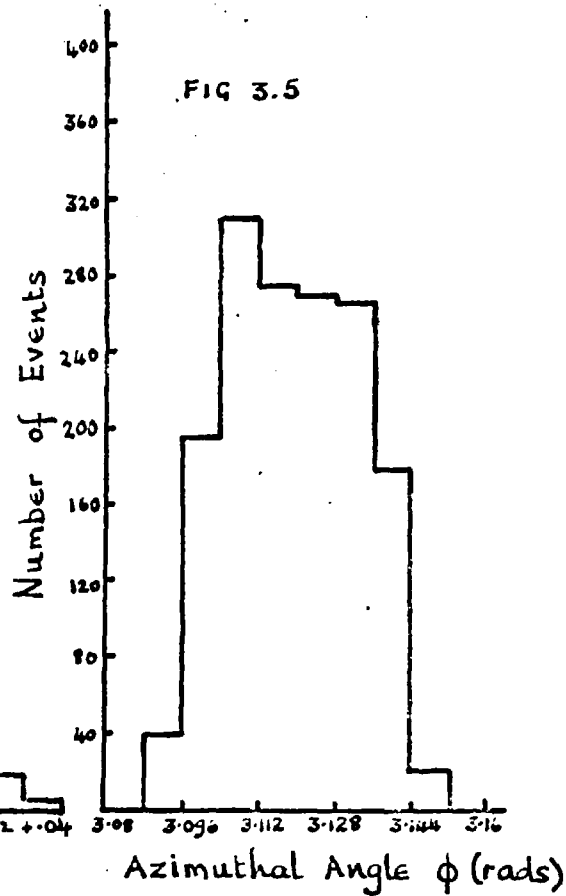
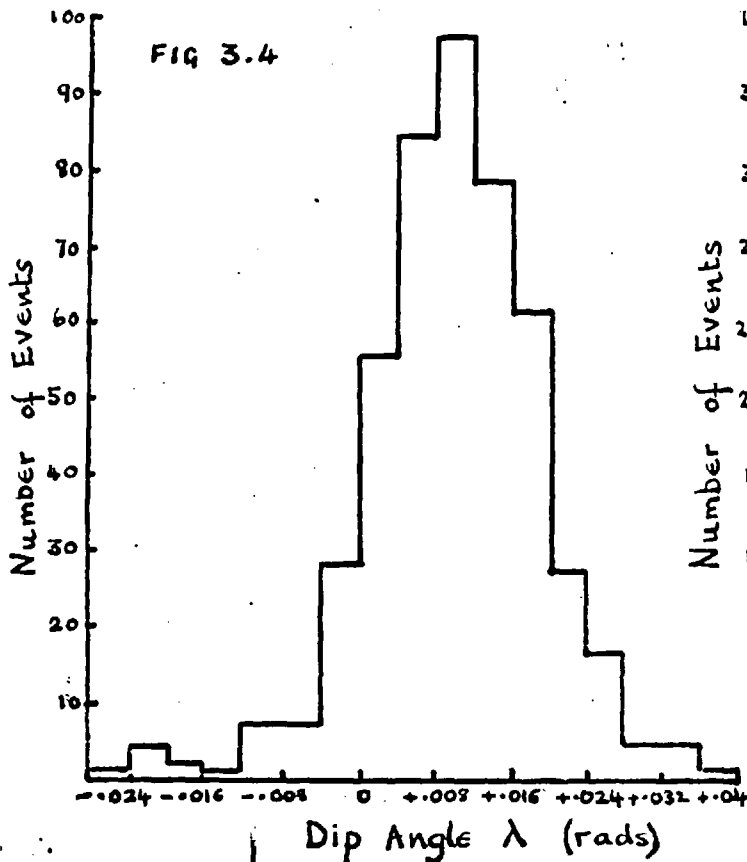
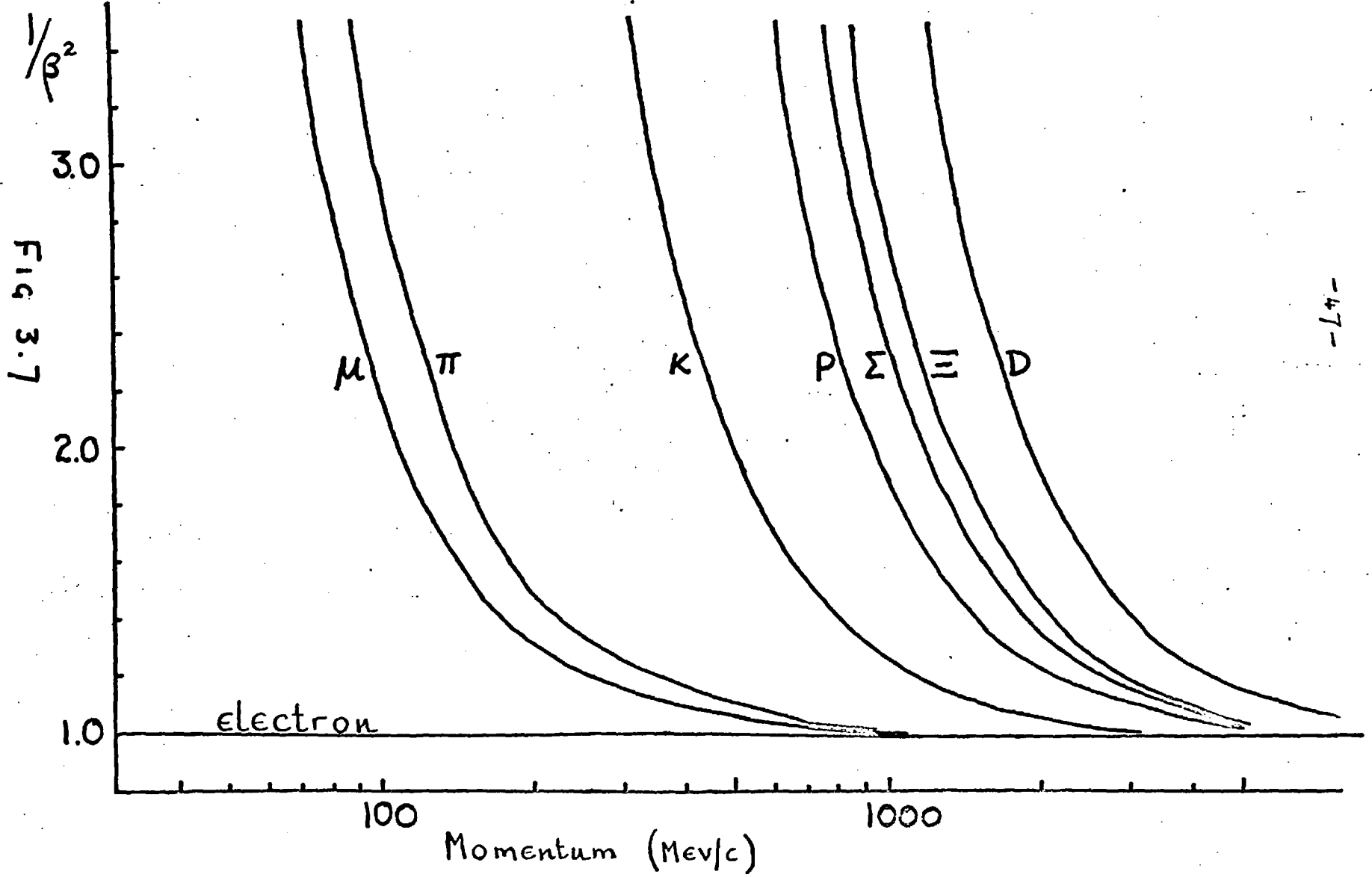


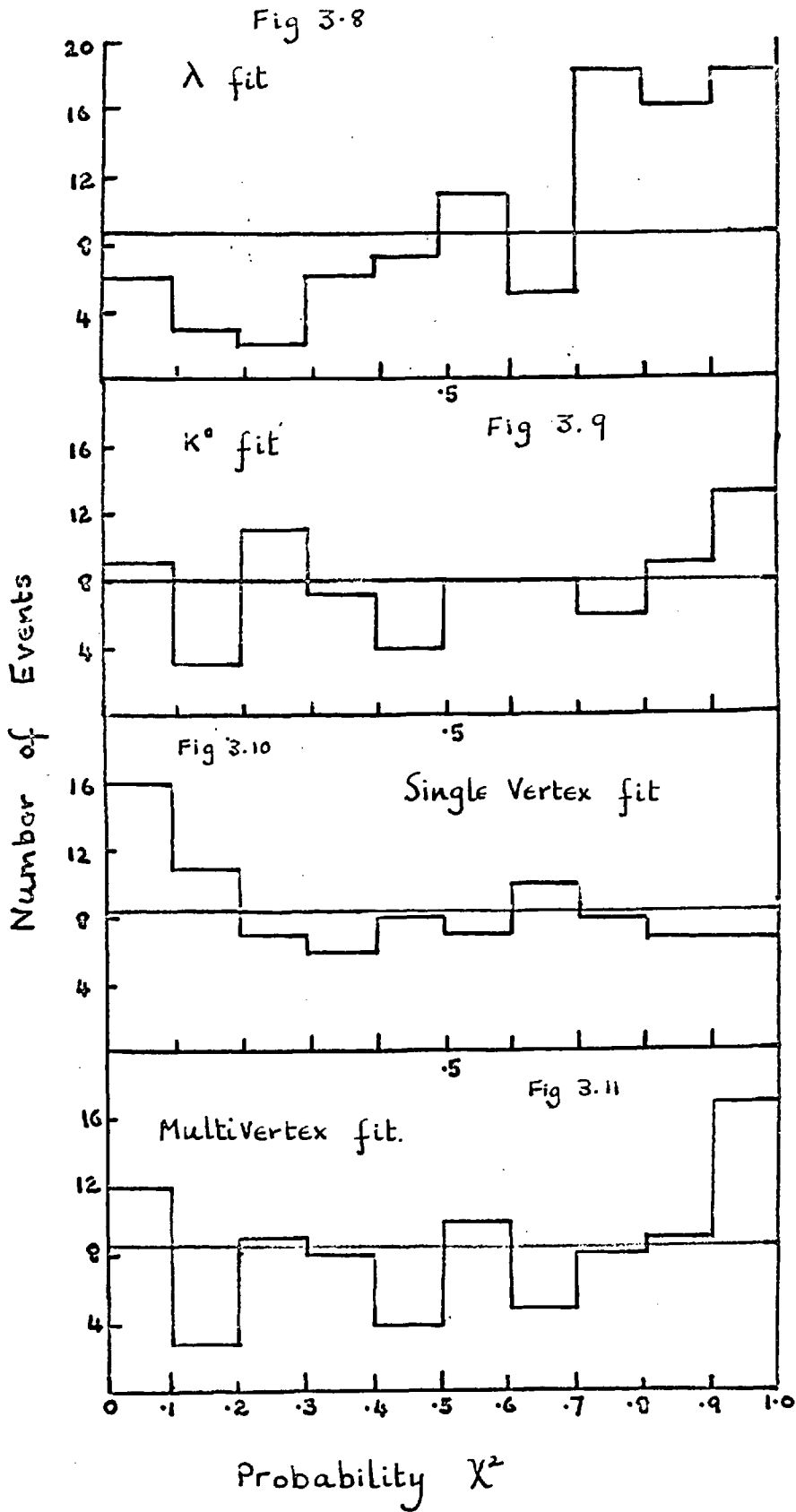
FIG 3.2

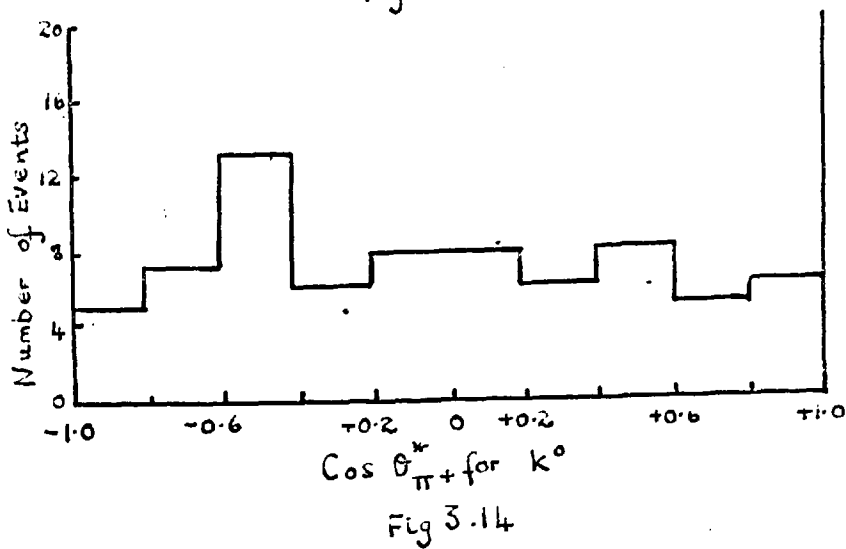
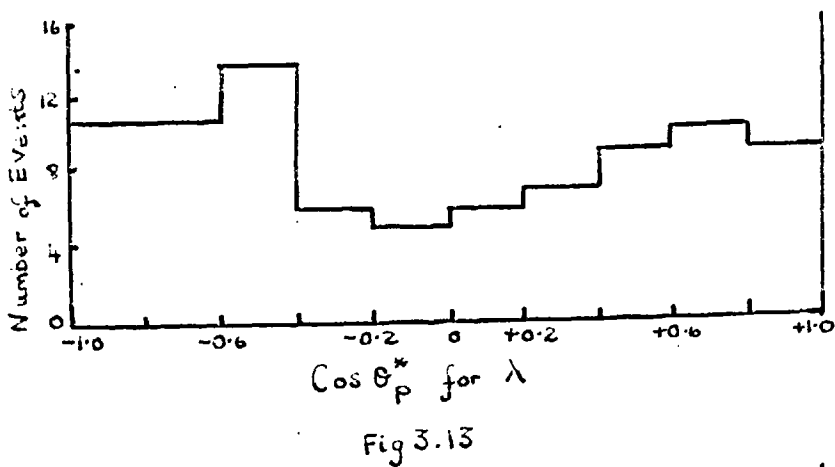
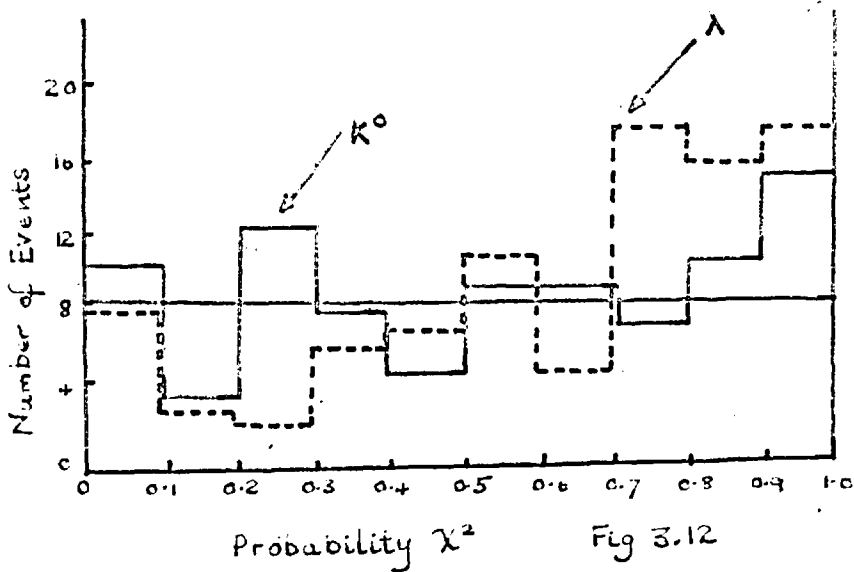
X - co-ordinate of Apex (cms.)

FIG 3.3









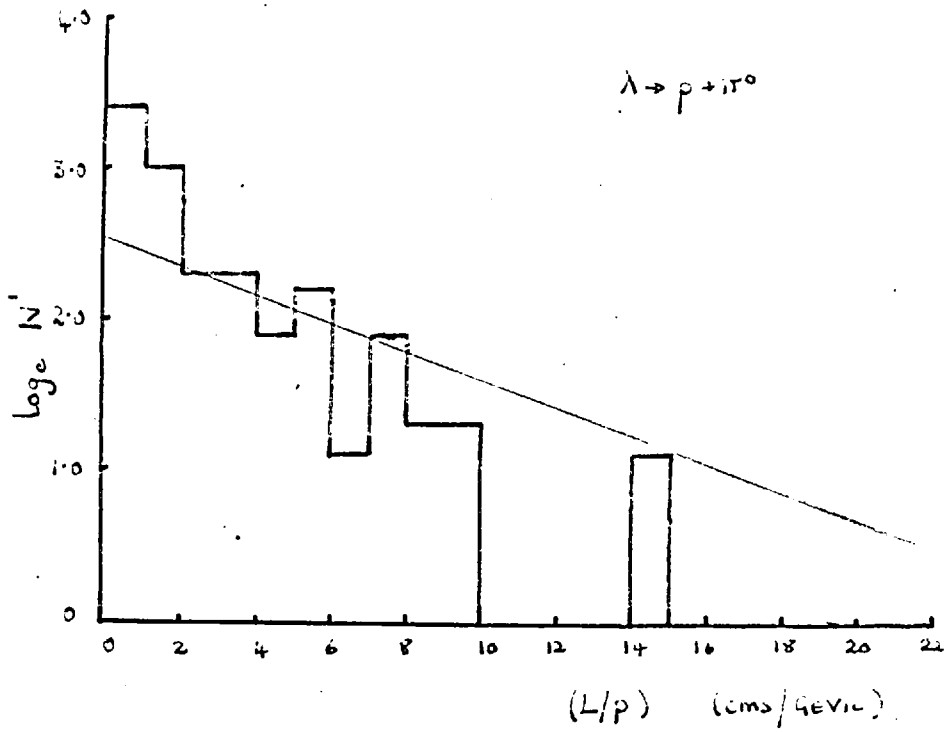


Fig 3-15

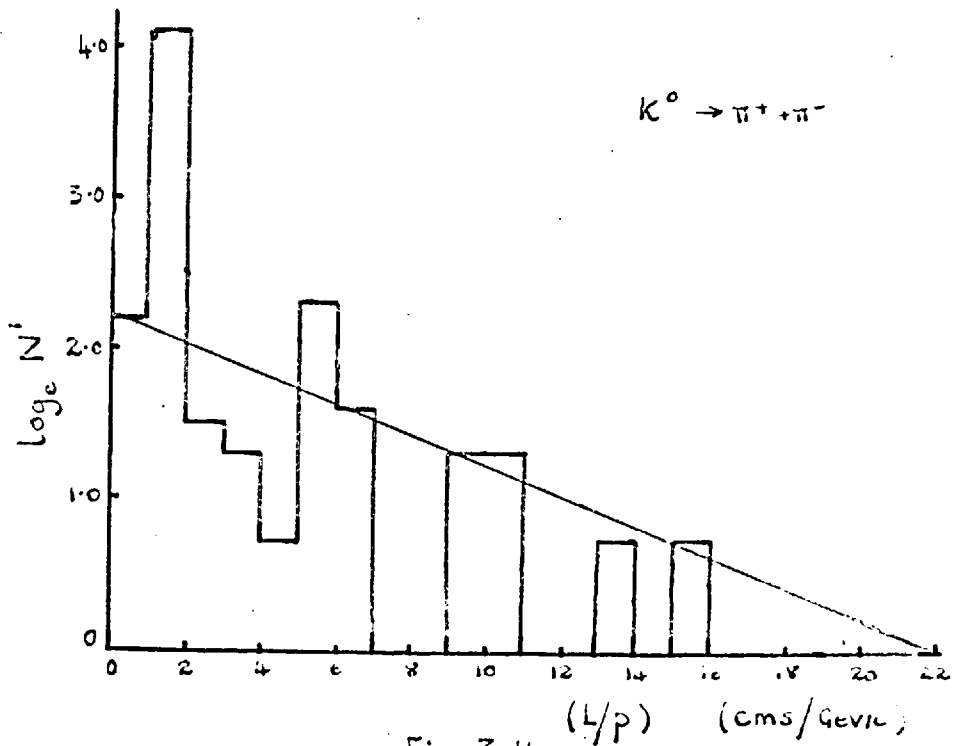


Fig 3-16

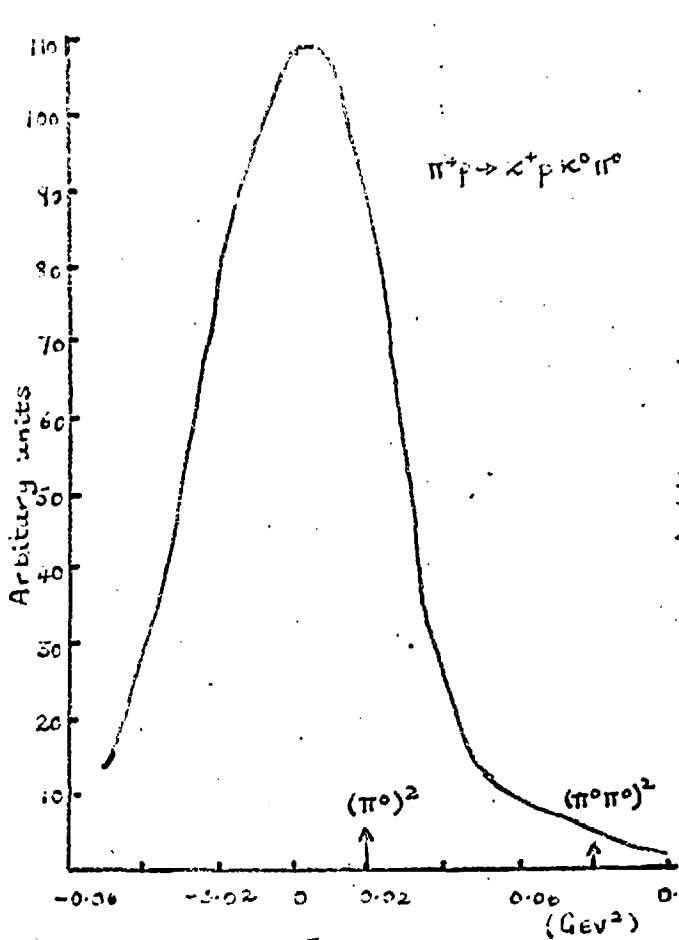


Fig 3.17

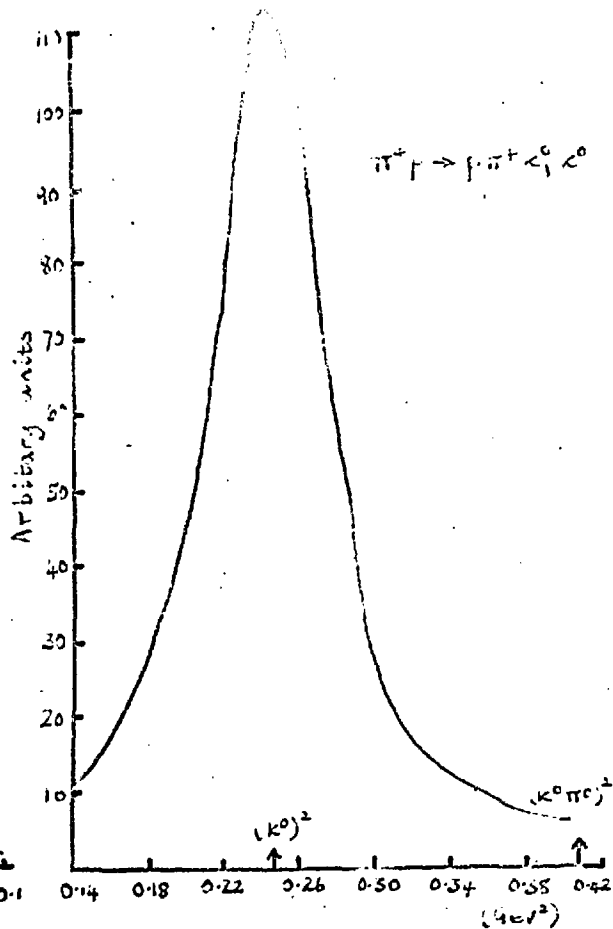


Fig 3.19

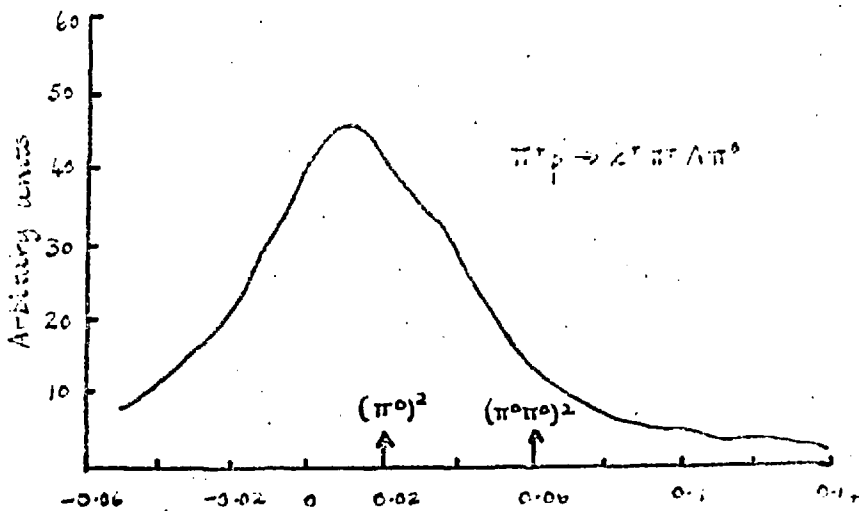


Fig 3.18

(MISSING MASS)<sup>2</sup> (GeV<sup>2</sup>)

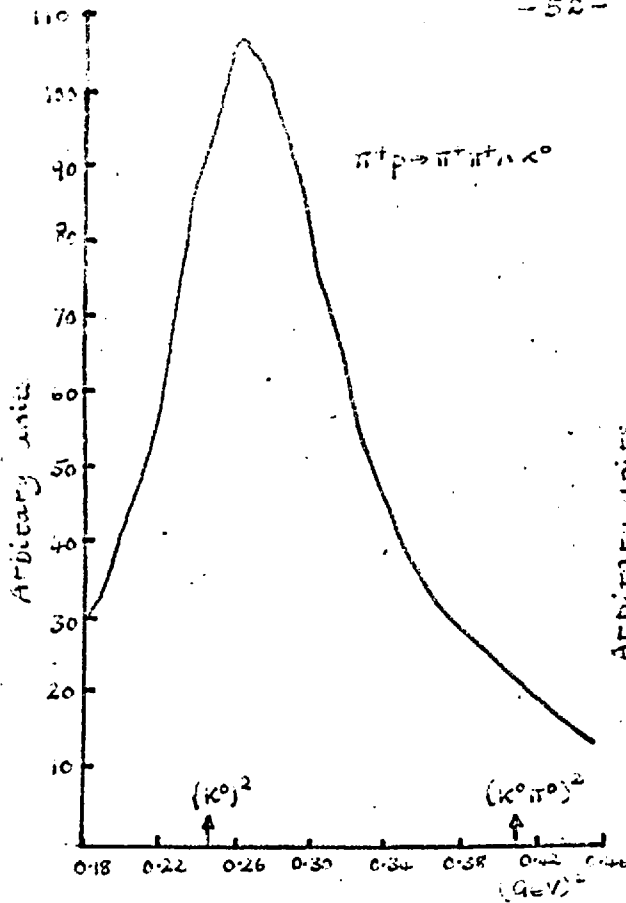


Fig 3.20

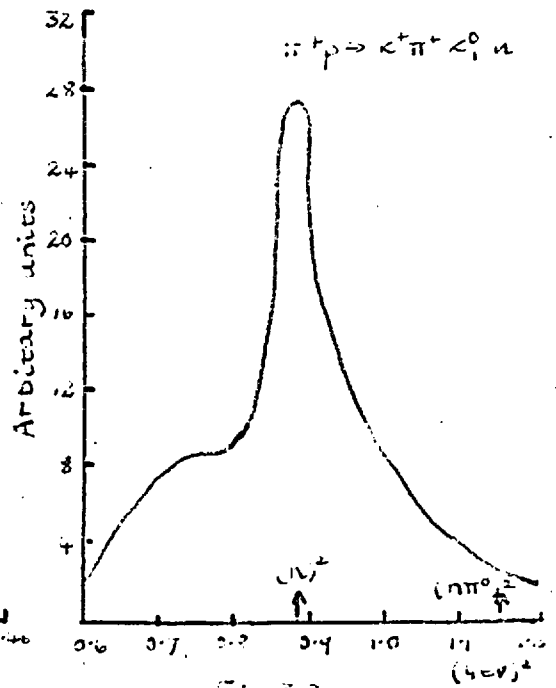


Fig 3.21

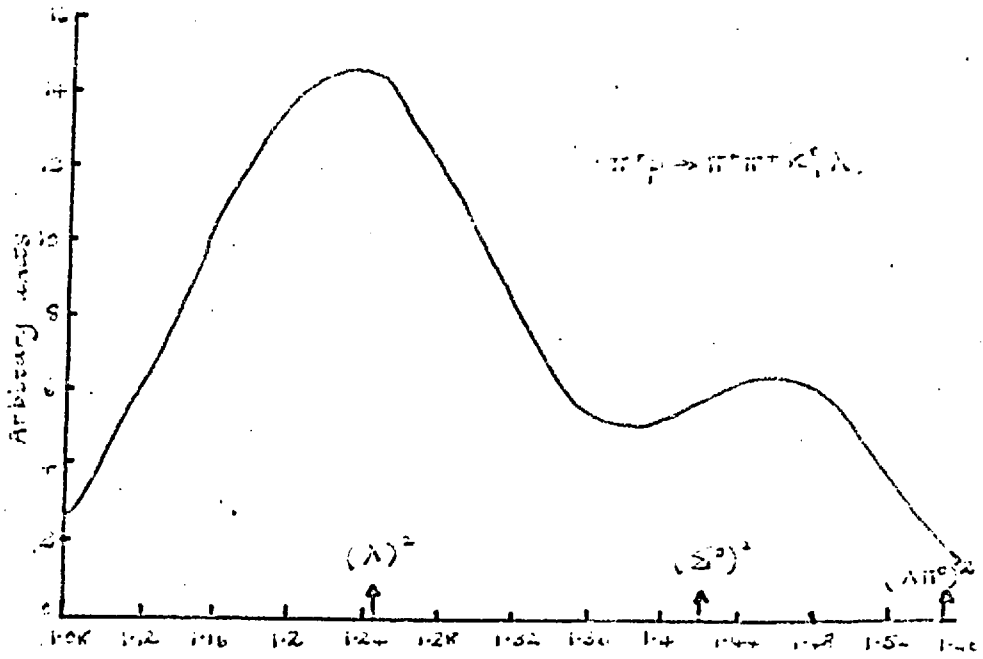


Fig 3.22

(MISSING MASS)^2 (GeV)^2

## CHAPTER 4

### INTERPRETATION OF EVENTS WITH ONE OR TWO CHARGED V'S

#### 4.1 Introduction

139 events with one or more charged V's were measured and analysed at Imperial College. Table 2 of Chapter 3 gives the relevant statistics.

These events were much harder to measure and analyse than events with neutral V's; to try and simplify the analysis, each reasonable measurement of an event with a short  $V^+$  track (up to 6 cms.) was computed twice through GRIND. Once, the measured momentum of the  $V^+$  track was assumed correct and so a one degree of freedom fit could be obtained for the V. This was not necessarily correct, so for the second computation, this momentum was assumed to be unmeasured and a zero degree of freedom fit for the V resulted, which led to many spurious single vertex fits for the event.

In all cases, if the one degree of freedom fit was compatible with the zero degree of freedom fit then it was used for all analysis.

#### 4.2 Probability of $\chi^2$ distributions

Only overall distributions for all charged V events are shown as the number of the individual types are small.

Figures 4.1, 4.2, and 4.3 show the probability of  $\chi^2$  distributions for the V fit, the single vertex and the multivertex fits respectively.

In Figure 4.1 the large number of events for which  $C \leq P_n(\chi^2) \leq 0.1$  are all those for which a zero degree of freedom fit had to be selected; apart from this, the distribution is isotropic.

If this distribution is compared to those for the neutral V fits (Figures 3.8 and 3.9) it can be seen that there is no preponderance of highly probable events. This indicates that the explanations given in Section 3.4 are correct as neither of the two effects are present in the charged V events.

The distributions for the single and multivertex fits are both flat indicating that the interpretation of the events was correct.

The poor statistics can be explained generally by the fact that only those events which gave a unique fit have been used in these distributions. As nearly 50% of the events of the type 210 were ambiguous after analysis, and it was extremely rare to get a multivertex fit calculated in GRIND for these events, only a small percentage of the  $V^+$  events appear in these distributions.

#### 4.5 Scanning Losses for $V^+$ events

The scanning losses were estimated using the techniques

discussed in Section 3.5.

Figures 4.4, 4.5, and 4.6 show the  $\text{Cos } \theta^*$  distributions for the decay of the  $V^+$ .

The decay angular distribution for the proton in the  $\Sigma^+$  rest frame is shown in Figure 4.4. If there was no loss of events due to the production angle of the proton, this distribution should be isotropic. There is a loss of events for  $+0.45 \leq \text{Cos } \theta_p^* \leq +1.0$ , but it is hard to believe that there is a systematic scanning bias up to such a large angle. A more realistic estimate obtained from examination of Figures 4.7 - 4.10 (this will be discussed later) suggests a loss of events up to a production angle of  $5^\circ - 10^\circ$  in the laboratory.

The decay angular distributions for the decays  $\Sigma^+ \rightarrow \pi^+ + n$ ,  $K^+ \rightarrow \mu^+ + \nu$  and  $K^+ \rightarrow \pi^+ + \pi^0$  are given in Figures 4.5 and 4.6, (only one distribution is given for the K decays). These distributions are essentially isotropic indicating that there is little scanning bias for these decays. In Figure 4.6 it is difficult to explain the peak for  $-0.8 \leq \text{Cos } \theta^* \leq -0.4$ , but it is probably due to poor statistics and to the inaccurate calculation of this angle in BAKE, as frequently this value was calculated from the quantities found in a zero degree of freedom V fit which was not necessarily accurate.

From these decay angular distributions the scanning bias due to the decay configuration of the charged V can be estimated. This

estimate, however, is momentum dependant and takes no account of any other factors which could contribute to the overall bias. One method which attempted to determine the overall bias with momentum independence was by the analysis of the distribution of the angle X defined as follows:

$$\cos X = \frac{(\vec{P}_V \times \vec{Z}) \cdot (\vec{P}_V \times \vec{P}_N)}{|\vec{P}_V \times \vec{Z}| |\vec{P}_V \times \vec{P}_N|}$$

where  $\vec{P}_V$  = laboratory momentum of the  $V^+$   
 $\vec{P}_N$  = laboratory momentum of the observed decay product  
 $\vec{Z}$  = Z- direction of the coordinate system.

The first term in this expression defined a vector lying in the x - y plane, while the second defines the normal to the decay plane; therefore the angle between these two vectors shows any bias due to dip, orientation or small angle decays.

If there were no scanning biases X should be isotropic for all values of  $\theta$  (the laboratory production angle of the seen decay product). Figures 4.7 - 4.10 show distributions of X for the following ranges of  $\theta$ :

$0^\circ \leq \theta \leq 6^\circ$	Figure 4.7
$6^\circ \leq \theta \leq 10^\circ$	Figure 4.8
$10^\circ \leq \theta \leq 20^\circ$	Figure 4.9
$20^\circ \leq \theta \leq 180^\circ$	Figure 4.10

Although the statistics are poor it can be seen that for

$\theta \geq 6^\circ$ , the distributions are nearly isotropic indicating negligible biases. For  $\theta < 6^\circ$  (Figure 4.7) the data shows a significant bias for these production angles. This bias is mainly due to the  $\Sigma^+ \rightarrow p + \pi^0$  decay mode which was seen in Figure 4.4. to be biased.

It was realised from this examination that corrections had to be made for only one decay mode,  $\Sigma^+ \rightarrow p + \pi^0$ , for  $\theta \leq 6^\circ$ .

#### 4.4 Lifetime plots for charged V's

The lifetime plots were calculated by the method given in Section 3.5 only for the decay modes with enough events to give significant distributions. These were  $\Sigma^+ \rightarrow p + \pi^0$  and  $\Sigma^+ \rightarrow n + \pi^+$ . Figures 4.11 and 4.12 show the distributions for  $\ln N'$  against  $(L/p)$  which led to the following values for the lifetimes.

$$\tau(\Sigma^+ \rightarrow p + \pi^0) = (0.96 \pm 20\%) \times 10^{-10} \text{ secs}$$

$$\tau(\Sigma^+ \rightarrow n + \pi^+) = (1.30 \pm 20\%) \times 10^{-10} \text{ secs}$$

which are consistent with the known values. ( ))

#### 4.5 The Analysis of the event types 210, 220 and 211.

The possible channels for these events were

$$\pi^+ p \rightarrow K^+ \pi^+ \lambda / \Sigma^0 \quad (210, 211) \text{ event types} \quad (1)$$

$$\pi^+ p \rightarrow K^+ p \bar{K}^0 \quad (210, 211) \text{ event types} \quad (2)$$

$$\pi^+ p \rightarrow \Sigma^+ \pi^+ K^0 \quad (210, 210) \text{ event types} \quad (3)$$

$$\pi^+ p \rightarrow \Sigma^+ K^+ \quad (220, 210) \text{ event types} \quad (4)$$

$$\pi^+ p \rightarrow \Sigma^+ K^+ \pi^0 \quad (220, 210) \text{ event types} \quad (5)$$

Some other channels were possible for 211 events, these were the following:



Obviously, because of the poor statistics, very few events of these channels were found and they have not been used in any distributions.

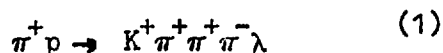
The analysis of these events was carried out in a similar manner to the events with neutral V's, but as stated before the analysis was more difficult. This resulted in a very high percentage of the events remaining ambiguous after analysis of the bubble densities and the probability of  $\chi^2$ . Table 4.1 shows the number of events in each channel.

Figures 4.13, 4.14 and 4.15 show the ideograms for the missing mass squared for the channels, (2), (3) and (5). These are only for the 210 events and because of the difficulty of measuring the short  $V^+$  track which resulted in large errors on the missing mass squared, they are not very good. Figures 4.13 and 4.14 showing the distributions for the  $\Sigma^+$  channels indicate that there must be some contamination due to events with more than one neutral particle being fitted as these hypotheses. The distribution for reaction (2) is shown in figure 4.15 which, although broad, is consistent with that hypothesis.

Contamination in these channels due to the production of more than one neutral particle will be discussed in Chapter 5.

#### 4.6 The Analysis of $41^+_0$ , $41^+_1$ , $42^{++}_0$ events

There are so many possible reactions for these events that only those with  $\Sigma^+$  production will be considered here, with the exception of the channel



which was also seen as a 401 event type.

The interpretation of these events was much simpler than for the 2 prongs with a charged V. Generally, the outgoing tracks were of comparatively low momentum so that examination of the bubble density usually removed ambiguities.

The possible  $\Sigma^+$  channels are as follows:

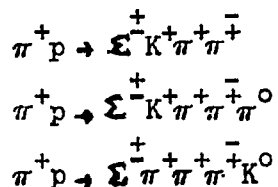


Table 4.2 gives the number of events in each channel.

The missing mass squared ideograms for these channels are shown in Figures 4.16, 4.17 and 4.18, and indicate that these channels have little contamination from events which really have more than one neutral particle produced.

#### 4.7 Ambiguous Events

Ambiguous events arose mainly for one of the two following reasons.

At this primary momentum it is impossible to separate physically the  $\lambda$ 's from the  $\Sigma^0$ 's, so that about 80% of the events which fitted the hypotheses

$$\pi^+ p \rightarrow K^+ \pi^+ \lambda$$

$$\pi^+ p \rightarrow K^+ \pi^+ \Sigma^0$$

were ambiguous.

For want of a better method the events were allocated according to the fit with the highest probability of  $\chi^2$ .

The other ambiguity that could arise due to confusion between  $\lambda$  and  $\Sigma^0$  production, is between the channels

$$\pi^+ p \rightarrow K^+ \pi^+ \lambda \pi^0$$

$$\pi^+ p \rightarrow K^+ \pi^+ \Sigma^0$$

where a very slow  $\pi^0$  is produced. Figure 3.18 shows the missing mass squared ideogram for the first of these channels; this peaks at the  $\pi^0$  mass squared and the only tail in the distribution is at the upper end which is due to the inclusion of events which really have more than one  $\pi^0$  produced. This, therefore, indicates that there is no ambiguity between these two channels.

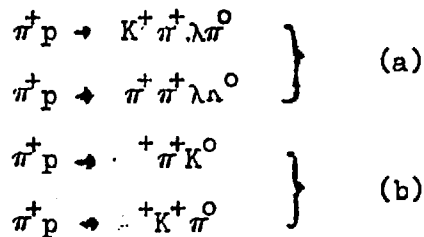
The  $\lambda/\Sigma^0$  ambiguity also affects the following channels

$$\pi^+ p \rightarrow \pi^+ \pi^+ K^0 \lambda / \Sigma^0$$

$$\pi^+ p \rightarrow K^+ \pi^+ \pi^+ \pi^- \lambda / \Sigma^0$$

where the same arguments have been used and the same conclusions reached.

The other major ambiguity was due to some track of momentum greater than 0.9 GeV/c which was ambiguous between a  $K^+$  and a  $\pi^+$ . This mainly affected the 2-prong events where the ambiguities were mainly between the following channels



The ambiguities of type (a) were resolved by allocating the events to the hypothesis with the highest probability of  $\chi^2$ . This was thought to be reasonable as these ambiguous events were only a small fraction of the total number in each channel.

The ambiguities of type (b) were more difficult to resolve. As these were of the type 210, the errors of measurement were very large giving an unrealistic missing mass squared, which could not be used in the analysis of the event. This, therefore, increased the number of ambiguous events. Although the proportion of ambiguous to unique events was large, these events were also allocated to the hypothesis with the higher probability of  $\chi^2$  as no better method could be found. If these events were not included, the distributions for these channels would be meaningless because of the poor statistics.

Therefore, throughout the rest of this thesis, all results are presented with these ambiguous events included, but these events are not used in the distributions given in Chapters 3 and 4.

TABLE 4.1

210	$\Sigma^+ K^+$	$\Sigma^+ K^+ \pi^0$	$\Sigma^+ \pi^+ K^0$	$K \pi \wedge / \Sigma$	$K^+ p K^0$
I.C.	9	8	14	5	4
Munich	20	22	11	6	2
Hamburg	4	8	1	4	4
Aachen	15	13	14	10	4
Total	<u>48</u>	<u>51</u>	<u>40</u>	<u>25</u>	<u>14</u>

220	$\Sigma^+ K^+$	$\Sigma^+ K^+ \pi^0$	211	$\Sigma^+ \pi^+ K_1^0$	$\Sigma^+ \pi^+ K_1^0 \pi^0$	$K^+ \pi^+ \wedge / \Sigma$
I.C.	0	0		3	1	0
Munich	2	3		4	6	2
Hamburg	0	0		1	0	1
Aachen	0	0		0	?	0
Total	<u>2</u>	<u>3</u>		<u>8</u>	<u>7</u>	<u>3</u>

TABLE 4.2

410	$\Sigma^+ K^+ \pi^+ \pi^-$	$\Sigma^+ K^+ \pi^+ \pi^- \pi^0$	$\Sigma^+ \pi^+ \pi^+ \pi^- K^0$	$K^+ \pi^+ \pi^+ \Sigma^-$	$K^+ \pi^+ \pi^+ \Sigma^- \pi^0$	$\pi^+ \pi^+ \pi^+ \Sigma^- K^0$
I.C.	10	9	4	2	1	3
Munich	19	12	2	2	3	2
Hamburg	4	1	1	0	1	0
Aachen	11	5	2	1	1	0
Total	<u>44</u>	<u>27</u>	<u>9</u>	<u>5</u>	<u>6</u>	<u>5</u>

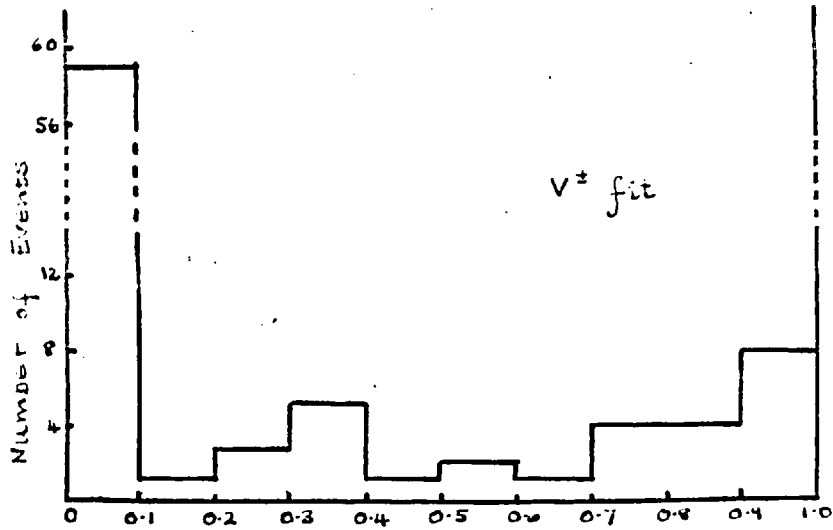


Fig 4.1

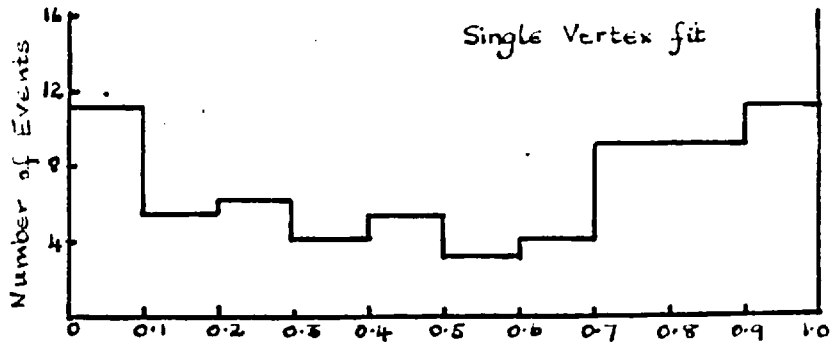


Fig 4.2

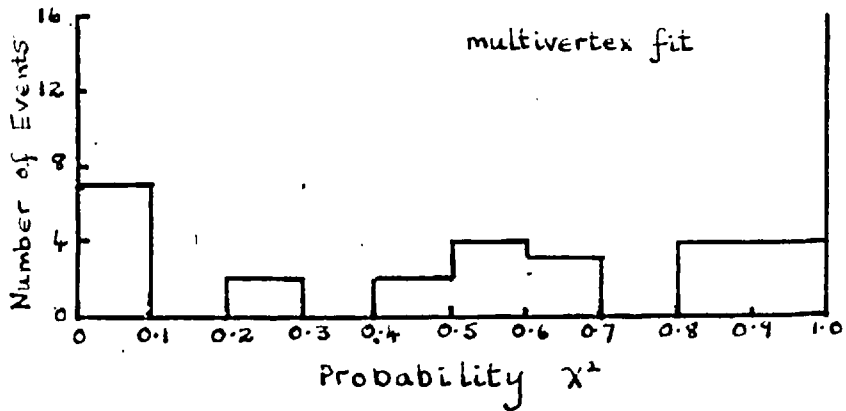
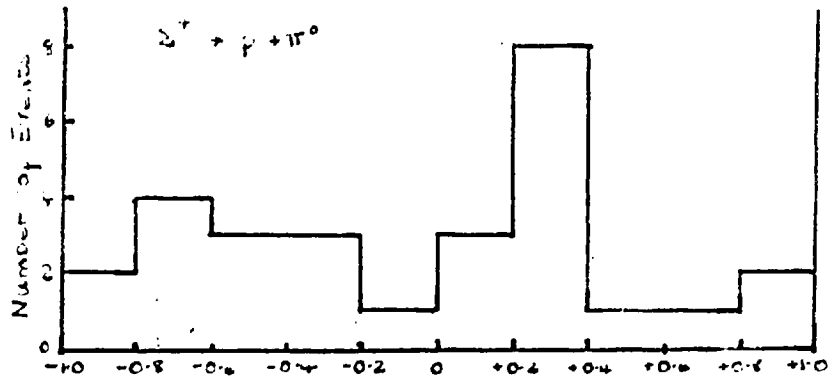
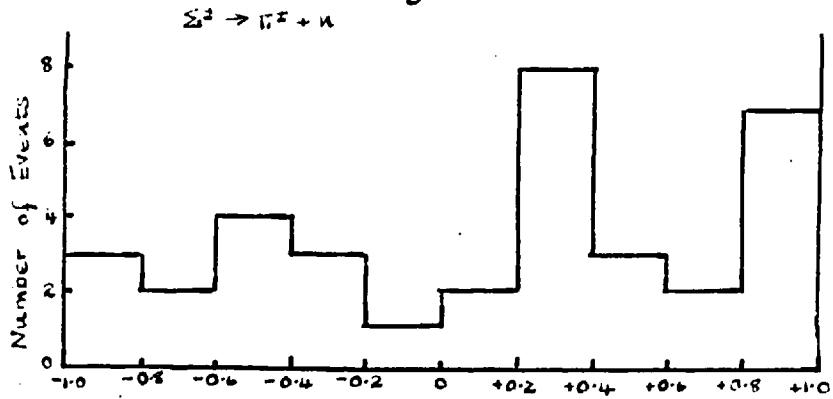


Fig 4.3



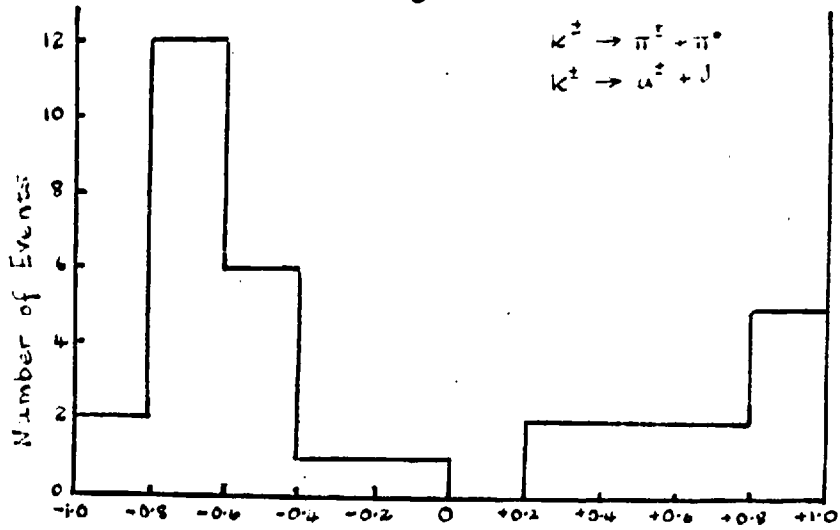
$\cos \theta_p^*$  for  $\Sigma^+$  decay

Fig 4.4



$\cos \theta_\pi^*$  for  $\Sigma^+$  decay

Fig 4.5



$\cos \theta_{\pi,\mu}^*$  for  $K^+$  decay

Fig 4.6

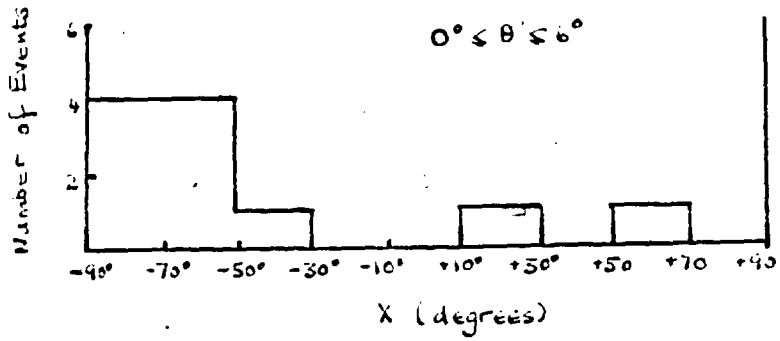


Fig 4.7

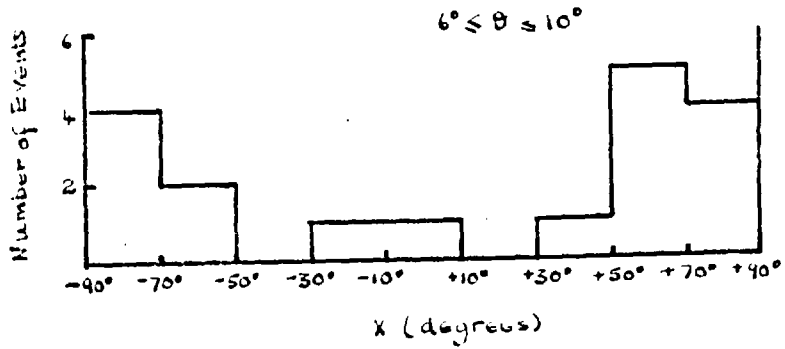


Fig 4.8

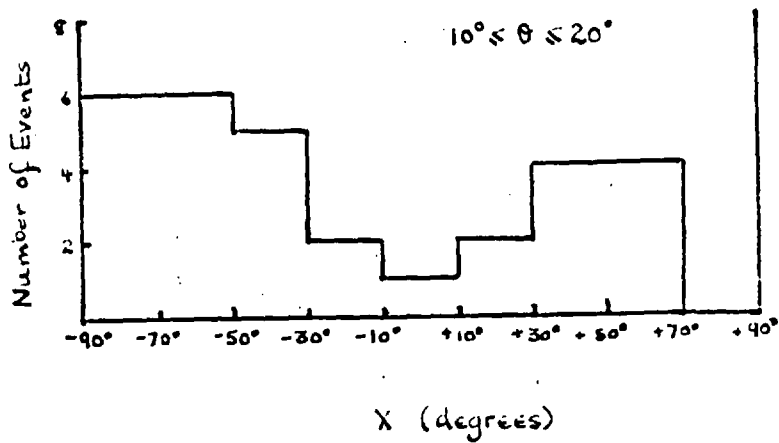


Fig 4.9

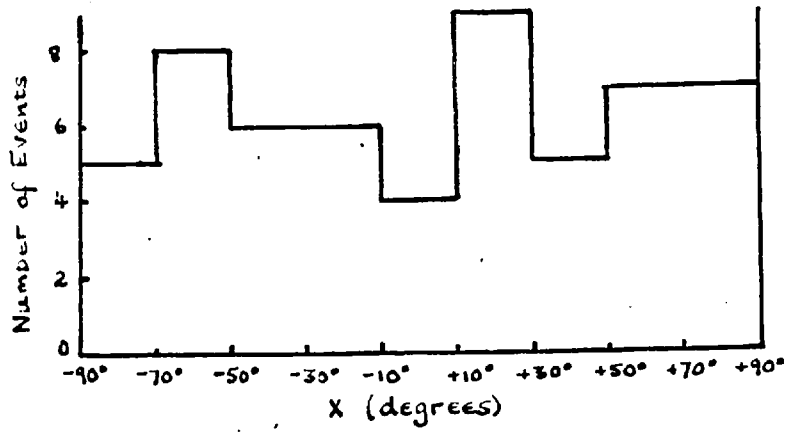


Fig 4.10

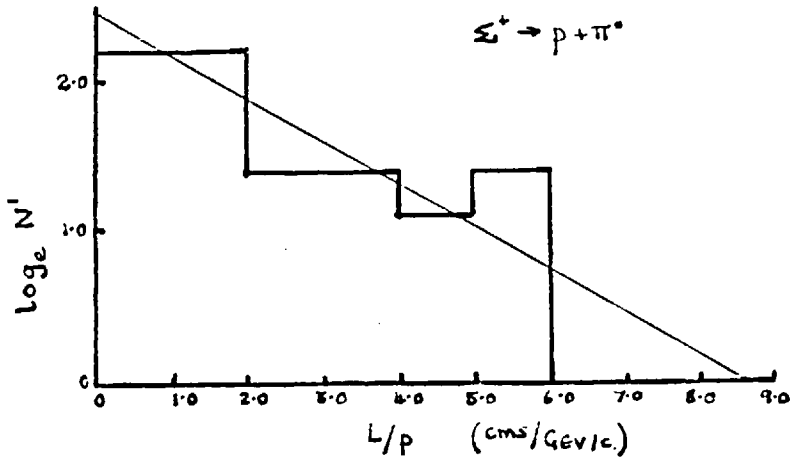


Fig 4.11

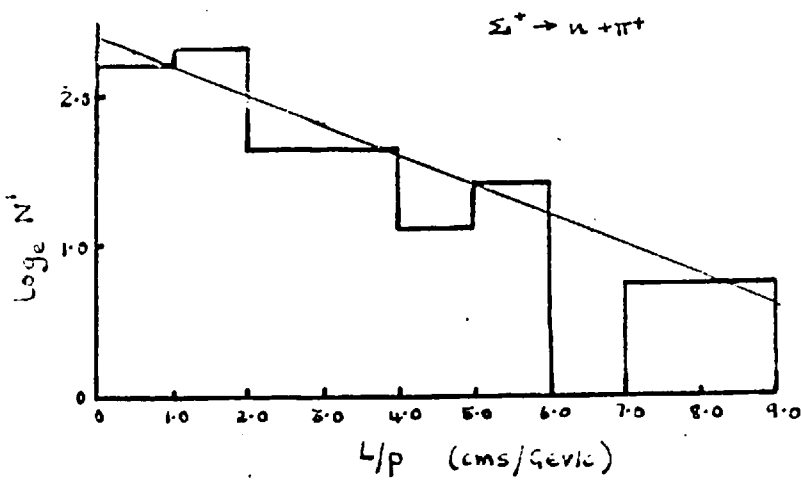


Fig 4.12

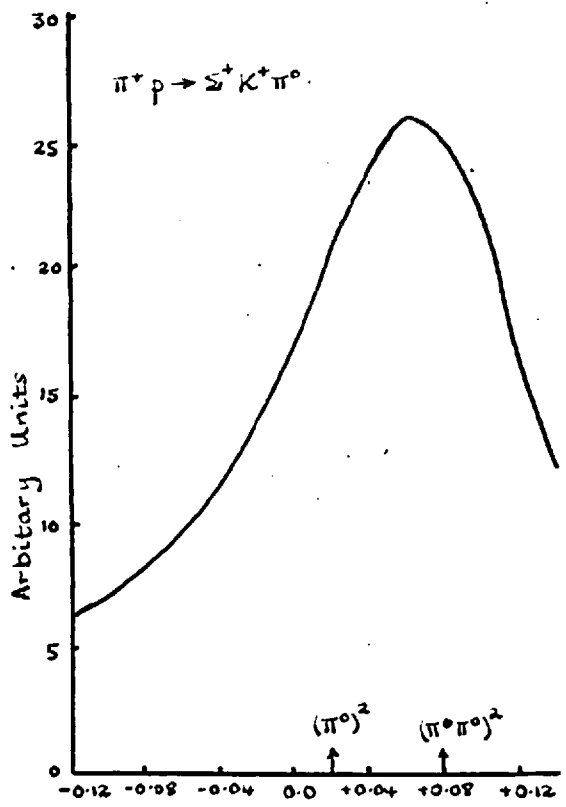


Fig 4.13

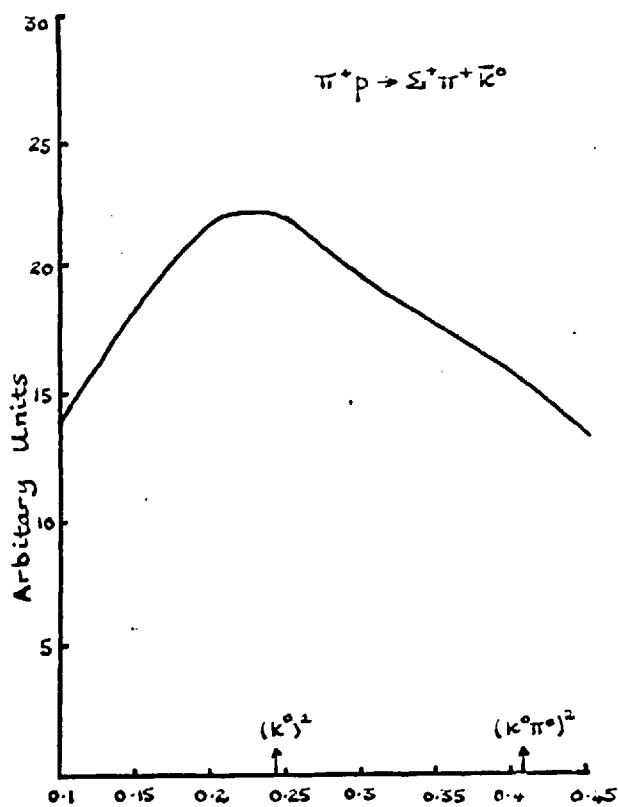


Fig 4.14

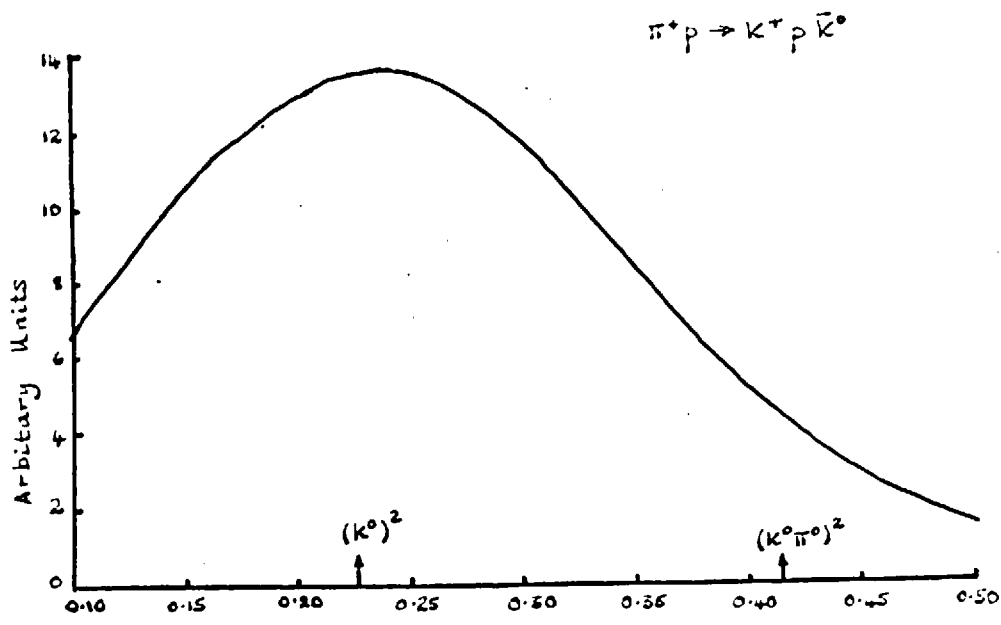


Fig 4.15

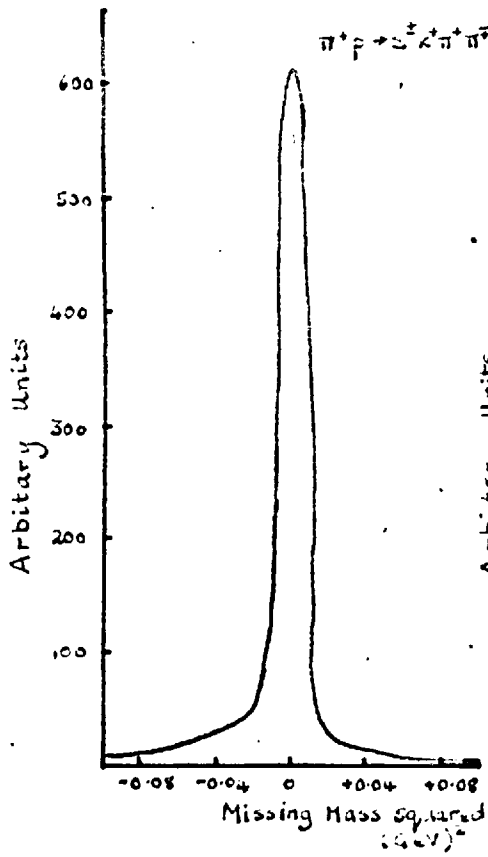


Fig 4-16

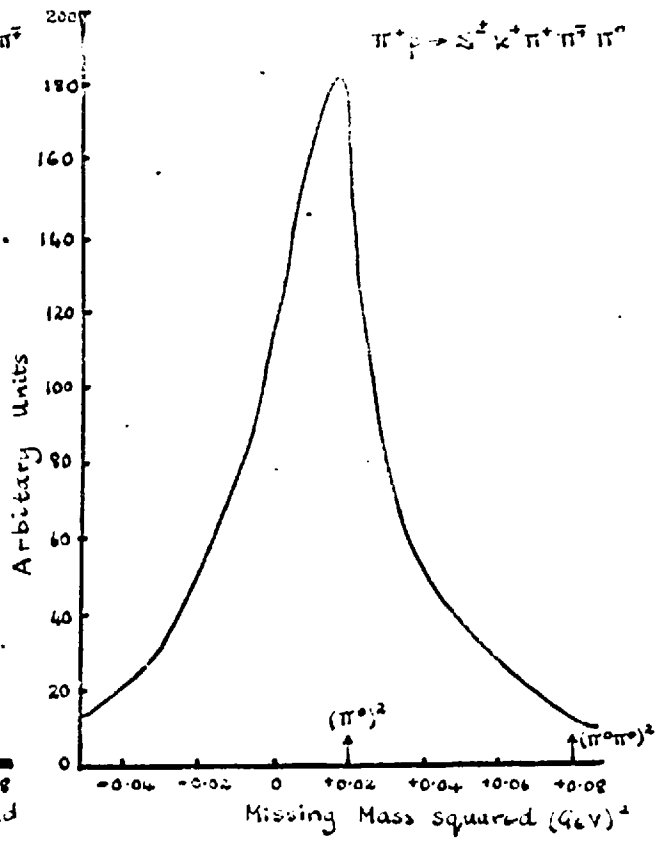


Fig 4-17

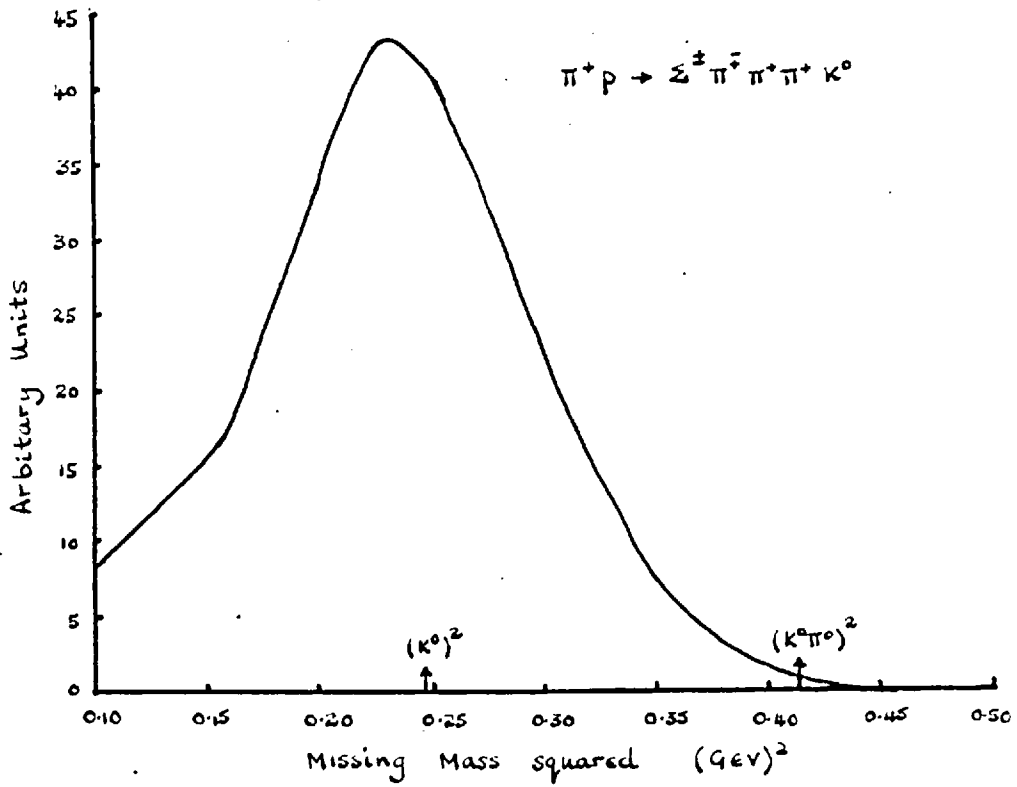


Fig 4-18

CHAPTER 5

GROSS SECTIONS FOR STRANGE PARTICLE PRODUCTION

5.1 The Determination of the Weights

All possible corrections have to be made to the cross-sections before they are finally computed. The corrections for scanning loss and particle decays were discussed in the last two chapters; as well as these, corrections have to be made for neutral (and so unseen) decay modes of the strange particles and for those particles which leave the chamber before decaying.

For all particle decays, the weight is determined; this is the inverse of the probability of detecting that particular event.

The weight is defined by

$$W = \frac{1}{e^{-l/pc\tau} - e^{-L/pc\tau}}$$

where  $m$  = mass of the particle (Gev)

$p$  = momentum of the particle (Gev/c)

$\tau$  = lifetime of the particle (secs.)

$c$  =  $3 \times 10^{10}$  cms/sec<sup>2</sup>

$l$  = imposed lower limit on the distance between the decay vertex and the production apex.

$L$  = potential length.

The two important factors in this expression are  $l$  and  $L$ .  $l$  is set in BAKE to be 0.2 cms when projected in the  $x - y$  plane; i.e. all strange particles which decay within this distance of the apex are rejected. A small correction is made for these events which is generally only significant for  $\Sigma^+$  decays. A correction of 10% has been made for these events.

The potential length is calculated in BAKE for all particle decays. It is defined as follows: suppose that the  $V$  has been moved along the direction of its line of flight until one of the secondary tracks intersected the boundary of the illuminated volume, at the shortest track length allowed. The distance between the two apices is then called the potential length. The minimum track length was set at 5 cms in BAKE as no momentum determination was possible for shorter tracks.

The weight, therefore, gives the correction factor for those events which had a strange particle decay outside the illuminated volume.

The average weights were found to be 1.2 for  $K^0$  decays, 1.1 for  $\lambda$  decays and negligible for  $\Sigma^+$  decays.

These values have been used in all calculations.

## 5.2 Correction $V^0$ events

There are two other corrections to be made for these events in addition to the weight calculated in the previous section,

First, a correction has to be made for the scanning loss. This was determined in Section 3.2 and is 1/99 for 201 events and 1/99.5 for 202 and 401 events.

The second correction is for the neutral decay modes of the  $V^0$ 's.

The two major decay modes of the  $\lambda$  are  $\lambda \rightarrow p + \pi^-$  and  $\lambda \rightarrow n + \pi^0$  with branching ratios of 67% and 31% respectively, so that roughly two thirds of the  $\lambda$  decays are detected. Therefore a correction factor of 3/2 accounts for the neutral decay mode.

For  $K^0$ 's there are two possibilities. Either it decays as  $K_2^0$  which is never detected, or it decays as a  $K_1^0$  whose decay modes are  $K_1^0 \rightarrow \pi^+ + \pi^-$  and  $K_1^0 \rightarrow \pi^0 + \pi^0$  with branching ratios of 69% and 22 % respectively.

Therefore the total probability of observing a  $K^0$  as a  $K_1^0$  is given by

$$\begin{aligned} & (\text{probability of observing as } K_1^0) \times (\text{probability of detecting the } K_1^0) \\ & = \left(\frac{1}{2} \times \frac{2}{3}\right) = \frac{1}{3} \end{aligned}$$

so that for events where one  $K^0$  is produced a correction factor of 3 is required.

For events with  $K^0\bar{K}^0$  pairs the following corrections are required. The  $K^0\bar{K}^0$  pair can be produced as a  $K_1^0\bar{K}_1^0$ ,  $K_2^0\bar{K}_2^0$  or  $K_1^0\bar{K}_2^0$  pair. A correction always has to be made for the  $K_2^0\bar{K}_2^0$  pair.

As approximately two thirds of the  $K_1^0$  decays are detected, the probabilities of observing the  $K_1^0 K_1^0$  pair are as follows. If both  $K_1^0$ 's are seen to decay, the event is classified as a 202 and the probability of seeing this is  $(\frac{2}{3} \times \frac{2}{3}) = 4/9$ . If, however, only one  $K_1^0$  decay is seen, the event is identified as a 201 and the probability of seeing this is  $2 \times (2/9) = 4/9$ ; the factor of two is included as either  $K_1^0$  decay can be detected. The probability of not observing either  $K_1^0$  decay is  $(\frac{1}{3} \times \frac{1}{3}) = 1/9$ .

Therefore the correction factor for  $K_1^0 K_1^0$  pairs seen as 202 events is 5/4; also from the observed number of  $K_1^0 K_1^0$  pairs in the 202 events, the expected number of  $K_1^0 K_1^0$  pairs in the 201 events can be estimated.

The  $K_1^0 K_2^0$  pairs are only detected in the 201 events as only the  $K_1^0$  decay is seen. As the expected number of  $K_1^0 K_1^0$  pairs in the 201 events is known the number of events with  $K_1^0 K_2^0$  pairs can be estimated; a correction factor of 3/2 then accounts for the unseen  $K_1^0 K_2^0$  pairs.

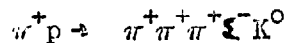
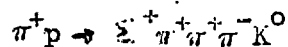
### 5.3 Corrections for $V^+$ events

Several corrections are necessary for events with these decays. The correction for the scanning loss was determined in Section 3.2 to be 1/97.4 for 201 events and 1/94 for 410 events.

For all  $K^+$  decays a 10% correction had to be made for all

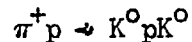
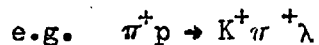
those decays occurring within 0.2 cms of the apex. An additional correction was necessary for the  $\Sigma^+ \rightarrow p + \pi^0$  decay mode to account for the loss of small angle decays. From the analysis of the angle X this loss was estimated in Section 4.2, to occur for all decay angles of  $6^\circ$  or less. A 15% correction accounted for these events.

In determining the cross-sections for the reactions



the few 211 and 411 events observed with a  $\Sigma^+$  decay and a  $K_1^0$  have not been used, but these are included in the correction factor of 3/2 applied to the 210 and 410 events.

All events with an observed  $K^+$  decay have not been used in the determination of the cross-sections as they would give a biased sample. For channels which were common to both the 201 and 210 event types



the 210 events have not been used to determine the cross-sections. These are included in the correction factor applied to the 201 events for the neutral decay mode of the  $V^0$ .

#### 5.4 Cross-Section Determination

The results from all four groups, Aachen, Hamburg, Imperial College and Munich are used in the cross-section calculations. As it was not possible to determine the scanning biases and corrections for the German groups, the corrections determined at Imperial College have been applied to the data. This may be a source of error as it is very unlikely that the scanning efficiency was the same for all groups; however, as the corrections are usually small, the effect on the calculated cross-sections should be negligible.

The cross-section is defined as

$$\sigma = \frac{N}{\rho A l n \bar{B}}$$

where N = number of events

$\rho$  = density of liquid hydrogen = 0.0625 gm/cc

$A_0$  = Avogadro's Number =  $6.03 \times 10^{23}$  mols/gm mol

l = length of fiducial volume at the mean z position

n = total number of frames scanned

$\bar{B}$  = average number of beam tracks per picture.

Using the total number of events for each group given in Table 2 of Chapter 3 and the following values of  $ln\bar{B}$

Imperial College	l = 54 cms.	$ln\bar{B} = 9.828 \times 10^6$ cms.
Aachen	l = 56 cms.	$ln\bar{B} = 7.023 \times 10^6$ cms.
Hamburg	l = 45 cms.	$ln\bar{B} = 4.834 \times 10^6$ cms.
Munich	l $\approx$ 60 cms.	$ln\bar{B} \approx 10.383 \times 10^6$ cms.

the total cross-sections for each group were determined and are given in Table 5.1.

The figures for the Munich data are approximate, as the values for  $l$  and  $\ln \bar{B}$  are unknown. They were estimated by assigning the average total cross-section for the Aachen and Imperial College groups to the Munich results and so determining  $\ln \bar{B}$ , which was used to calculate all the other cross-sections. This introduces an error of approximately 10% in all further calculations.

The cross-sections for the 4-prong  $\bar{L}^+$  events and the 2-prong events are shown in Table 5.1.

As the number of events in any channel with more than one neutral is unknown, no cross-sections for these channels can be determined. In Table 2 of Chapter 3 it was seen that about 17% of all events were of this type, so that the cross-section for all multi-neutral events is approximately 149  $\mu\text{b}$ .

It can also be seen from Table 5.1 that the Hamburg results are in disagreement with those obtained for the other groups. It appears that the cross-sections for the Hamburg results are consistently too low. The reason for this discrepancy is unknown, but it introduces another error into the cross-section calculations so that it is only reasonable to quote these values with a large percentage error estimated to be  $\pm 30\%$ .

In most cases this error is sufficient to include the error arising from including events with more than one neutral particle in the fitted channels. There was, however, considerable contamination in the following channels

$$\pi^+ p \rightarrow \Sigma^+ K^+ \pi^0$$

and

$$\pi^+ p \rightarrow \Sigma^+ \pi^+ K^0$$

The missing mass squared ideograms for these channels were given in Figures 4.13 and 4.14 respectively. It was estimated that perhaps the contamination was as much as 20%, but the statistics are poor as only Imperial College events are included in these plots.

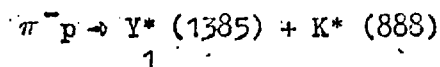
Therefore a larger error (40%) is quoted on the cross-sections for these channels.

The resonance production cross-sections are shown in Table 5.2 This demonstrates that  $Y_1^*$  (1385) and  $K^*$  (898) are the resonances predominantly produced. From experiments at lower energies<sup>(16,17,18)</sup> this was expected, although the relative production rates of these resonances in some reactions are quite different at this high energy. These reactions are discussed in detail in the next Chapter.

### 5.5 Strange particle production in 4 GeV/c $\pi^+ p$ & $\pi^- p$ Interactions

In the  $\pi^- p$  experiment at the same incident pion momentum, 722 strange particle events were analysed. This gave a total cross-section of  $2.52 \pm 0.25$  mb<sup>(1)</sup>.

Small amounts of  $Y_1^*$  (1385) and  $K^*$  (888) production were seen, but there was no copious production of these resonances which was the feature of the  $\pi^+p$  strange particle interactions. However, in the  $\pi^-p$  interactions the quasi-two body reaction



is significantly produced while it is not seen at all in the  $\pi^+p$  interactions.

In both experiments the baryon tends to be peaked backwards in the centre of mass system indicating that the peripheral model can explain most of the reactions.

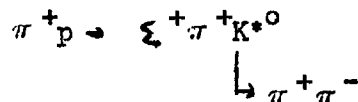
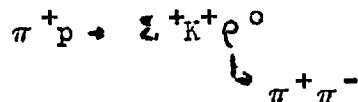
### 5.6 The 4-prong strange particle reactions

The statistics for most of these reactions are very poor.

In the main reaction

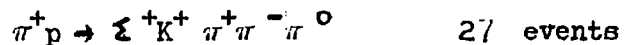


there is some  $e^0$  and  $K^{*0}$  (888) production. The cross-sections for the reactions



were estimated to be  $12 \mu\text{b}$  and  $14 \mu\text{b}$  respectively.

In the only other significant reaction



there is perhaps a little  $\omega^0$  production but all other distributions agree with the phase space predictions.

In all  $\Sigma^+$  4-prong events, the  $\Sigma$ 's tend to be produced in the backward direction, though this is not so strong as in the two prong events. This is consistent with what one would expect as the interaction becomes less peripheral.

TABLE 5.1

CROSS-SECTIONS

Reaction	Total ( $\mu\text{b}$ )	I.C. ( $\mu\text{b}$ )	Aa. ( $\mu\text{b}$ )	Ha. ( $\mu\text{b}$ )	Mu. ( $\mu\text{b}$ )
$\pi^+ p \rightarrow K^+ \Lambda / \Sigma$	74	76	107	36	85
$\pi^+ p \rightarrow K^+ \pi^+ \Lambda \pi^0$	117	134	107	55	135
$\pi^+ p \rightarrow \pi^+ \pi^+ K^0 \Lambda / \Sigma^0$	112	166	82	65	129
$\pi^+ p \rightarrow p \pi^+ K^0 \bar{K}^0$	94	118	167	25	73
$\pi^+ p \rightarrow p \pi^+ K_1^0 K_2^0$	37	54	55	20	19
$\pi^+ p \rightarrow p \pi^+ K_1^0 K_1^0$	28	26	50	0	25
$\pi^+ p \rightarrow K^+ p K^0$	50	59	54	40	47
$\pi^+ p \rightarrow K^+ p K_1^0 \pi^0$	56	78	41	60	44
$\pi^+ p \rightarrow K^+ \pi^+ K_1^0 n$	62	68	41	40	83
$\pi^+ p \rightarrow \Sigma^+ K^+$	45	28	66	25	59
$\pi^+ p \rightarrow \Sigma^+ K^+ \pi^0$ *	51	26	62	53	68
$\pi^+ p \rightarrow \Sigma^+ \pi^+ K^0$ *	56	46	90	9	46
$\pi^+ p \rightarrow \Sigma^+ \pi^+ K^0 \pi^0$	22	11	?	0	59
$\pi^+ p \rightarrow \Sigma^+ K^+ \pi^+ \pi^-$	45	34	51	27	60
$\pi^+ p \rightarrow \Sigma^+ K^+ \pi^+ \pi^- \pi^0$	28	30	23	6	38
$\pi^+ p \rightarrow \Sigma^+ \pi^+ \pi^+ \pi^- K^0$	9	13	9	7	6
$\pi^+ p \rightarrow K^+ \pi^+ \pi^+ \Sigma^-$	5	6	4	0	6
$\pi^+ p \rightarrow K^+ \pi^+ \pi^+ \Sigma^- \pi^0$	6	3	4	6	9
$\pi^+ p \rightarrow \pi^+ \pi^+ \pi^+ \Sigma^- K^0$	5	13	0	0	6
$\pi^+ p \rightarrow K^+ \pi^+ \pi^+ \pi^- \Lambda / \Sigma^0$	18	26	?	9	?
Multineutral events	149	114	175	135	155
Total	1049	1027	1169	810	1098

all cross sections have  $\pm 30\%$  error

\* cross-section error of  $\pm 40\%$

TABLE 5.2

<u>Reaction</u>	<u>Resonance</u>	<u>Cross-section</u>
$\pi^+ p \rightarrow K^+ \pi^+ \lambda$	$Y_1^{*+} (1385)$	22 $\mu b$
$\pi^+ p \rightarrow K^+ \pi^+ \lambda \pi^0$	$Y_1^{*+} (1385)$	41 $\mu b$
	$Y^{**} \rightarrow Y_1^{*+} (1385) + \pi^0$	12 $\mu b$
	$Y_1^{*+} (1385) + K^{*+} (888)$	< 8 $\mu b$
$\pi^+ p \rightarrow \pi^+ \pi^+ \lambda K^0$	$K^{*+} (888)$	65 $\mu b$
	$K^{*+} (888) + Y_1^{*+} (1385)$	< 15 $\mu b$
$\pi^+ p \rightarrow p \pi^+ K_1^0 K_2^0$	$\rho + N^{*++} (1238)$	< 1.4 $\mu b$
$\pi^+ p \rightarrow K^+ p K^0$	$A_2 \rightarrow K^+ K^0$	13 $\mu b$
$\pi^+ p \rightarrow \Sigma^+ \pi^+ K^0$	$K^* (888)$	17 $\mu b$
	$K^* (1400)$	8 $\mu b$
$\pi^+ p \rightarrow \Sigma^+ K^+ \pi^0$	$K^* (888)$	6 $\mu b$
$\pi^+ p \rightarrow \Sigma^+ K^+ \pi^+ \pi^-$	$K^* (888)$	14 $\mu b$
	$\rho^0$	12 $\mu b$

CHAPTER 6

DISCUSSION OF 2-PRONG STRANGE PARTICLE REACTIONS

In this chapter the 2-prong strange particle reactions are discussed. As the statistics are poor, only the resonance production is considered and the results obtained discussed with reference to work at lower incident  $\pi^+$  momentum.

6.1 The reaction  $\pi^+ p \rightarrow K^+ \pi^+ \lambda \pi^0$

Eighty-five 201 events were identified as belonging to the reaction

$$\pi^+ p \rightarrow K^+ \pi^+ \lambda \pi^0 \quad (1)$$

which gave a cross-section of  $117 \mu b^{\pm} 30\%$ .

This reaction was dominated by strong  $Y_1^{*+} (1385) \rightarrow \lambda \pi^+$  production as shown in Figure 6.1 which shows the effective mass distribution for the  $\lambda \pi^+$  combination, compared with a phase space normalised to all events outside the  $Y_1^{*+}$  region (1.34 - 1.44 Gev). About 42% of the events were of the channel

$$\pi^+ p \rightarrow Y_1^{*+} (1385) + K^+ + \pi^0 \quad (2)$$

$$\downarrow$$

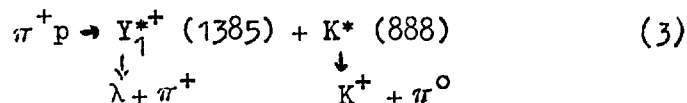
$$\lambda + \pi^+$$

corresponding to a cross-section of  $41 \mu b$ .

The  $Y_1^{*+} (1385)$  is produced in a peripheral process, as is shown by the strong backward peaking of the centre of mass angular distribution (Figure 6.2)

It is a feature of the pion interactions <sup>(2-9)</sup> that quasi-two

body interactions formed a large fraction of the peripheral processes, so that it was expected that there should be significant production of the channel.



which would be described by the diagram in Figure 6.3.

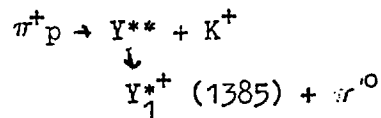
The scatter diagram for the  $\lambda\pi^+$  and  $K^+\pi^0$  effective masses is shown in Figure 6.4 where the  $K^*$  (0.84 - 0.96 Gev) and  $Y^*$  (1.34 - 1.44 Gev) regions are indicated by the dotted lines. The projection for the  $K^+\pi^0$  effective mass is shown in Figure 6.5, the shaded area representing the distribution for events with the  $\lambda\pi^+$  effective mass lying in the  $Y_1^{*+}$  (1385) region.

It is obvious that very little  $K^*$  (888) is produced in this reaction and that it is not preferentially produced in association with the  $Y_1^{*+}$  (1385). From Figure 6.4, the cross-section for Reaction (3) was estimated to be  $\leq 8 \mu\text{b}$ , so the data was insufficient for a Gottfried-Jackson analysis <sup>(45-51)</sup> to be used to determine the exchange mechanism.

All the other effective mass distributions for this channel are in agreement with those predicted by phase space except that for the  $\lambda\pi^+\pi^0$  combination. Figure 6.6 shows this distribution compared with a phase space normalised to all events.

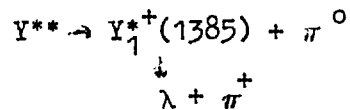
A small enhancement is observed in the mass region

(1.84 - 1.92 Gev), which, in itself, is not significant. If, however, the distribution is redrawn (Figure 6.7) for those events where the  $\lambda\pi^+$  effective mass lies in the  $Y_1^{*+}$  (1385) region, then the enhancement becomes a two standard deviation effect. Nearly all the background has been removed and if the distribution is compared with a phase space normalised to the events outside this region then there are 8 events above phase space and the cross-section for the reaction



was estimated to be 12  $\mu\text{b}$ . The centre of mass angular distribution for this enhancement is shown in Figure 6.8, but as there are so few events it is impossible to say whether it is produced by a peripheral interaction.

The following values are obtained for the quantum numbers of this enhancement.



$$M(Y^{**}) = 1.884 \text{ Gev} \quad \Gamma(Y^{**}) \approx 80 \text{ Mev.}$$

$$Q = B = +1 \quad S = -1 \quad \therefore I_3 = +1 \text{ and } I \geq 1$$

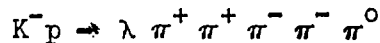
This implies that  $J \geq 3/2$  with the parity completely undetermined.

The only other evidence for a particle in this mass region

decaying in this way was presented by Belyakov et al (62) who studied the interaction of 7-8 GeV/c  $\pi^-$  in propane; an enhancement was observed in the ideogram for the effective mass of the  $\lambda \pi^+ \pi^-$  combination for stars with two outgoing tracks. When the  $\lambda \pi^+$  effective mass distribution was drawn for these events it was found to peak strongly at the  $Y_1^*$  (1385) mass. This implied a  $Y_1^* (1385) + \pi^-$  decay mode and the mass of this  $Y^{**}$  was estimated to be  $1770 \pm 100$  MeV.

It is possible to consider that although the two estimated masses for this  $Y^{**}$  are vastly different, both enhancements are really due to the same resonance.

There is some further tentative evidence for this resonance in 6 GeV/c  $K^-p$  interactions but the data is only partially analysed (63). The preliminary results for the channel



show an enhancement in the effective mass of the  $\lambda \pi^+ \pi^-$  combination at a mass of 1.85 GeV and with a width of about 100 MeV. Unfortunately this distribution has not been replotted for those events where the  $\lambda \pi^+$  effective mass lies in the  $Y_1^*$  (1385) region.

The centre of mass production angular distribution for the  $\lambda$ ,  $K^+$ ,  $\pi^+$  and  $\pi^0$  are shown in Figures 6.9 - 6.12 respectively. These distributions show that the peripheral model can only explain some features of this reaction.

6.2 The reaction  $\pi^+ p \rightarrow \pi^+ \pi^+ \lambda K^0$

The reaction

$$\pi^+ p \rightarrow \pi_a^+ \pi_b^+ \lambda K^0 \quad (1)$$

can be identified in the 201 and 202 events in three different ways with a total cross-section of  $112 \mu b \pm 30\%$ :-

$$\pi^+ p \rightarrow \pi^+ \pi^+ \lambda (K^0) \quad \lambda \text{ detected in 201 events} \quad (2)$$

$$\pi^+ p \rightarrow \pi^+ \pi^+ K_1^0 (\lambda) \quad K_1^0 \text{ detected in 201 events} \quad (3)$$

$$\pi^+ p \rightarrow \pi^+ \pi^+ K_1^0 \lambda \quad \text{both } \lambda, K_1^0 \text{ detected in 202 events} \quad (4)$$

It is difficult to separate reaction (1) from the almost identical reaction

$$\pi^+ p \rightarrow \pi^+ \pi^+ K^0 \Sigma^0.$$

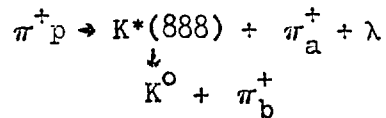
Contamination due to this reaction can be removed from channels (3) and (4) as it was possible to fit for the  $\Sigma^0$  directly. In reaction (2), however, this was not possible and the contamination was estimated to be  $\leq 15\%$ .

As there were 43 events belonging to reaction (2) the contamination is about four events and so is negligible. 69 events altogether of reaction (1) were identified and have been used in all distributions.

The scatter diagram of the  $\pi_b^+ K^0$  and  $\pi_a^+ \lambda$  effective masses is shown in Figure 6.13 with the  $K^*$  (0.84 - 0.96 Gev) and  $Y_1^*$  (1.32 - 1.44) regions indicated by the dotted lines. The projections from this plot are shown in Figures 6.14 and 6.15 for

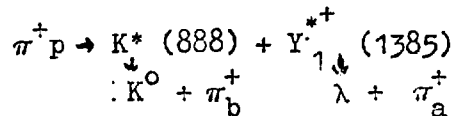
the  $K^0 \pi_b^+$  and  $\lambda \pi_a^+$  effective masses respectively. The shaded area in Figure 6.15 shows the distribution obtained for those events where the  $K^0 \pi_b^+$  effective mass lay in the  $K^*$  (888) region.

Strong  $K^*(888)$  production is observed and the centre of mass angular distribution for the  $K^*$  (Figure 6.16) shows that, as expected, the  $K^*$  is produced peripherally. The cross-section for the process



was estimated to be 65  $\mu\text{b}$ .

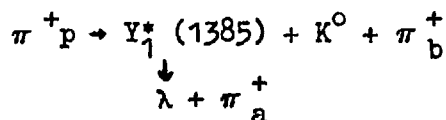
There appears to be little or no  $Y_1^*$  (1385) production and so the cross-section for the reaction



is very low  $\leq 15 \mu\text{b}$ .

All other effective mass distributions are well described by phase space. The centre of mass angular distributions for the  $\lambda$ ,  $K^0$  and  $\pi^+$  are shown in Figures 6.17, 6.18 and 6.19 respectively.

Reaction (1) has been reported in detail by Yamamoto et al <sup>(17)</sup> at an incident  $\pi^+$  momentum of 2.77 GeV/c. At this energy the reaction was dominated by strong  $Y_1^*$  (1385) production; i.e. by the process



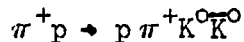
with a cross-section of approximately  $32 \mu\text{b}$ .

This result is in complete disagreement with that obtained in the present experiment where  $K^*(888)$  production is predominant.

At  $3.55 \text{ GeV}/c$  incident  $\pi^+$  momentum <sup>(18)</sup>, a detailed analysis of this reaction is not available but it is thought that both  $Y_1^*$  (1385) and  $K^*(888)$  were observed as there was some evidence for the associated production of these two resonances. This suggests that the dominance of  $K^*(888)$  production over  $Y_1^*$  (1385) is gradual with increasing energy.

### 6.3 The reaction $\pi^+ p \rightarrow p \pi^+ K^0 \bar{K}^0$

Forty-five events of the type 201 and 202 were found to proceed by the reaction



with a cross-section of  $94 \mu\text{b} \pm 30\%$ .

This reaction could be detected in two different channels



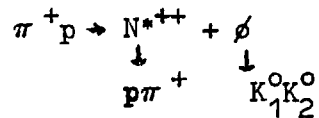
Thirty-five 201 events and ten 202 events were found in channels (1) and (2) with cross-sections of  $37 \mu\text{b}$  and  $28 \mu\text{b}$  respectively.

As the statistics are not sufficient to treat these two channels separately, the distributions for channels (1) and (2)

will be plotted on the same graph. In all cases the shaded areas represent events of channel (2).

There appears to be little or no resonance production in this channel. The scatter diagram for  $M(p\pi^+)$  against  $M(K^0\bar{K}^0)$  is given in Figure 6.20. The dotted lines indicate the  $N^{*++}$  region (1.12 - 1.32 Gev). There is some  $N^{*++}$  production but there are no significant enhancements in the  $K^0\bar{K}^0$  effective mass. The projections for these effective masses are shown in Figures 6.21 and 6.22 respectively compared with phase spaces normalised to all events.

For the  $K^0\bar{K}^0$  distribution there appears to be complete disagreement with the theoretical distribution for reaction (1) which is difficult to explain. In particular there is little or no  $\phi \rightarrow K_1^0 K_2^0$  production which is in complete contradiction to the results published at 2.77 Gev/c incident  $\pi^+$  momentum (17) where 66% of the events of channel (1) were of the reaction



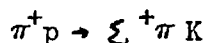
and the cross-section was estimated to be 8.5  $\mu\text{b}$ . At 4 Gev/c incident  $\pi^+$  momentum, the upper limit on the cross-section is  $< 1.5 \mu\text{b}$ .

All other effective mass distributions are essentially consistent with phase space. The centre of mass production angles

for the  $\pi^+$ , proton and  $K^0$  are shown in Figures 6.23, 6.24 and 6.25 respectively.

6.4 The reaction  $\pi^+ p \rightarrow \Sigma^+ \pi^0 K^+$

98 events were identified as the reaction



which was observed in the two channels

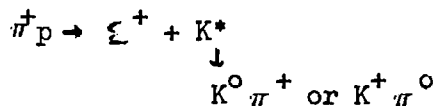
$$\pi^+ p \rightarrow \Sigma^+ \pi^+ K^0 \quad 47 \text{ events } \quad 210, 211 \text{ event types} \quad (1)$$

$$\pi^+ p \rightarrow \Sigma^+ K^+ \pi^0 \quad 51 \text{ events } \quad 210 \text{ event types only} \quad (2)$$

with cross-sections of  $56 \mu\text{b} \pm 40\%$  and  $51 \mu\text{b} \pm 40\%$  respectively.

The Dalitz plots for the two reactions are shown in Figure 6.26 and 6.27 respectively; the  $K^*$  (888) region (0.84 - 0.96 Gev) is indicated by the dotted lines. The projections for the  $K\pi$  effective masses are shown in Figures 6.28 and 6.29 respectively, and these distributions are compared with phase spaces normalised to all events outside the  $K^*$  region.

In both channels there is some  $K^*$  (888) production which is, as expected, stronger in channel (1). The cross-section for the reaction



was estimated to be  $23 \mu\text{b}$ . For the study of  $K^*$  production it is reasonable to treat both reactions together. The centre of mass

production angles for the  $\xi^+$ ,  $K^0$  and  $\pi^+$  of reaction (1) are shown in Figures 6.30, 6.32 and 6.33 respectively and those for the  $\xi^+$ ,  $K^+$  and  $\pi^0$  from reaction (2) in Figures 6.31, 6.34 and 6.35.

In both cases these distributions show that these reactions are mainly peripheral, so that  $K^*$  production can be described by the diagram in Figure 6.36 where both K and  $K^*$  exchange are possible.

As the background under the  $K^*$  peak is very low ( $\leq 20\%$ ) all events in the  $K^*$  peak have been used in an attempt to determine the ratio of K to  $K^*$  exchange by a Gottfried and Jackson analysis.

At lower energies this ratio was found to be 50% (17, 20).

Consider the upper vertex in Figure 6.36; for  $K^*$  exchange

$$\begin{array}{l} \pi^+ + K^* \rightarrow K^* + L \\ \text{(angular momentum) Parity} \quad 0^- + 1^- \rightarrow 1^- + |L, 0\rangle \end{array}$$

where  $L$  is the orbital angular momentum; parity conservation requires  $L$  to have negative parity so that  $L = 1$  is the lowest state allowed by angular momentum conservation. Now  $L_z = 0$  along the chosen axis of quantization (the direction of the incident  $\pi^+$  in the  $K^*$  centre of mass) so that the  $K^*$  is forced to be in a  $|1, \pm 1\rangle$  spin state. This means that the spin state is described by the spherical Harmonic  $|Y_1^{\pm 1}|^2$  and so the Cos  $\theta$

distribution is proportional to  $\text{Sin}^2\theta$ ; similarly it can be shown that for K exchange the spin state is described by  $|Y_1^0|^2$  and so the  $\text{Cos } \theta$  distribution will be proportional to  $\text{Cos}^2\theta$ .

$\text{Cos } \theta$  and  $\phi$  are shown in Figures 6.38 and 6.39 respectively. The vectors required to define these angles are shown in Figure 6.37 and are defined in the  $K^*$  centre of mass.

Then  $\text{Cos } \theta$  and  $\text{Cos } \phi$  are defined by

$$\text{Cos } \theta = \frac{\vec{p}_{\pi_{in}^+} \cdot \vec{p}_{\pi_{out}}}{|\vec{p}_{\pi_{in}^+}| \cdot |\vec{p}_{\pi_{out}}|} \quad \text{Cos } \phi = \frac{(\vec{p}_{\pi_{in}^+} \times \vec{p}_p) \cdot (\vec{p}_p \times \vec{p}_{\pi_{out}})}{|\vec{p}_{\pi_{in}^+} \times \vec{p}_p| \cdot |\vec{p}_p \times \vec{p}_{\pi_{out}}|}$$

Although the statistics are poor it has been attempted to fit these distributions to the theoretical expressions for  $\text{Cos } \theta$  and  $\phi$  given in Section 7.2. The fitting was done using the method of least squares although the validity of this method is in doubt when dealing with such a small number of events.

Figures 6.38 and 6.39 show the experimental and theoretical distributions for  $\text{Cos } \theta$  and  $\phi$ . The values of  $\chi^2$  obtained for the fits to these distributions were 15 for the  $\text{Cos } \theta$  distribution (7 degrees of freedom) and 15 for the  $\phi$  distribution (10 degrees of freedom). These values correspond to low probabilities of  $\chi^2$  and either indicate a genuine divergence from Gottfried and Jackson's theory or confirm that least squares fitting to such a small number of events is unrealistic.

Nevertheless, the following values for the elements of the density matrix for a spin one particle were obtained (these are discussed in more detail in Chapter 7).

$$\rho_{00} = 0.271 \pm 0.188 \quad \rho_{1-1} = 0.193 \pm 0.119$$

This leaves  $\rho_{10}$  as the only undetermined parameter. It was not possible to calculate the real part of  $\rho_{10}$  as the data necessary for finding the expectation value  $\langle \sin 2\theta \cos \phi \rangle$  was unavailable.

From the above values it is not possible to make any definite estimate of the ratio of pseudoscalar to vector exchange.

All that can be said is that neither of these exchange mechanisms is predominant over the other as for pseudoscalar exchange  $\rho_{00}$  should be the only non-zero matrix element, i.e.  $\rho_{00} \sim 1, \rho_{1-1} = 0$ ; while for vector exchange  $\rho_{00} = 0$  and  $\rho_{10} \sim 1$ .

This means that at this energy which is considerably higher than any other at which this reaction was studied (17), this reaction still proceeds by a mixture of K and K\* exchange, where the ratio of K to K\* exchange is undetermined.

The only other interesting feature in this reaction is seen in channel (1)

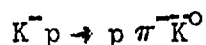


In the dalitz plot shown in Figure 6.26, the distribution of the points shows a very definite structure, as they appear to

fall into two  $K^0 \pi^+$  effective mass regions. One region is due to  $K^*$  (888) production but the other seems to be centred around a  $K^0 \pi^+$  effective mass a little below 1.4 Gev.

This is seen more clearly in the projection (Figure 6.28) which is compared with a phase space normalised to all events outside the  $K^*$  (888). A second enhancement is seen in the region 1.2 - 1.48 Gev.

Recently the existence of a second  $K^*$  has been reported by two groups; the first studied the reaction



at an incident  $K^-$  momentum of 3.5 Gev/c <sup>(64)</sup>. A peak was observed in the  $\pi^- \bar{K}^0$  effective mass distribution, besides the  $K^*$  (888), at a mass of 1.4 Gev and a width of 160 Mev. The ratio of  $K^*$  (888),  $K^*$  (1400) and background production was estimated to be 0.59: 0.22: 0.18.

Further evidence for this  $K^*$  (1400) was obtained by studying the reactions



191 events



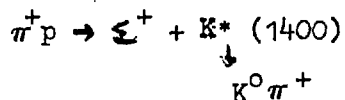
160 events

at an incident  $\pi^-$  momenta of 3.9 and 4.2 Gev/c <sup>(65)</sup>. A similar peak was observed in the  $\pi^- K^+$  effective mass distribution with 68 events in the region 1.35 - 1.51 Gev where phase space predicts only 32-36 events. This enhancement probably has  $I = \frac{1}{2}$

because it is not observed in other channels where the production of an  $I = 3/2$   $K^*$  (1400) would be favoured.

This enhancement was not observed in  $\pi^- p$  interactions at 4 GeV/c because of the poor statistics (1).

In the present experiment, although the statistics are very poor compared with the two experiments quoted here, it is perhaps possible to interpret this enhancement as further evidence for the existence of the  $K^*$  (1400). This would give a cross-section of  $8 \mu\text{b}$  for the reaction



which leads to the following values for the ratios of the cross-sections.

$K^*$  (888) :  $K^*$  (1400) : background

0.30            0.14            0.56

These are in agreement for the ratio of  $K^*$  (888) to  $K^*$  (1400) production but the background seems to be much larger. This could possibly be explained by the contamination present in this channel due to events with many neutrals.

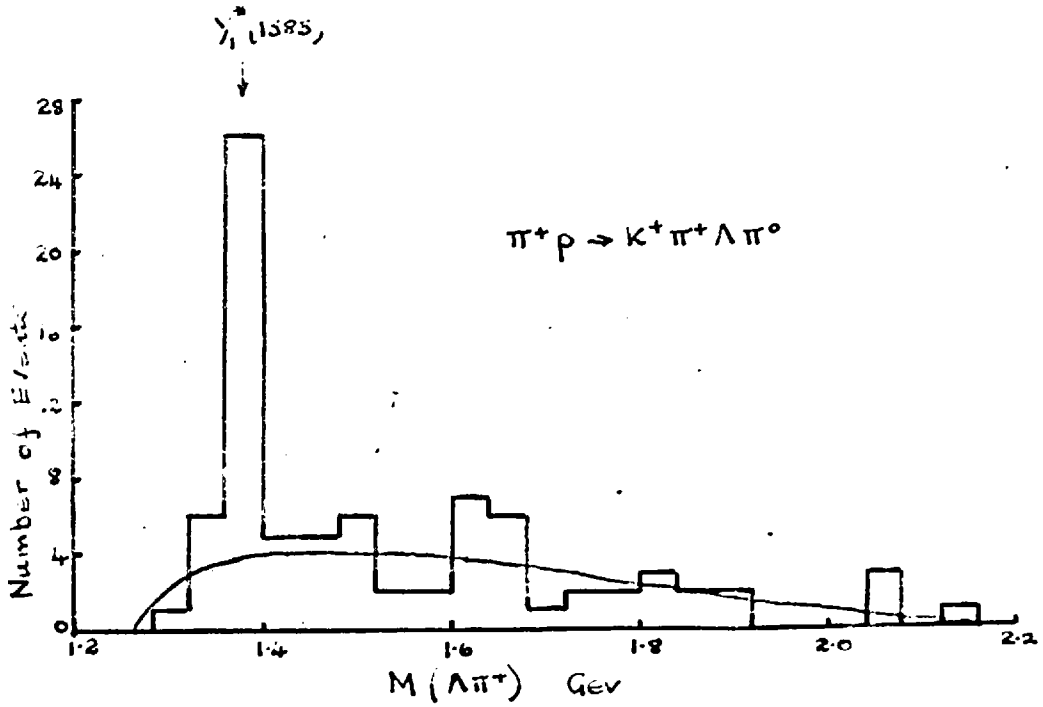


Fig. 6.1

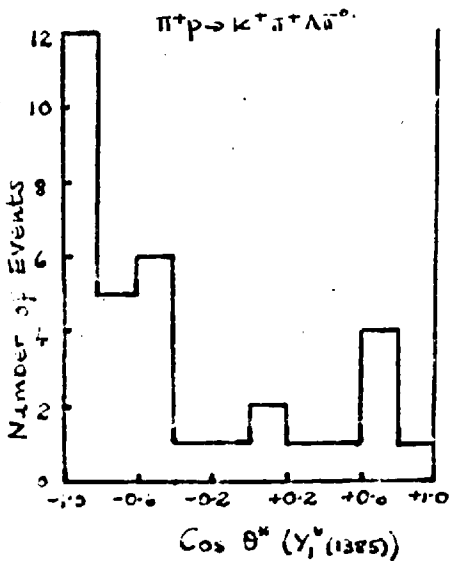


Fig 6.2

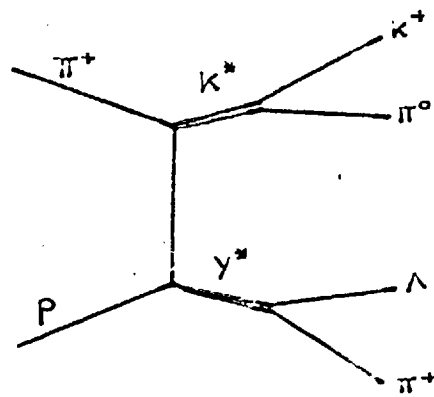


Fig 6.3

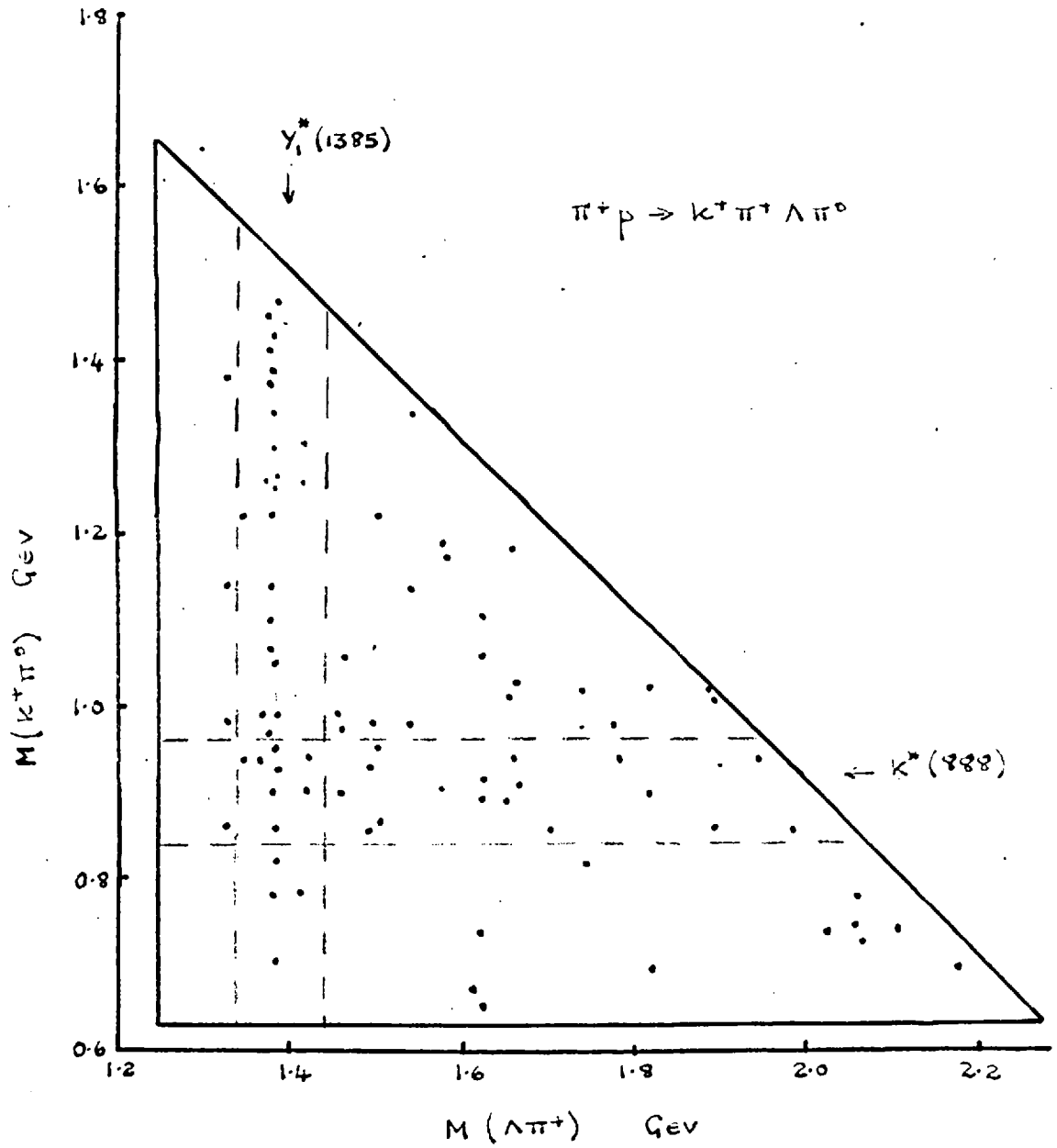


Fig 6.4

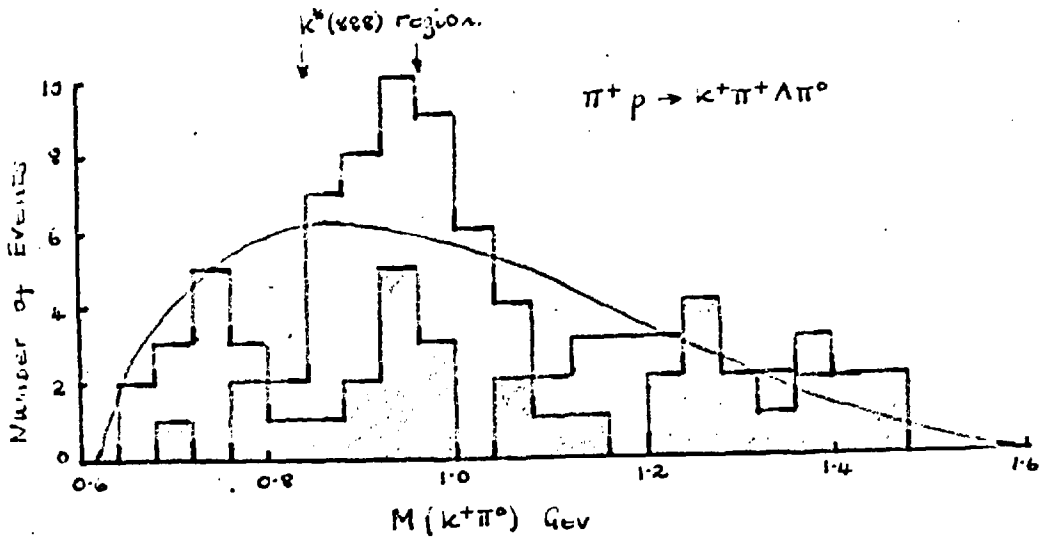


Fig 6.5

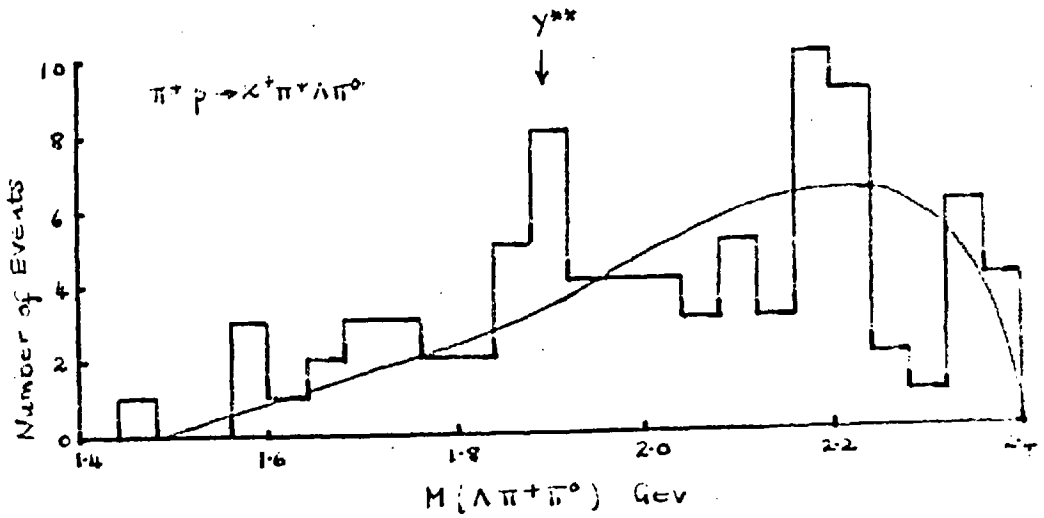


Fig 6.6

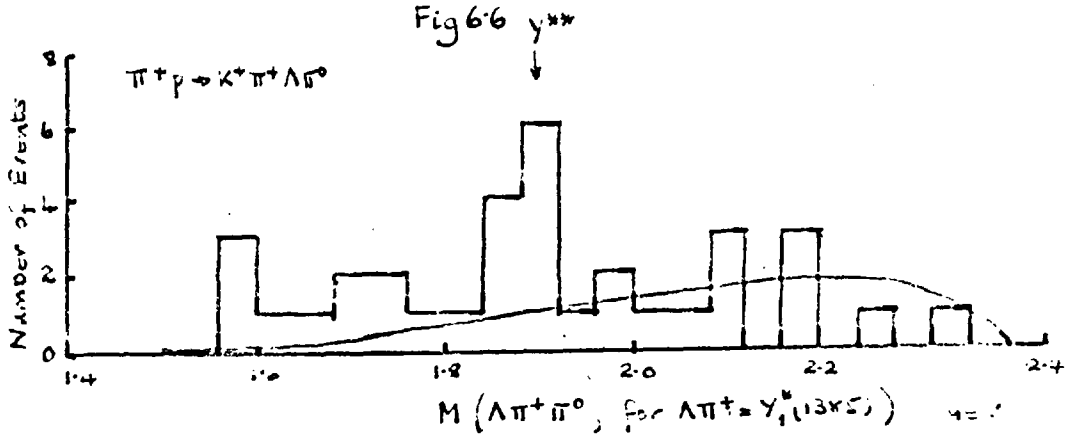


Fig 6.7

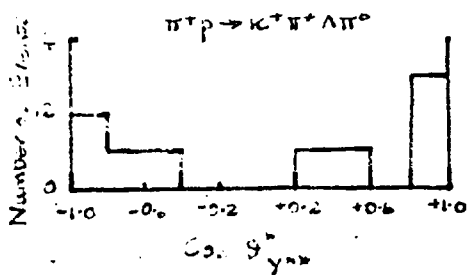


Fig 6-8

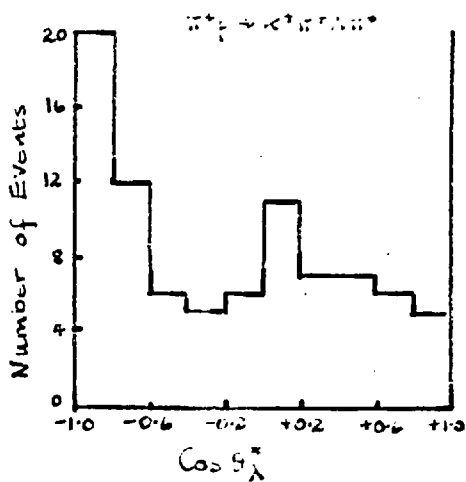


Fig 6-9

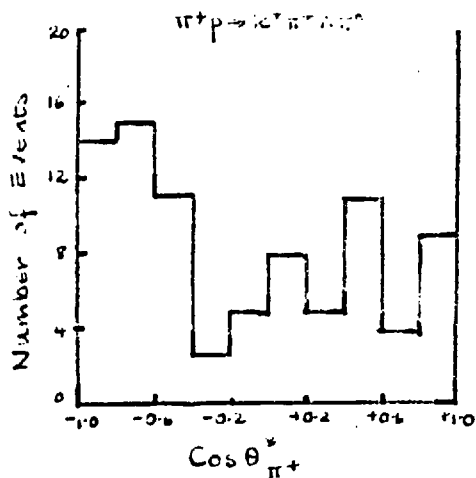


Fig 6-11

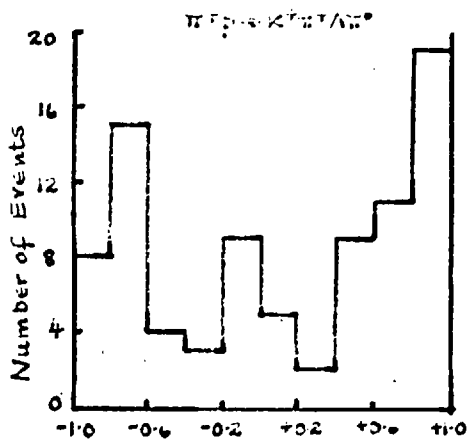


Fig 6-10

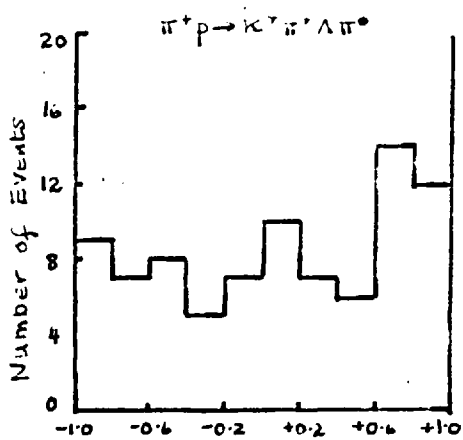


Fig 6-12

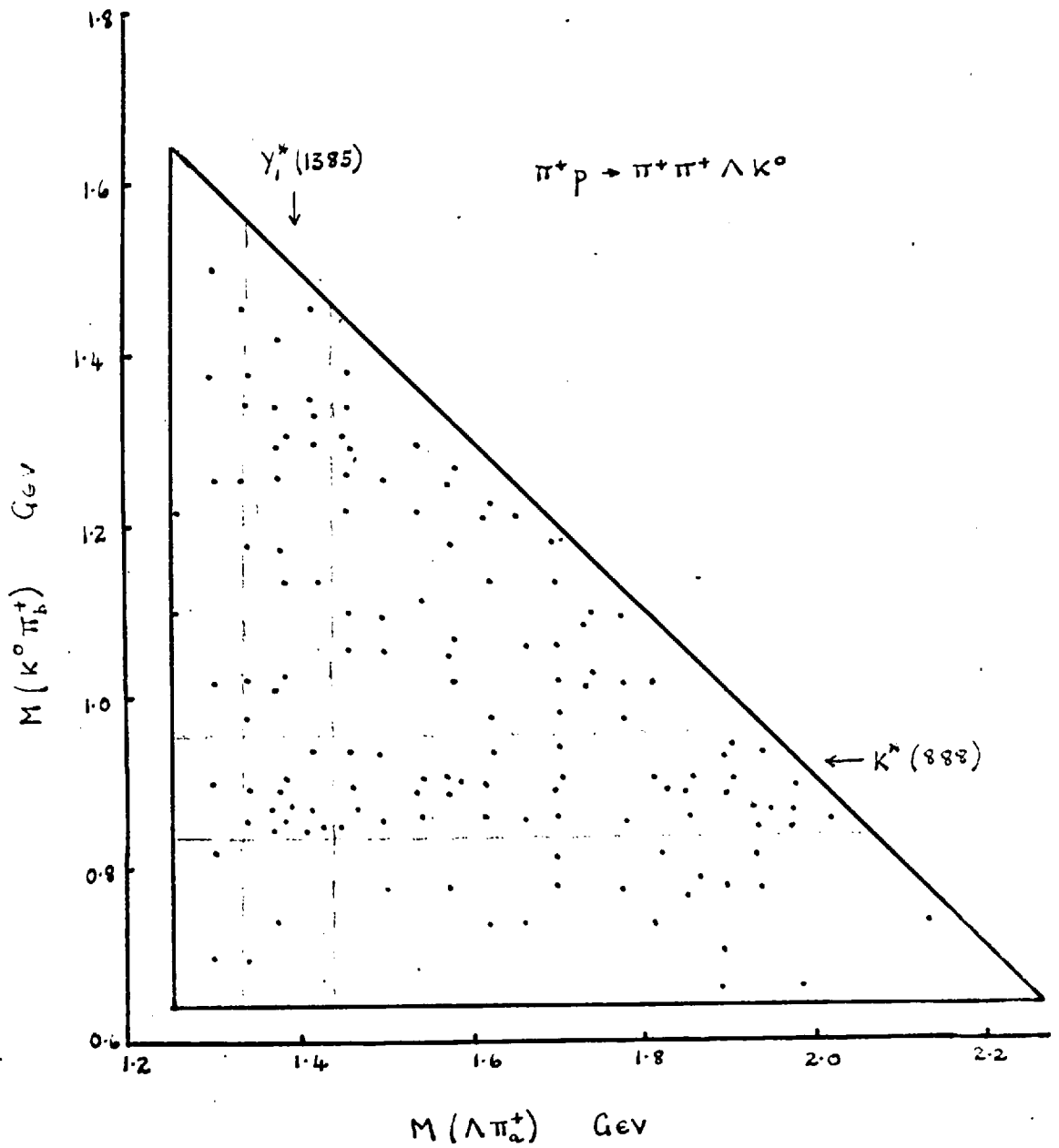


Fig 6.13

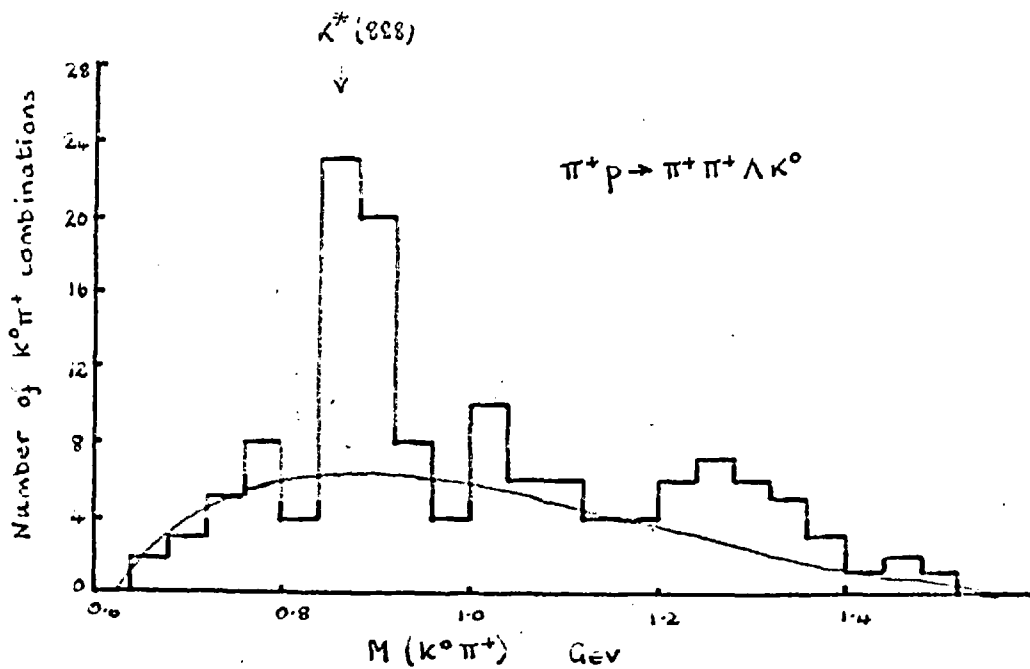


Fig 6-14

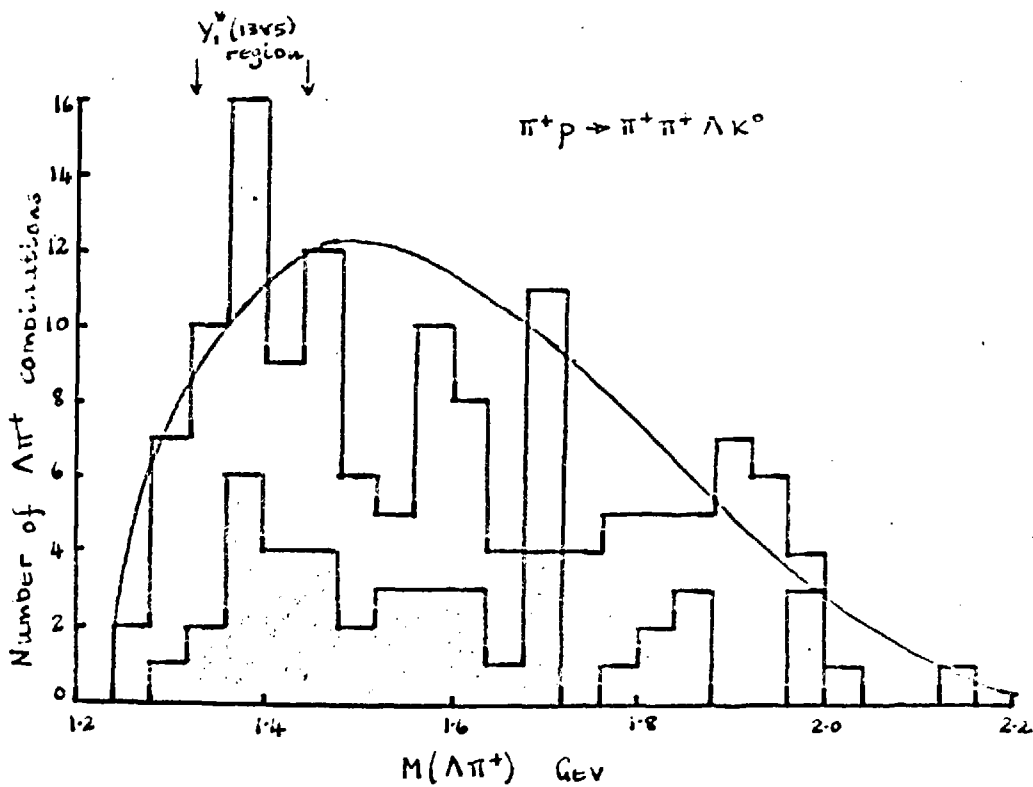


Fig 6-15

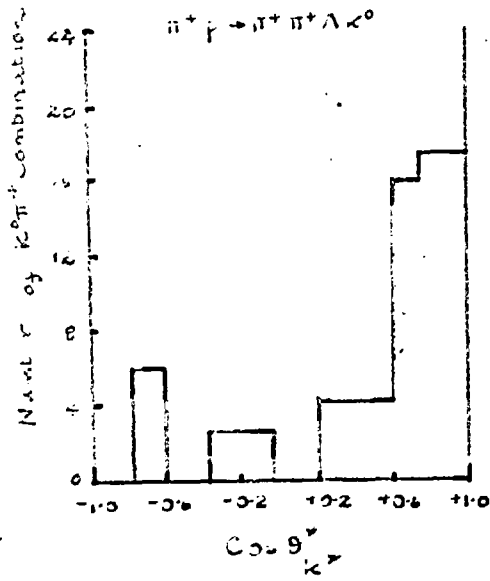


Fig 6.16

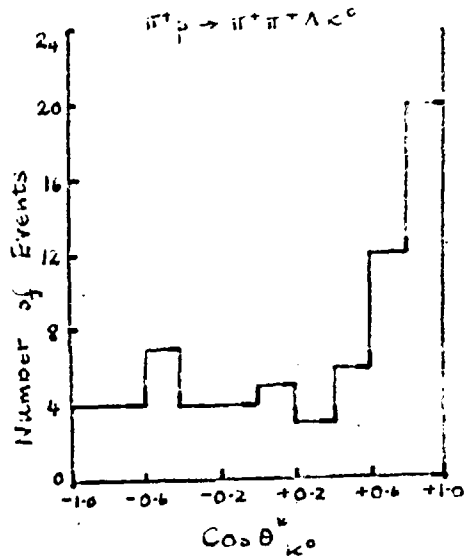


Fig 6.18

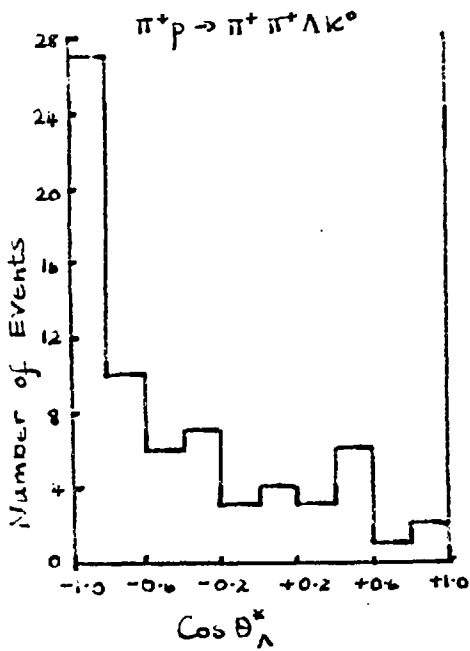


Fig 6.17

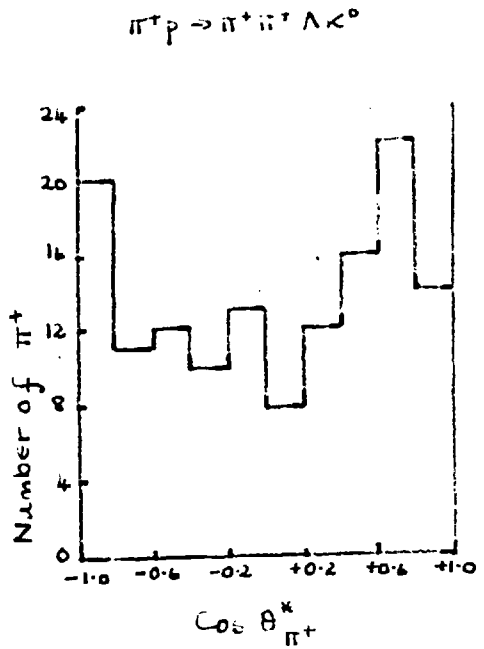


Fig 6.19

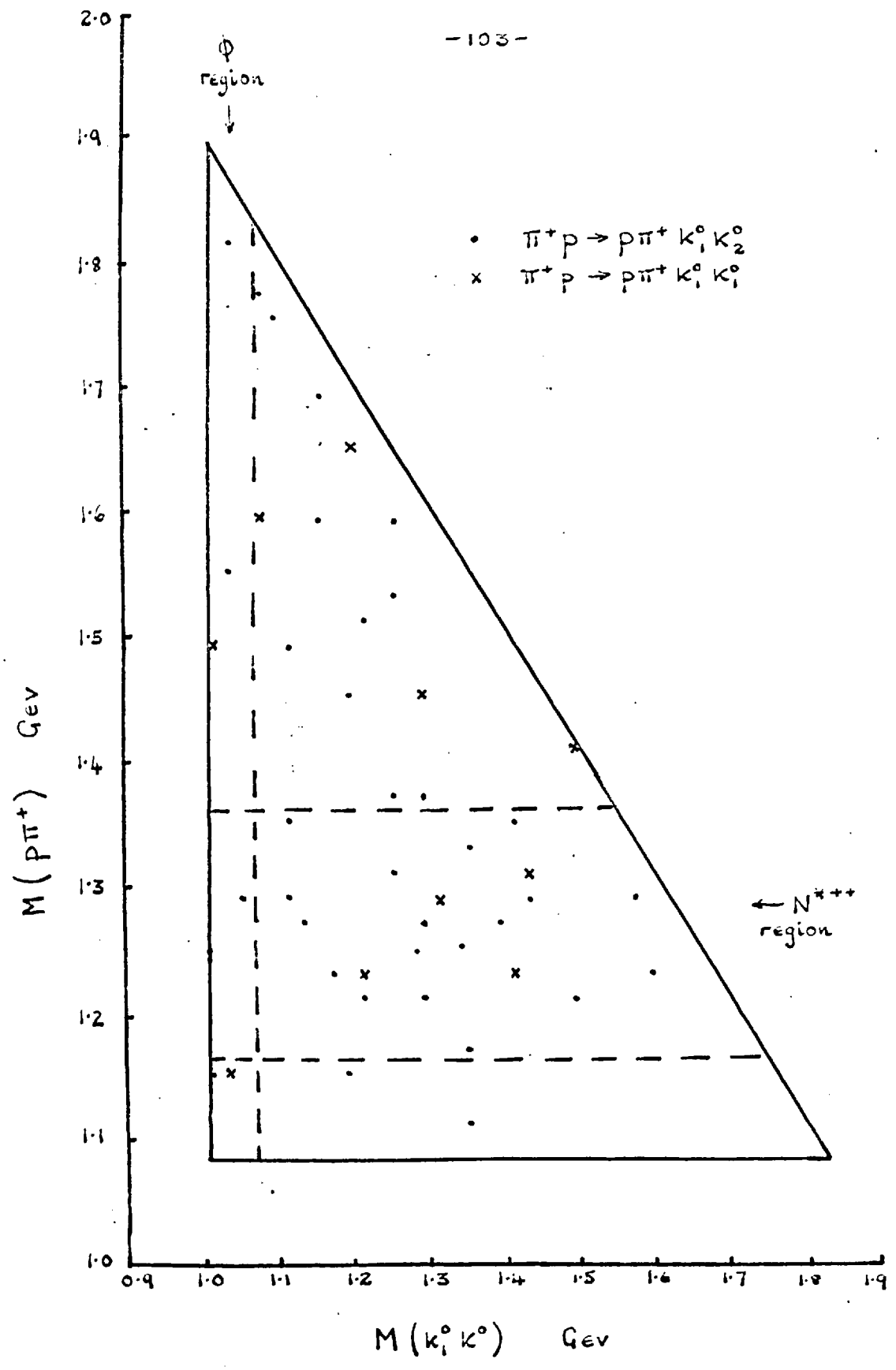


Fig 6.20

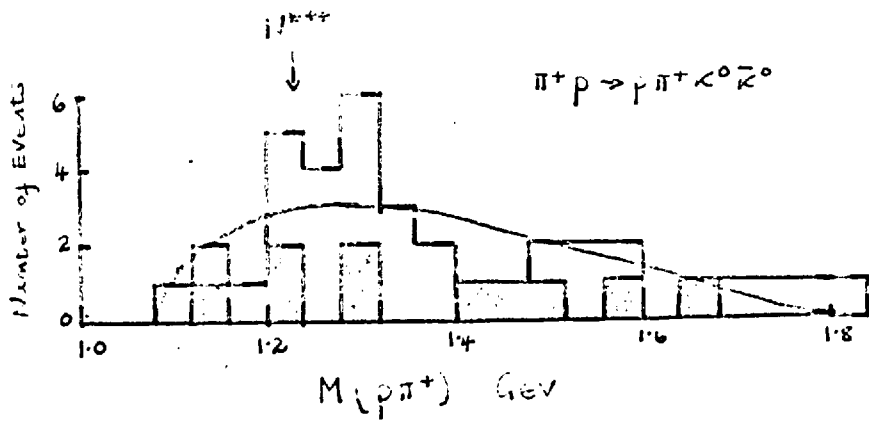


Fig 6.21

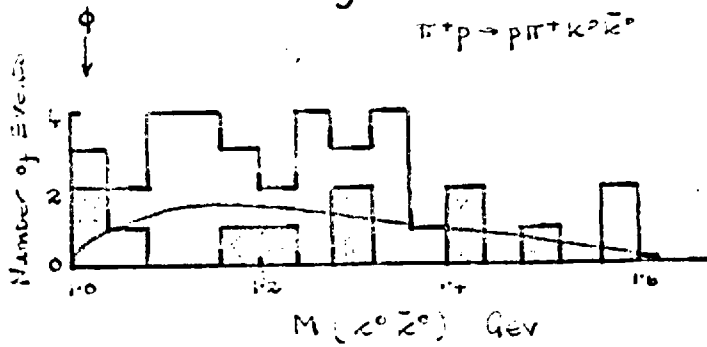


Fig 6.22

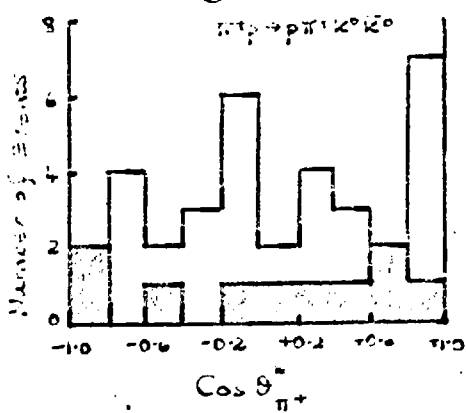


Fig 6.23

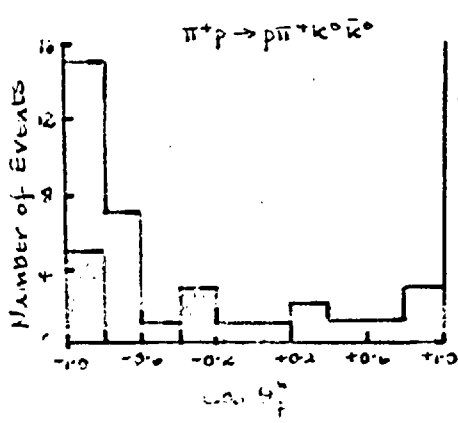


Fig 6.24

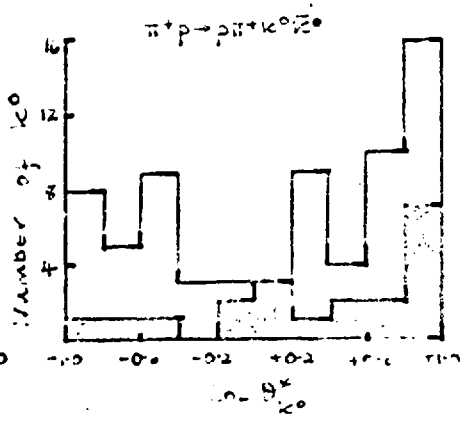


Fig 6.25

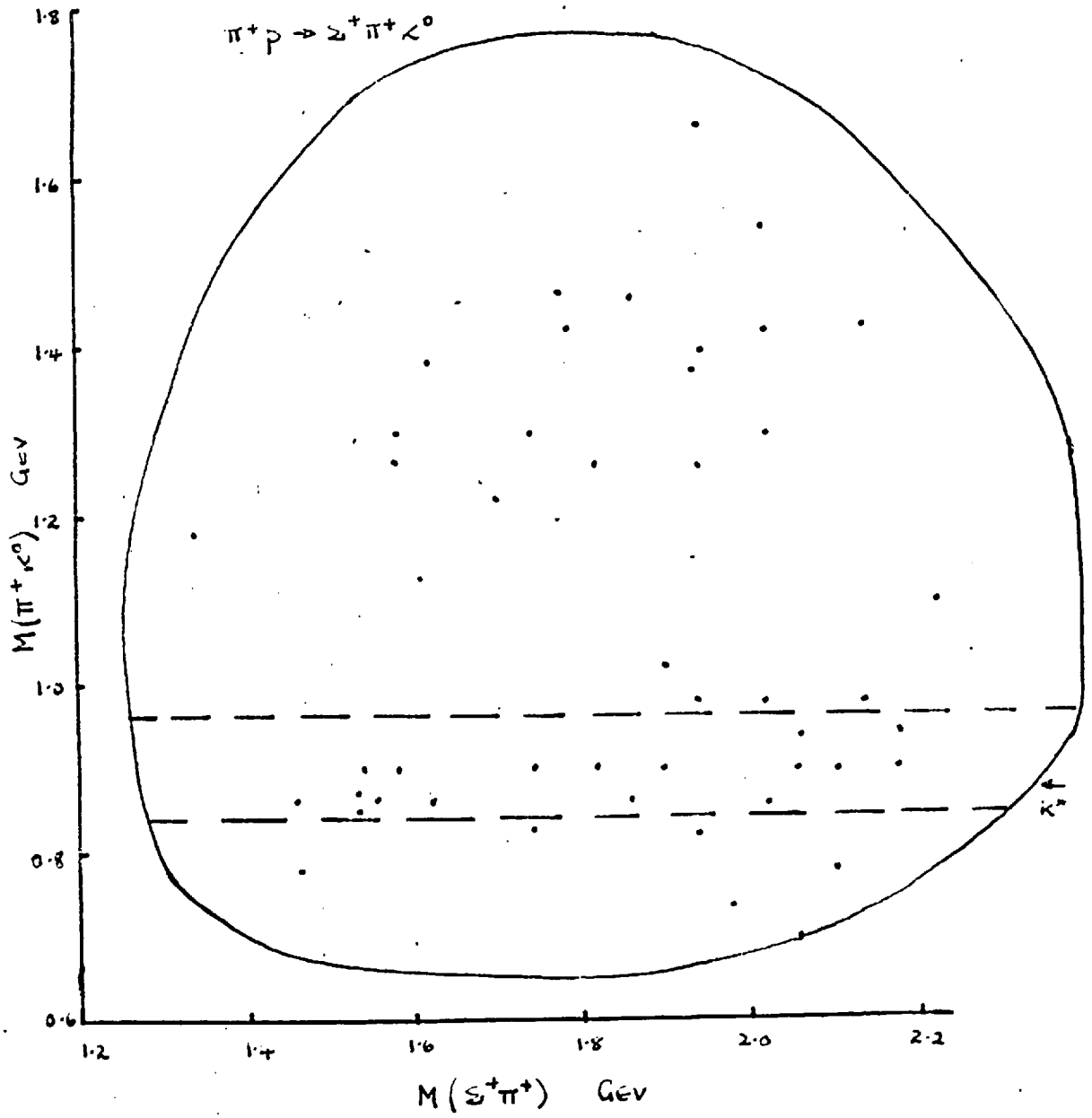


Fig 6.26

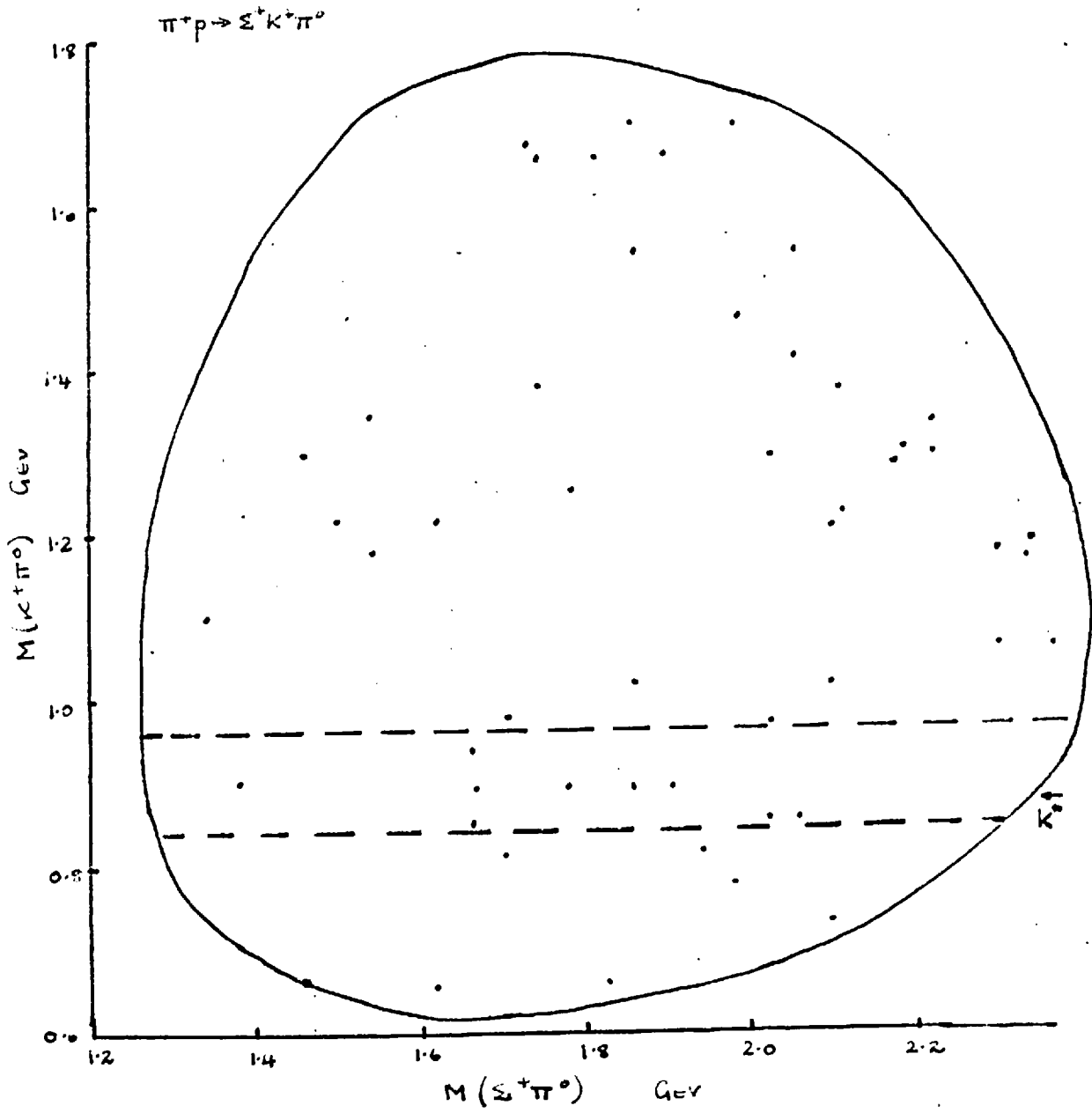


Fig 6.27

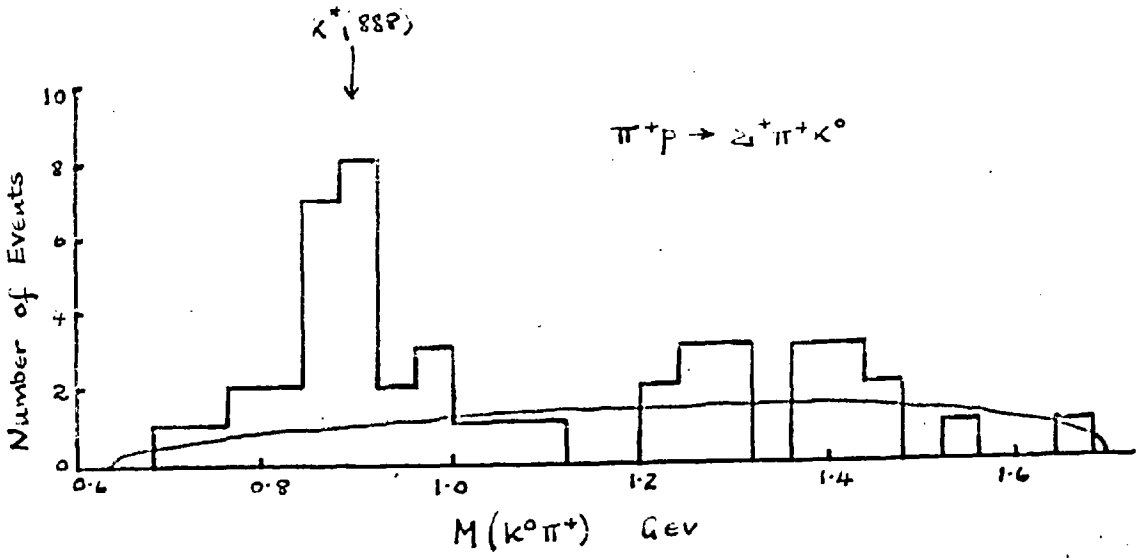


Fig 6.28

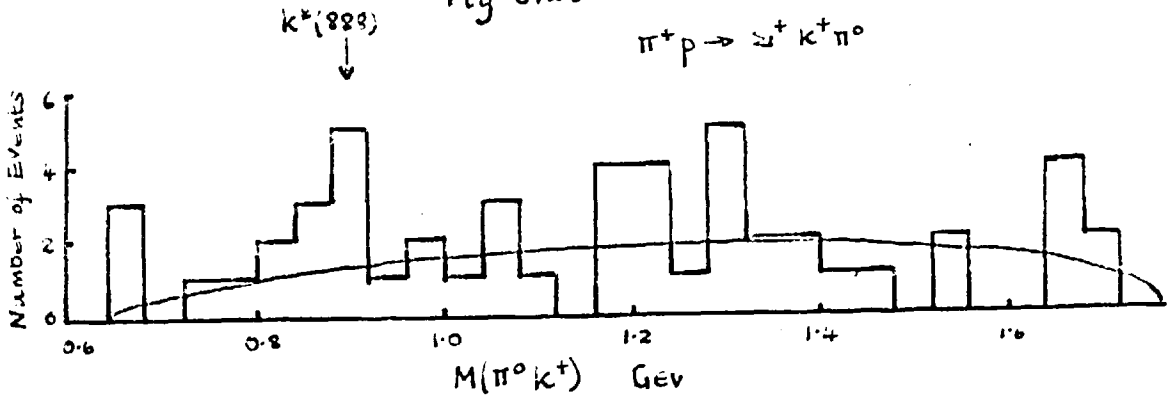


Fig 6.29

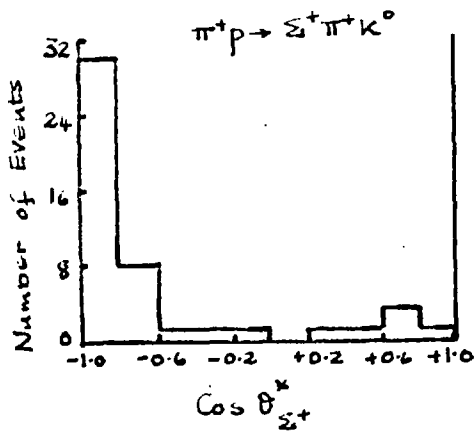


Fig 6.30

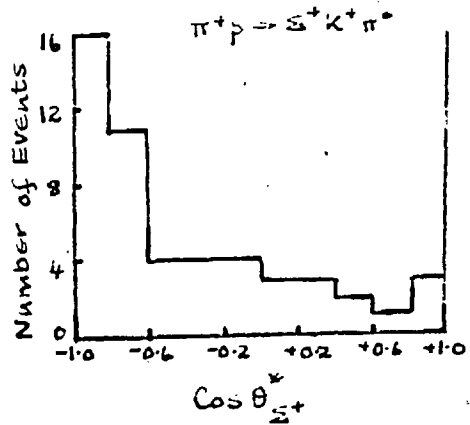


Fig 6.31

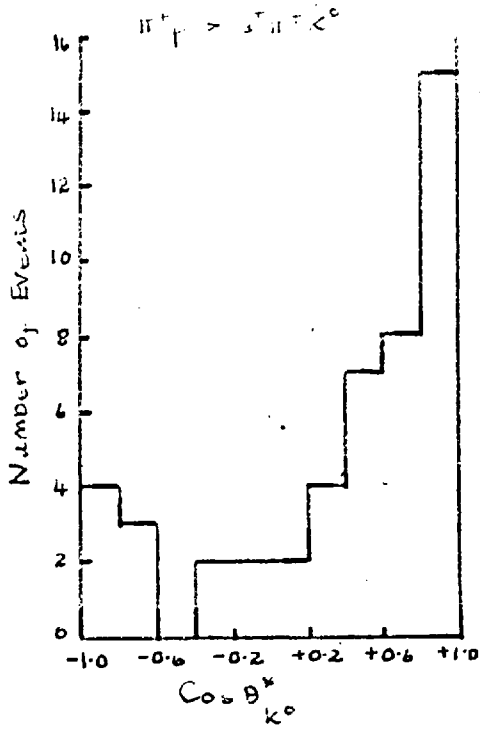


Fig 6.32

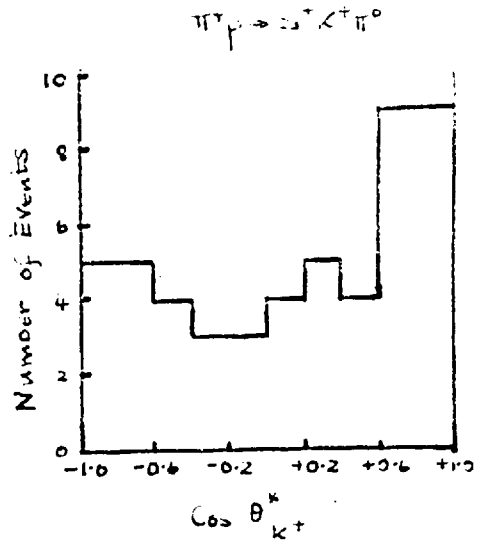


Fig 6.34

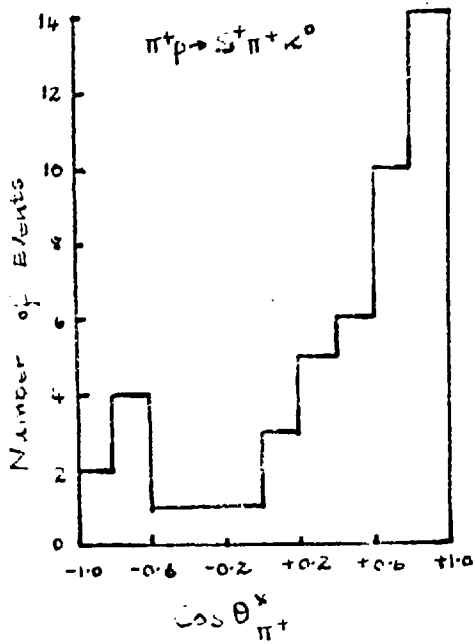


Fig 6.33

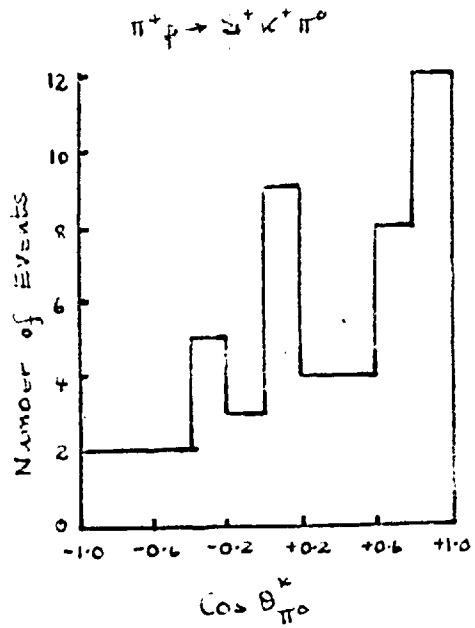


Fig 6.35

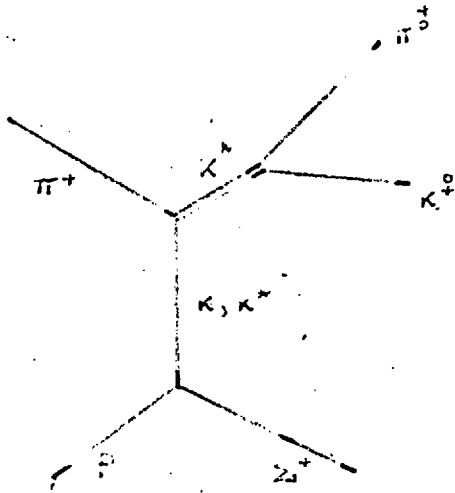


Fig 6-36

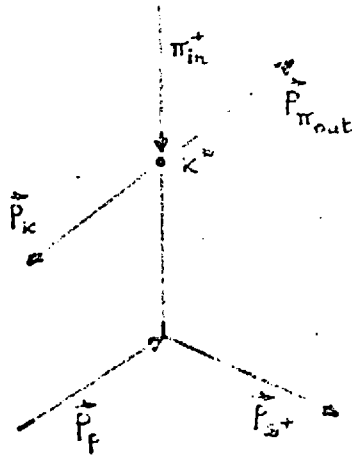


Fig 6-37

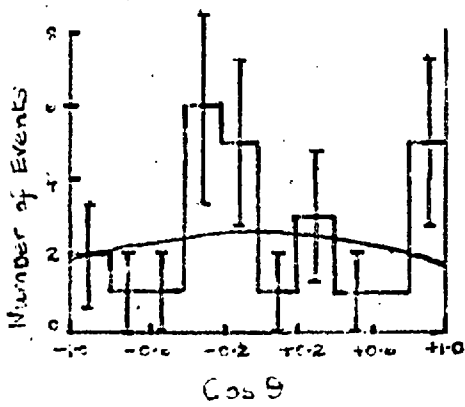
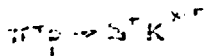


Fig 6-38

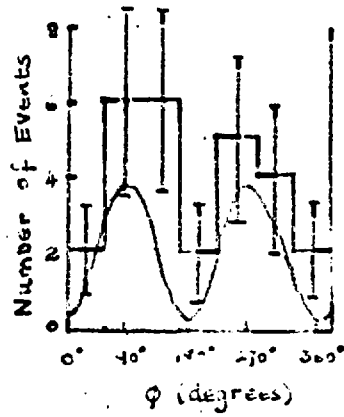
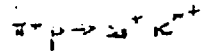


Fig 6-39

CHAPTER 7

EXCHANGE MECHANISMS

7.1 Introduction

The peripheral model was first suggested by Goebel <sup>(41)</sup> and Chew and Low <sup>(10)</sup> to study the scattering of unstable particles (e.g.  $\pi$ - $\pi$  scattering); to do this, the one-particle exchange contribution had to be isolated by extrapolation of the production data from the physical region of  $\Delta^2$  (the four momentum transfer) to the point in the unphysical region  $\Delta^2 = -m_{ex}^2$ . This extrapolation was difficult to do experimentally, but the implication that this pole influenced the physical region for small values of  $\Delta^2$  was the basis for the one-pion-exchange models proposed by Drell <sup>(42)</sup>, Salzman and Salzman <sup>(43)</sup> and Ferrari and Selleri <sup>(44)</sup>.

In an attempt to account for the rapid decrease in production ~~cross~~-section with increasing  $\Delta^2$ , Ferrari and Selleri introduced empirical form factors which accounted for all the disagreement between the peripheral model and the experimental data; while this was comparatively successful for one-pion exchange, for vector meson exchange these form factors had to have such a strong  $\Delta^2$  dependence that the peripheral nature of the interaction was lost. Recently Gottfried and Jackson <sup>(45)</sup> have applied the absorptive model <sup>(46)</sup> to explain the differences

between theory and experiment without using such form factors.

## 7.2 Gottfried and Jackson Analysis (45, 47-52)

This analysis has been developed to determine the exchange mechanisms responsible for quasi-two body interactions at high energies. As the analysis is carried out in terms of decay angular correlations, one of the resonances produced must decay through a parity conserving process (e.g. the strong interaction).

The choice of the cartesian coordinate reference system is arbitrary, but for peripheral interactions there is one which emphasises the exchanged system. For this, the z-axis is chosen along the direction of the incident pion as seen from the unstable particle's rest system. The y-axis is chosen along the direction of the normal to the production plane, so that the x-axis lies in the production plane.

The decay angles  $\theta$  and  $\phi$  are then defined with respect to this system as shown in Figure 7.22. It can easily be shown (49) that  $\phi$  is equivalent to the Treiman-Yang angle (53) and it is generally defined so that  $\phi = 0$  in the production plane.

It is possible to describe the spin population of a resonance by a hermitean density matrix  $\rho_{mm'}$ , where  $m$  and  $m'$  are magnetic quantum numbers relative to the specified z-axis.

Parity conservation in the production process reduces the

number of independent elements of this matrix and using the Trace condition that  $\text{Tr } \rho = 1$  enables the matrix to be defined as follows for a resonance with spin  $J = 1$ .

$$\rho(J = 1) = \begin{bmatrix} \rho_{11} & \rho_{10} & \rho_{1,-1} \\ \rho_{10}^* & \rho_{00} & \rho_{10}^* \\ \rho_{1,-1} & -\rho_{10} & \rho_{11} \end{bmatrix}$$

where  $\rho_{00} = 1 - 2\rho_{11}$  and  $\rho_{11} = \rho_{1,-1}$  are real.

The predicted angular distributions in terms of  $\theta, \phi$  and  $\rho_{mm}$  for a spin one particle decaying to give two spinless bosons is then (47)

$$W(\theta, \phi) = \frac{3}{4\pi} (\rho_{00} \cos^2\theta + \rho_{11} \sin^2\theta - \rho_{1,-1} \sin^2\theta \cos^2\phi - \sqrt{2} \text{Re } \rho_{10} \sin 2\theta \cos \phi) \dots (1)$$

This expression is directly proportional to  $\frac{d\sigma}{d\phi d(\cos\theta)}$

so that if it is integrated over  $\phi$  ( $0 \rightarrow 2\pi$ ) the following result is obtained

$$\frac{d\sigma}{d(\cos\theta)} \propto (1 - \rho_{00}) + 3\rho_{00} \cos^2\theta \dots (2)$$

while integration over  $\cos\theta$  ( $+1 \rightarrow -1$ ) gives

$$\frac{d\sigma}{d\phi} \propto (1 + 2\rho_{1,-1}) - 4\rho_{1,-1} \cos^2\phi \dots (3)$$

To determine  $\text{Re } \rho_{10}$ , the expectation value of  $\langle \sin 2\theta \cos \phi \rangle$  is calculated from

$$\langle \sin 2\theta \cos \phi \rangle = \int_{0+1}^{2\pi-1} \int_{\phi \cos\theta} W(\theta, \phi) \frac{\sin 2\theta \cos \phi d\phi d(\cos\theta)}{W(\theta, \phi) d(\cos\theta) d\phi}$$

which gives  $\text{Re } \rho_{10} = \frac{-5}{4\sqrt{2}} \langle \sin 2\theta \cos \phi \rangle$ . (54)

For Pseudoscalar (e.g.  $\pi, K$ ) meson exchange only  $\rho_{00}$  will be different from zero, but for vector (e.g.  $\rho, \omega, \phi, K^*$ ) meson exchange only  $\rho_{11}$  and  $\rho_{1,-1}$  are non-vanishing.

The expected values of the matrix elements are either zero or one unless absorptive effects are included when the matrix elements deviate from these values with increasing  $\Delta^2$ .

In a similar manner it is possible to describe a baryonic ( $J = \frac{3}{2}$ ) resonance which decays into a boson and a baryon with  $J = \frac{1}{2}$  by the following density matrix.

$$\rho = \begin{bmatrix} \rho_{33} & \rho_{31} & \rho_{3,-1} & \rho_{3,-3} \\ \rho_{31}^* & \rho_{11} & i\rho_{1,-1} & \rho_{3,-1}^* \\ \rho_{3,-1} & -i\rho_{1,-1} & \rho_{11} & \rho_{31}^* \\ -i\rho_{3,-3} & \rho_{31} & -\rho_{3,-1} & \rho_{33} \end{bmatrix}$$

where  $\rho_{33}, \rho_{3,-3}$  and  $\rho_{1,-1}$  are real and  $\rho_{11} = \frac{1}{2} - \rho_{33}$ .

The decay angular distribution is then given by (47)

$$W(\theta, \phi) \propto (\rho_{33} \sin^2 \theta + \rho_{11} (\frac{1}{3} + \cos^2 \theta) - \frac{2}{\sqrt{3}} \text{Re } \rho_{3,-1} \sin^2 \theta \cos 2\phi - \frac{2}{\sqrt{3}} \text{Re } \rho_{31} \sin 2\theta \cos \phi)$$

this expression after integration over  $\phi$  and  $\cos \theta$  respectively, with the same limits as before, gives

$$\frac{d\sigma}{d(\cos \theta)} \propto 3\rho_{33} \sin^2 \theta + \rho_{11} (1 + 3 \cos^2 \theta) \dots (4)$$

$$\frac{d\sigma}{d\phi} \propto \left(1 + \frac{4}{\sqrt{3}} \operatorname{Re} \rho_{3,-1}\right) - \frac{8}{\sqrt{3}} \operatorname{Re} \rho_{3,-1} \cos^2 \phi \dots (5)$$

and  $\operatorname{Re} \rho_{31}$  is determined from the expectation value

$\langle \sin 2\theta \cos \phi \rangle$  using

$$\operatorname{Re} \rho_{31} = -\frac{5\sqrt{3}}{8} \langle \sin 2\theta \cos \phi \rangle.$$

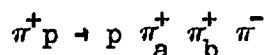
For pseudoscalar exchange  $\rho_{33}$ ,  $\operatorname{Re} \rho_{3,-1}$ ,  $\operatorname{Re} \rho_{31}$ , should be zero, so that  $\cos \theta$  will be proportional to  $(1 + 3 \cos^2 \theta)$

and  $\rho_{11} = 0.5$ .

For  $\rho$ -exchange, Sakurai and Stodolsky<sup>(55)</sup> predict values for these parameters using the  $\rho$ -photon analogy; the predicted values are  $\rho_{33} = \frac{3}{8}$ ,  $\operatorname{Re} \rho_{3,-1} = \frac{\sqrt{3}}{8}$ , and  $\operatorname{Re} \rho_{31} = 0$ .

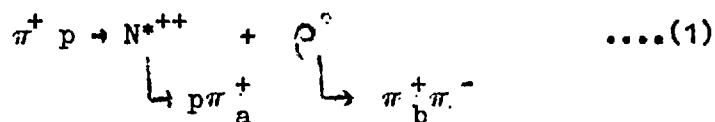
### 7.3 The reaction $\pi^+ p \rightarrow N^{*++} + \rho^0$ (8)

In 2072 events of the type



corresponding to a cross-section of 3.09 millibarns, strong  $N^{*++}$  and  $\rho^0$  production was observed (Figures 7.1 and 7.2.)

In Figure 7.4 the effective mass distribution for the  $\pi_b^+ \pi^-$  combination is shown for those events where the effective mass of the  $p\pi_a^+$  combination lay in the  $N^{*++}$  region which was defined to be 1.12 - 1.32 Gev. From this it was estimated that 20% of the events of this type proceeded by the reaction.



The cross-section for this quasi-two body process was 0.6 millibarns  $\pm$  30%. This error was sufficient to account for the effects of the large widths of these resonances.

The scatter diagram in Figure 7.3 for  $m(p\pi_a^+)$  against  $M(\pi_b^+\pi^-)$  is only for events for which  $\Delta^2(p/p\pi_a^+) < 0.3 \text{ Gev}^2$ . This shows that reaction (1) is produced at low four momentum transfer and can be described by the peripheral diagram in Figure 7.7. If both  $p\pi_a^+$  combinations satisfied this criterion only the one with the lowest value of  $\Delta^2$  was used.

The projections from this plot are shown in Figures 7.8 and 7.9. In Figure 7.8 the effective mass distribution for  $p\pi_a^+$  is shown for the  $\pi_b^+\pi^-$  effective mass lying in the  $\rho^0$  region (0.66 - 0.86 Gev). Figure 7.9 shows the  $\pi_b^+\pi^-$  effective mass distribution for the  $p\pi_a^+$  effective mass lying in the  $N^{*++}$  region. The background is negligible so that these events (423) will be used in the analysis of the decay angular distributions.

The vectors which are required to define the decay angular distributions for  $\rho^0 \rightarrow \pi_b^+\pi^-$  are shown in Figure 7.5; all these vectors are determined in the  $\rho^0$  centre of mass.

Then  $\text{Cos}\theta$  and  $\text{Cos}\phi$  are defined by the expressions:

$$\text{Cos}\theta = \frac{\vec{p}_{\pi_{in}^+} \cdot \vec{p}_{\pi_b^+}}{|\vec{p}_{\pi_{in}^+}| |\vec{p}_{\pi_b^+}|} \quad \text{Cos}\phi = \frac{(\vec{p}_{\pi_{in}^+} \times \vec{p}_{p_{in}^+}) \cdot (\vec{p}_{p_{in}^+} \times \vec{p}_{\pi_b^+})}{|\vec{p}_{\pi_{in}^+} \times \vec{p}_{p_{in}^+}| |\vec{p}_{p_{in}^+} \times \vec{p}_{\pi_b^+}|}$$

The distribution for  $\cos \theta$  and  $\phi$  are given in Figures 7.10 and 7.11 respectively with  $\phi = 0$  in the production plane.

The asymmetric decay of the  $\rho^0$  with respect to the incoming pion (i.e. in  $\cos \theta$ ) is well known <sup>(56)</sup> and does not prevent the determination of  $\rho_{00}$  provided that the s-wave ( $I = 0$ ) amplitude which causes the interference is assumed to be small; also on fitting the symmetric theoretical curve to the experimental distribution, the contribution due to the interference term is cancelled out.

The curves in Figures 7.10 and 7.11 show the results of least squares fitting of equation (2) and (3) respectively to the experimental data. From these and the mean value of  $\langle \sin 2\theta \cos \phi \rangle$ , the following values for the matrix elements were obtained for  $\Delta^2 (p/p_{\pi_a^+}) < 0.3 \text{ Gev}^2$ :

$$\rho_{00} = 0.77 \pm 0.04; \quad \rho_{1-1} = -0.044 \pm 0.035; \quad \text{Re } \rho_{10} = -0.062 \pm 0.025$$

These values are consistent with pure  $\pi$ - exchange if absorptive effects are taken into consideration. (This will be discussed in Section 7.5).

In Figure 7.6 the vectors which define the decay angles for  $N^{*++} \rightarrow p \pi_a^+$  are given; all the vectors are determined in the  $N^{*++}$  rest frame.

$\cos \theta$  and  $\cos \phi$  are then defined by

$$\cos \theta = \frac{\vec{p}_{\pi_{in}} \cdot \vec{p}_p}{|\vec{p}_{\pi_{in}} \cdot \vec{p}_p|} \quad \cos \phi = \frac{(\vec{p}_{\pi_{in}} \times \vec{p}_{\pi_{in}^+}) \cdot (\vec{p}_{\pi_{in}^+} \times \vec{p}_p)}{|\vec{p}_{\pi_{in}} \times \vec{p}_{\pi_{in}^+}| |\vec{p}_{\pi_{in}^+} \times \vec{p}_p|}$$

The experimental distributions for  $\text{Cos}\theta$  and  $\phi$  are shown in Figures 7.12 and 7.13, with  $\phi = 0$  in the production plane. A slight asymmetry is evident in  $\text{Cos}\theta$ , but this has not prevented the experimental data being fitted by the theoretical expressions. The curves shown in these two pictures were obtained from least squares fitting of equations (4) and (5) respectively to the experimental data; the following values for the matrix elements were obtained:

$$\rho_{33} = 0.077 \pm 0.028; \quad \text{Re} \rho_{3-1} = 0.011 \pm 0.03 \quad \text{Re} \rho_{31} = -0.013 \pm 0.028$$

These values confirm that this reaction proceeds by pure  $\pi^-$  exchange.

It has been suggested by Goldhaber et al. (57) working at an incident  $\pi^+$  momentum of 3.15 Gev/c that there were strong correlations between the decay angles of the  $\rho^0$  and  $N^{*++}$ . This is not possible if this reaction proceeds entirely by  $\pi^-$  exchange as there is then no means of transmitting angular information between the vertices. Goldhaber explained the effect in his data by concluding that it was not possible to isolate the pure one pion exchange process.

In the present experiment these possible correlations were examined by making a scatter diagram of  $\text{Cos} \theta_{\pi_b}^+$  from the decay of the  $\rho^0$  against  $\text{Cos} \theta_p$  for the  $N^{*++}$ . Figures 7.14 and 7.15 and

7.16 show the normalised projected distributions for  $\text{Cos } \theta_{\pi_b^+}$  for various regions of  $\text{Cos } \theta_p$ ; these regions were chosen to be the same as those given by Goldhaber. Similar distributions for  $\text{Cos } \theta_p$  for intervals of  $\text{Cos } \theta_{\pi_b^+}$  are given in Figures 7.17, 7.18 and 7.19.

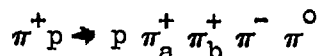
If there were no correlations between these angles then the distribution of  $\text{Cos } \theta_{\pi_b^+}$  should be independent of the interval chosen for  $\text{Cos } \theta_p$ , and similarly the distribution of  $\text{Cos } \theta_p$  should have the same shape regardless of the interval of  $\text{Cos } \theta_{\pi_b^+}$ .

From these distributions it can be seen that  $\text{Cos } \theta_{\pi_b^+}$  does not depend on  $\text{Cos } \theta_p$  as Figures 7.14, 7.15 and 7.16 are similar. This, however, does not seem to be true for  $\text{Cos } \theta_p$ , where the distribution in Figure 7.18 ( $-0.45 \leq \text{Cos } \theta_{\pi_b^+} \leq 0.4$ ) is isotropic while the others have approximately  $\text{Cos}^2 \theta_p$  behaviour.

This correlation is much weaker than that observed by Goldhaber and it can probably be explained by the effect of the background or absorptive effects.

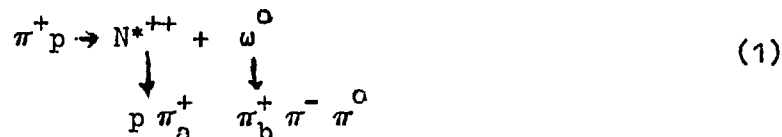
7.4 The Reaction  $\pi^+ p \rightarrow N^{*++} + \omega^0$  (8)

Strong  $N^{*++}$  and  $\omega^0$  production was observed in 2290 events of the type



produced with a cross-section of 3.43 millibarns.

Figures 7.20 and 7.21 show the projections for the effective masses of the  $p \pi^+$  and  $\pi^+ \pi^- \omega^0$  combinations from the scatter diagram Figure 8.1. It can be seen that about 10% of the events proceed by the reaction



corresponding to a cross-section of  $3.35 \text{ mb} \pm 30\%$ .

In order to get a pure sample of events of this reaction, only those events for which  $\Delta^2 (p/p \pi_a^+) \leq 0.6 \text{ Gev}^2$  were selected. This implied that the reaction was peripheral in nature and could be described by the diagram given in Figure 7.23 where the identity of the exchanged particle had to be established.

Figure 7.26 shows the scatter diagram for events satisfying this criterion and nearly all the background has been removed.

The projection for the effective mass of the  $\pi_a^+ \pi^- \pi^0$  combination for  $p \pi_a^+$  in the  $N^{*++}$  region is shown in Figure 7.27 and the similar projection for the  $p \pi_a^+$  effective mass for the

$\pi^+ \pi^- \pi^0$  effective mass lying in the  $\omega^0$  region (0.74 - 0.84 Gev) is shown in Figure 7.28. A pure sample of reaction (1) has been obtained in this way so these 240 events will be used in the analysis of the decay angular distributions.

The vectors required to define the decay angles of the  $\omega^0$  are shown in Figure 7.24, all of which are defined in the  $\omega^0$  rest system.

For the decay of a resonance into three similar particles  $\text{Cos}\theta$  has to be defined differently; as the  $\omega^0$  decays through a parity conserving process, it is valid to select the normal to the decay plane and define  $\theta$  as the angle between this plane and the incoming  $\pi^+$ , where all vectors are defined in the  $\omega^0$  centre of mass.

$\text{Cos}\theta$  and  $\text{Cos}\phi$  are defined by

$$\text{Cos}\theta = \frac{\vec{p}_{\pi^+} \cdot \hat{n}}{|\vec{p}_{\pi^+} \cdot \hat{n}|} \quad \text{Cos}\phi = \frac{(\vec{p}_{\pi^+} \times \vec{p}_{\pi^-}) \cdot (\vec{p}_{\pi^0} \times \hat{n})}{|\vec{p}_{\pi^+} \times \vec{p}_{\pi^-}| |\vec{p}_{\pi^0} \times \hat{n}|}$$

where

$$\hat{n} = \frac{\vec{p}_{\pi^0} \times \vec{p}_{\pi^-}}{|\vec{p}_{\pi^0} \times \vec{p}_{\pi^-}|}$$

and the experimental distributions for  $\text{Cos}\theta$  and  $\phi$  are given in Figures 7.29 and 7.30 respectively.

The curves represent the results obtained from the least squares fitting of the theoretical expressions to the experimental data; the theoretical expressions used were the same as those discussed in the previous section. The values of the matrix elements obtained were:

$$\rho_{00} = 0.47 \pm 0.05; \quad \rho_{1,-1} = 0.126 \pm 0.045; \quad \text{Re } \rho_{10} = -0.103 \pm 0.026.$$

Similarly in Figure 7.25 the vectors needed to determine  $\text{Cos } \theta$  and  $\text{Cos } \phi$  are shown; all are defined in the  $N^{*++}$  centre of mass.

$\text{Cos } \theta$  and  $\text{Cos } \phi$  are then defined by:

$$\text{Cos } \theta = \frac{\vec{p}_{p_{in}} \cdot \vec{p}_p}{|\vec{p}_{p_{in}} \cdot \vec{p}_p|} \quad \text{Cos } \phi = \frac{(\vec{p}_{p_{in}} \times \vec{p}_{\pi_{in}}) \cdot (\vec{p}_{\pi_{in}} \times \vec{p}_p)}{|\vec{p}_{p_{in}} \times \vec{p}_{\pi_{in}}| |\vec{p}_{\pi_{in}} \times \vec{p}_p|}$$

and the experimental distributions for  $\text{Cos } \theta$  and  $\phi$  are given in Figures 7.31 and 7.32, with  $\phi = 0$  in the production plane. The curves represent the least squares fit of the theoretical distributions to the data, and the values for the matrix elements obtained were:

$$\rho_{33} = 0.15 \pm 0.04; \quad \text{Re } \rho_{3-1} = 0.035 \pm 0.046; \quad \text{Re } \rho_{31} = -0.048 \pm 0.038.$$

These two sets of results for the  $\omega^0$  and  $N^{*++}$  decay are difficult to interpret, as they cannot easily be explained by a single exchange mechanism.

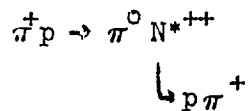
For this reaction, only certain particles can be exchanged. From considering G-parity conservation at the pion vertex in Figure 7.23, only particles with positive G-parity can be exchanged. This forbids  $\pi$ ,  $\eta$  or  $\omega^0$  exchange while allowing  $\rho$ -exchange.

If this reaction proceeded predominantly by  $\rho$ -exchange then the values expected for the  $\omega^0$  matrix elements are  $\rho_{00}$  and  $\text{Re } \rho_{10}$  almost equal to zero and  $\rho_{1-1}$  almost one; whereas for the  $N^{*++}$  vertex the matrix elements should have the following values for  $\rho$ -exchange (55):-

$$\rho_{33} = 0.38; \quad \text{Re } \rho_{3-1} = 0.22; \quad \text{Re } \rho_{31} = 0.$$

The experimental data does not agree with these expected values.

That these predicted values are correct for  $\rho$ -exchange has been confirmed in the analysis of the following reaction at 4 GeV/c (7):



The angular distributions showed that the data was consistent with a M1 transition at the  $N\rho N^*$  vertex using the Sakurai and Stodolsky theory (55). This reaction was then analysed using the Gottfried-Jackson analysis and  $\text{Cos } \theta'$  and  $\phi$  calculated for

the  $N^{*++}$  decay, from which values of the matrix elements were obtained consistent with those quoted above.

It is therefore concluded that the reaction  $\pi^+ p \rightarrow N^{*++} + \omega^0$  cannot be explained by  $\rho$ -exchange alone, unless absorptive effects drastically modify the results. The effect of absorption will be discussed in the next section.

### 7.5 The Effect of Absorption on the Peripheral Model

Although the peripheral model can generally explain the decay angular distributions in terms of one or two exchange mechanisms, it is unable to explain the four momentum transfer distributions.

These distributions are more strongly peaked towards low values of  $\Delta^2$  than those predicted by the unadorned peripheral model and generally have angular spreads that are mostly independent of the nature of the exchanged particle. The absorption model was introduced by Gottfried, Jackson and Svensson (45, 50-52) to try and explain these discrepancies.

Any quasi-two body process accounts for only a small fraction of all the open channels that contribute to the total inelastic cross-section; it is possible to consider this process in a similar way to elastic diffraction scattering ("shadow" scattering) which arises from the existence of a strongly absorbing region of finite extent. Intuitively it seems reasonable to expect

quasi-two body processes to occur at large impact parameters, while more complicated un-correlated final states are produced at large values of  $\Delta^2$  and so act as a large absorbing region. These many body channels would therefore reduce the contributions to the reaction amplitude from the low partial waves to below the values expected from the simple peripheral model while leaving the contributions due to the higher partial waves unchanged. This would result in lower values for the reaction cross-sections and modified angular distributions and decay correlations.

Jackson (51) and Svensson (52) have applied the absorption model to the reactions:



for the results obtained at 4 Gev/c incident pion momentum.

The suppression of the low partial waves was determined using a high energy form of the distorted wave Born approximation for potential scattering (45) with the spins of the particles explicitly included.

The four momentum transfer distributions, between the proton and the  $N^{*++}$ , for these two reactions are shown in Figures 7.33 and 7.34 respectively.

The experimental results are compared with theoretical curves

calculated assuming the absorption model. There is good agreement between the theory and experiment for reaction (1), but in reaction (2) there is marked disagreement. In this case, if a form factor is included which is only a slowly varying function of  $\Delta^2$ , the model can be made to agree with the experimental data.

The absorption model predicts that as  $\Delta^2$  increases, the values of the matrix elements should depart significantly from those predicted for the simple peripheral model. Therefore, the study of the experimental  $\Delta^2$  dependence of these matrix elements can determine whether the absorption model is to be preferred over the peripheral model with form factors which predicts matrix elements independent of  $\Delta^2$ .

Jackson (51) has calculated the variations for  $\rho_{mm}$  with  $\Delta^2$  for reaction (1). These theoretical curves are compared with the experimental values which are averaged over all  $\Delta^2$  and plotted at the average value of  $\Delta^2$  observed. (Figures 7.35 and 7.36). The agreement is extremely good for this reaction.

Svensson (52) has, in a similar manner, applied the absorption model to reaction (2), where the results are not as convincing. The comparisons between the theory and the experimental data are shown in Figures 7.37 and 7.38; the experimental points have been determined for different  $\Delta^2$  intervals.

It is obvious that the simple peripheral model (shown by the dotted lines) does not fit the experimental results, but it is debatable whether the absorption model (the solid lines) explains the results any better.

If it is thought that this reaction can be explained by  $\rho$ -exchange using the absorption model, then this is the first reaction in which the suppression of the low partial waves gives values for  $\rho_{mm}$ , very different from those predicted by the peripheral model.

It is concluded that the absorption model explains the results of reaction (1) very well, but that it cannot convincingly explain the data of reaction (2) in terms of  $\rho$ -exchange alone.

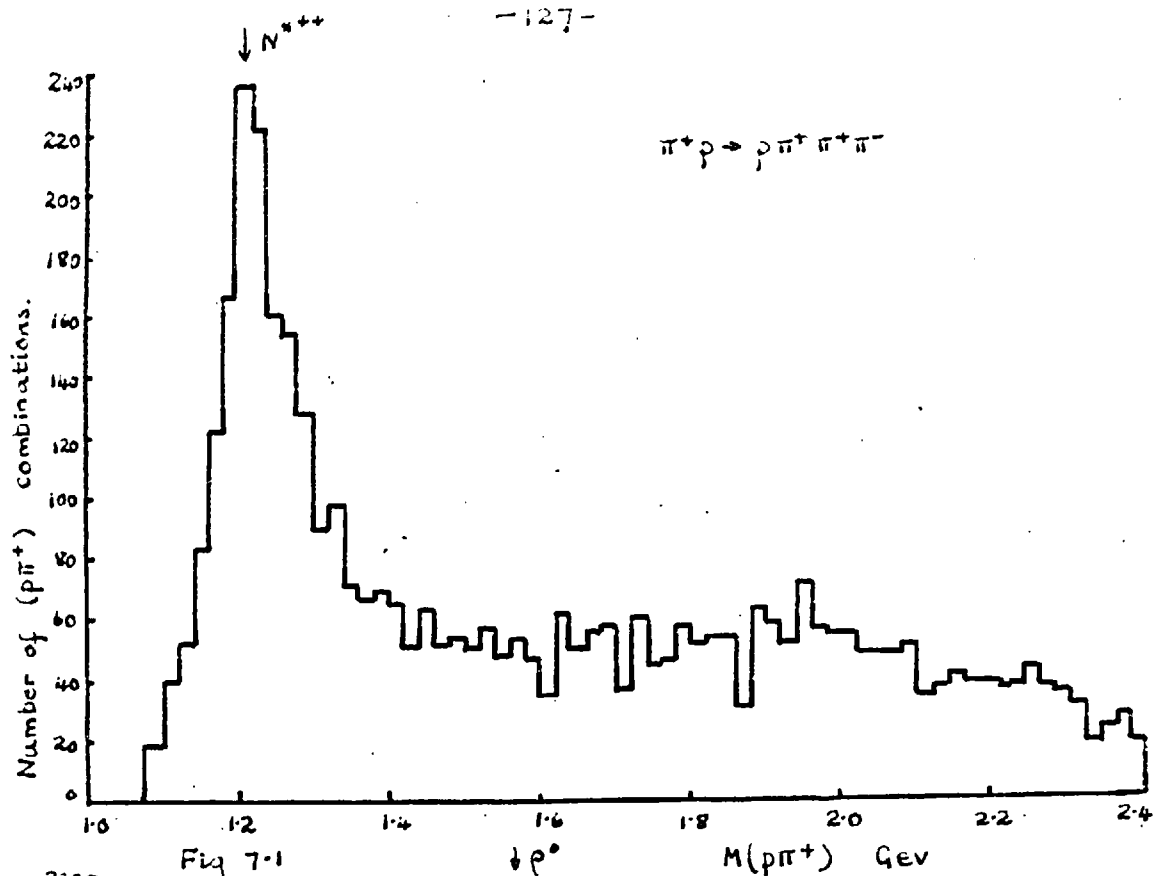


Fig 7-1

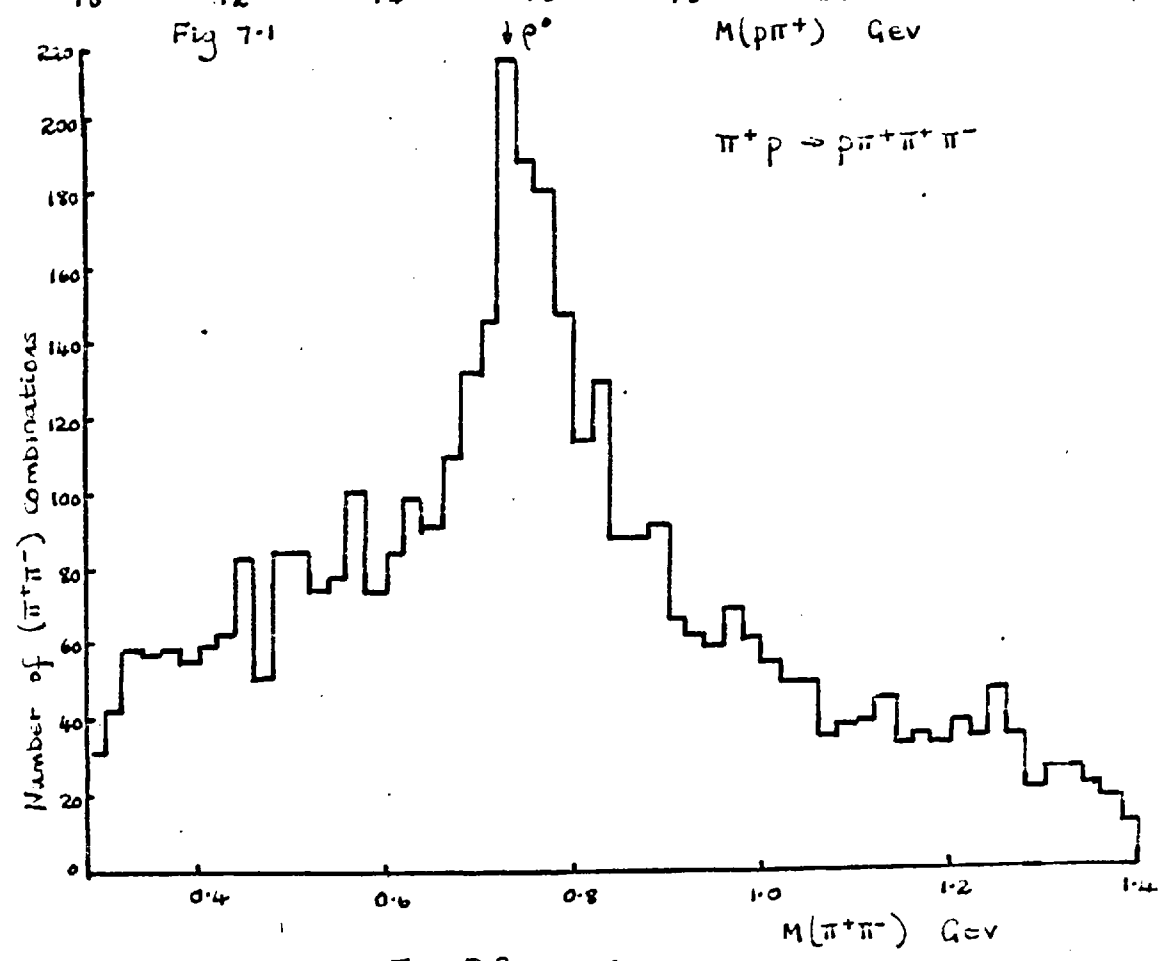
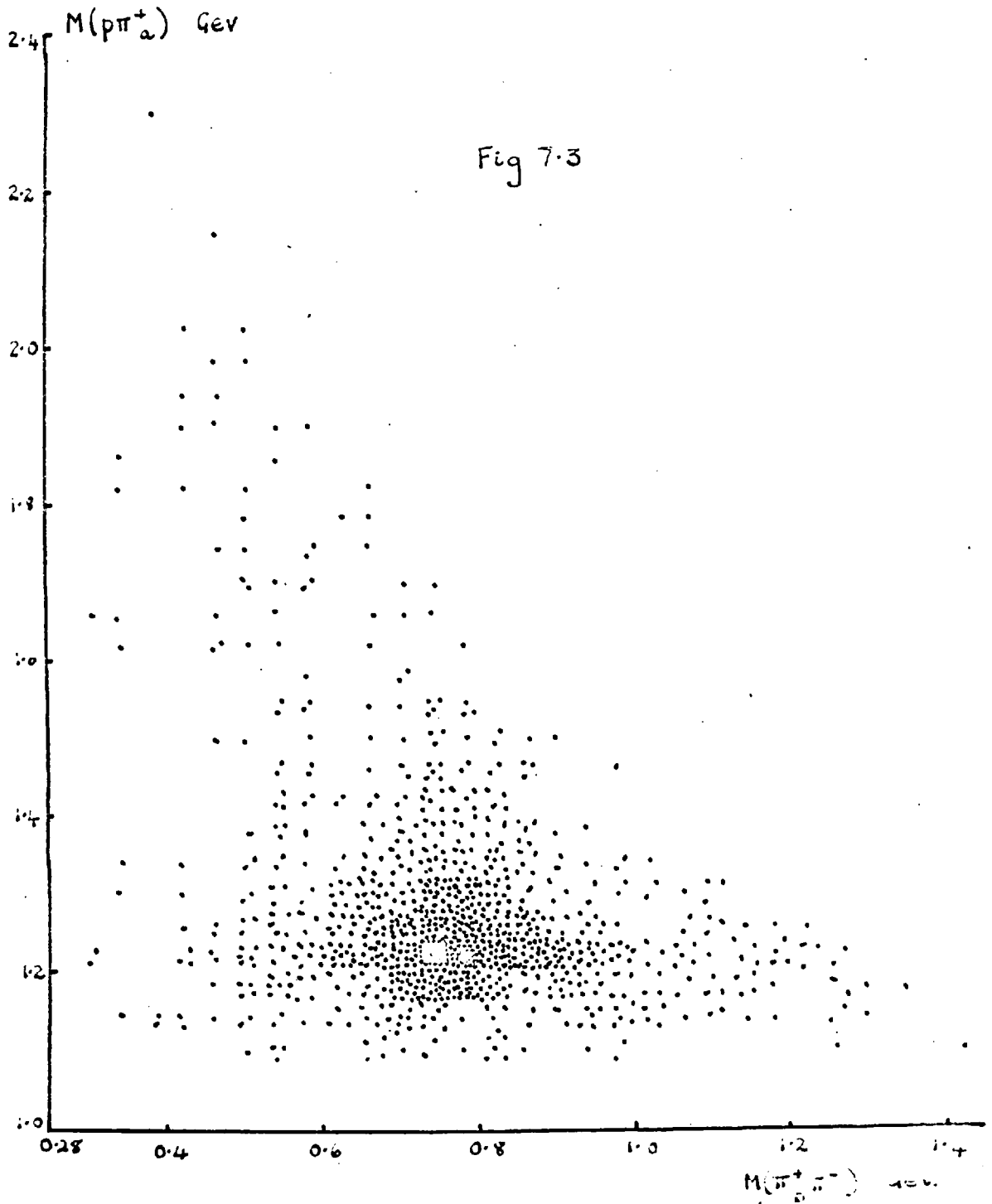
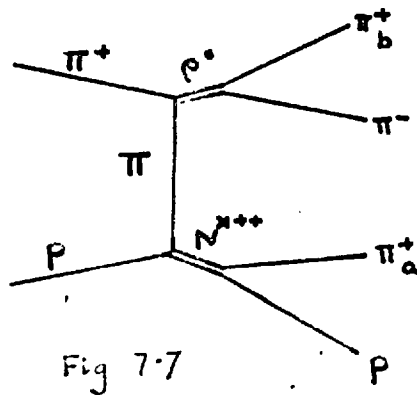
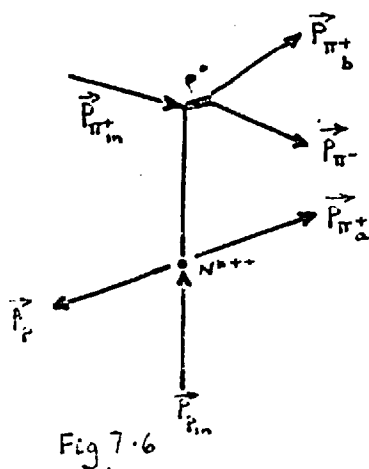
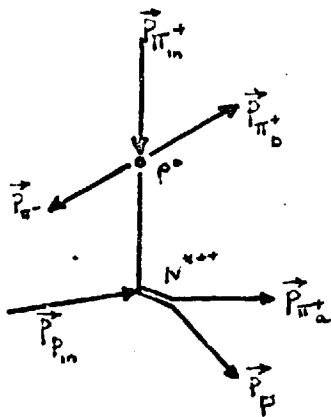
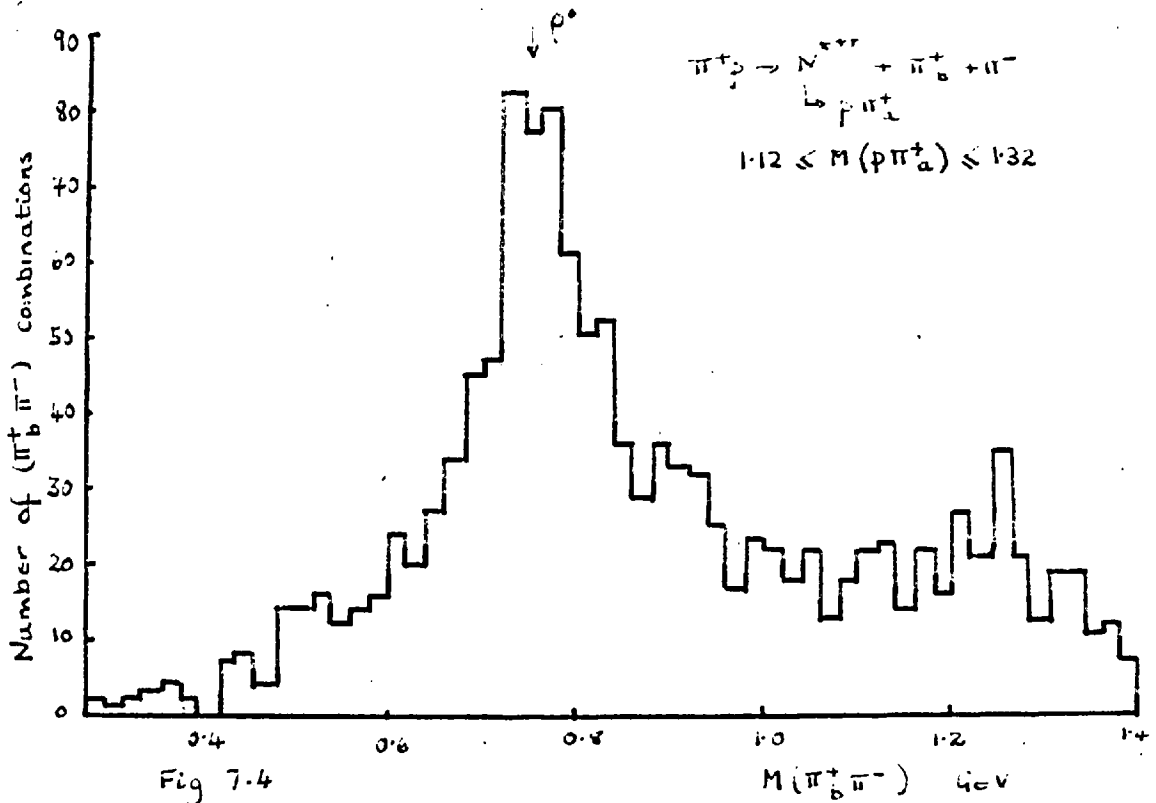


Fig 7-2



SCATTER DIAGRAM for  $M(p\pi_a^+)$  v.  $M(\pi_b^+ \pi^-)$   
for  $\Delta^2(p/\pi\pi_a^+) < 0.3 \text{ GeV}^2$



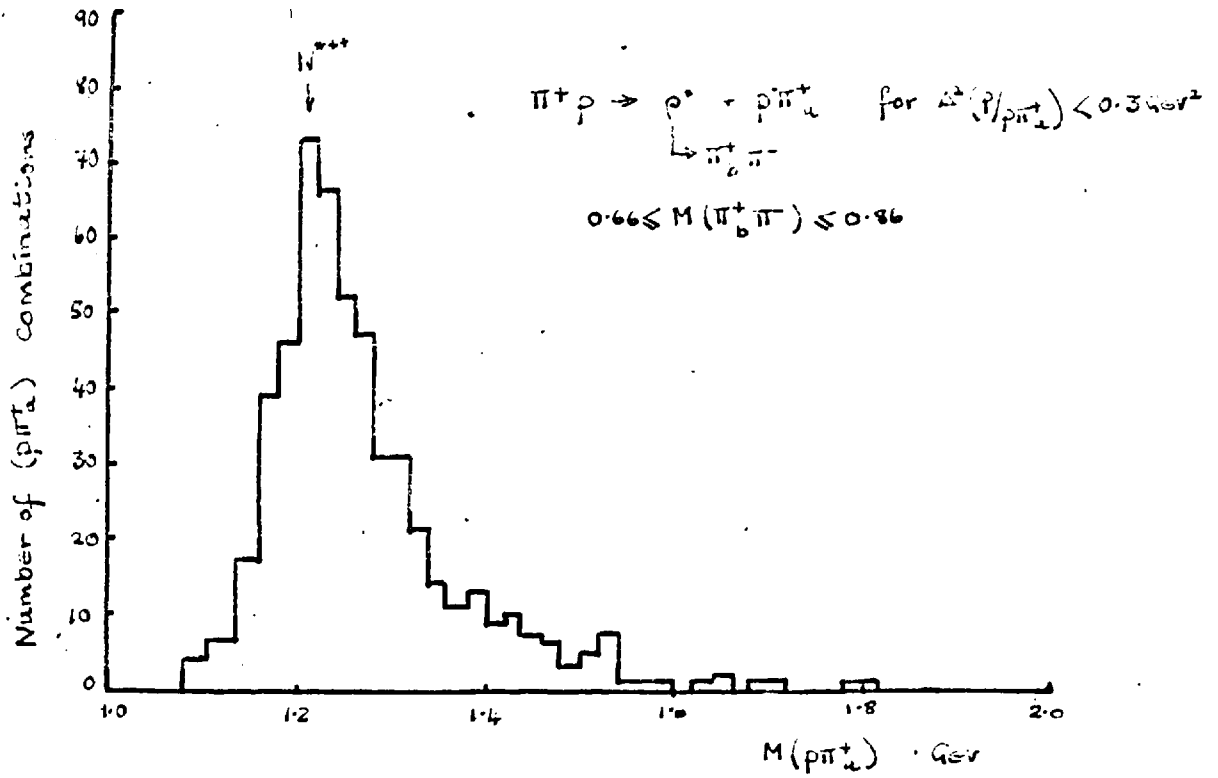


Fig 7.8

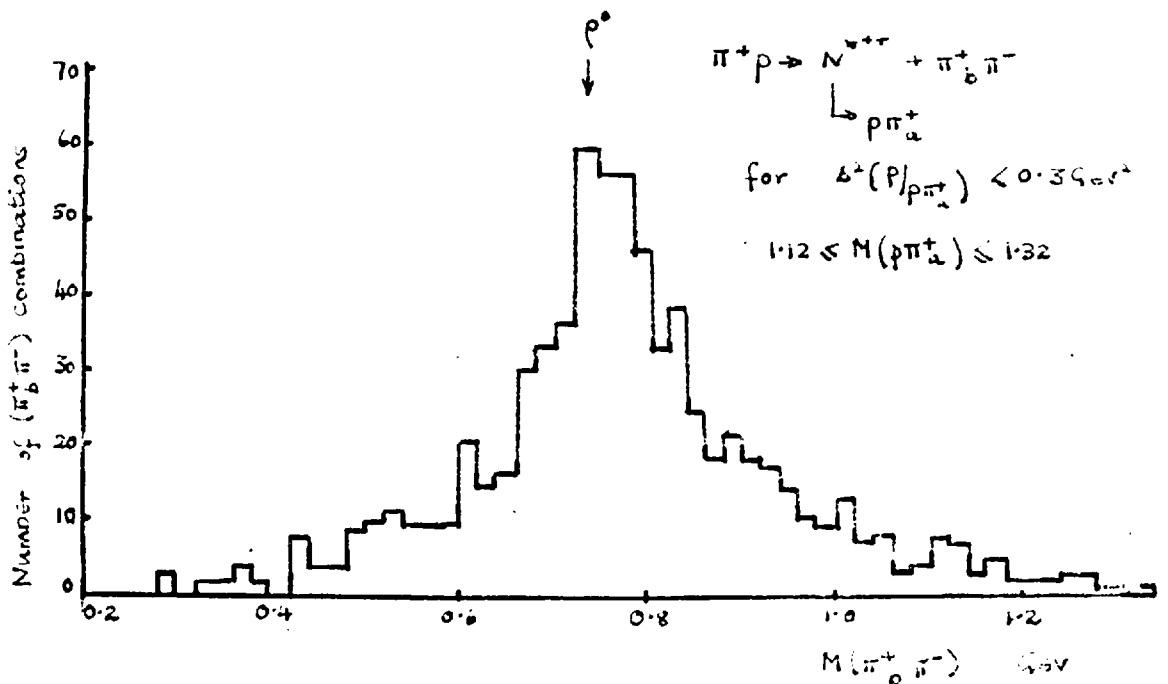
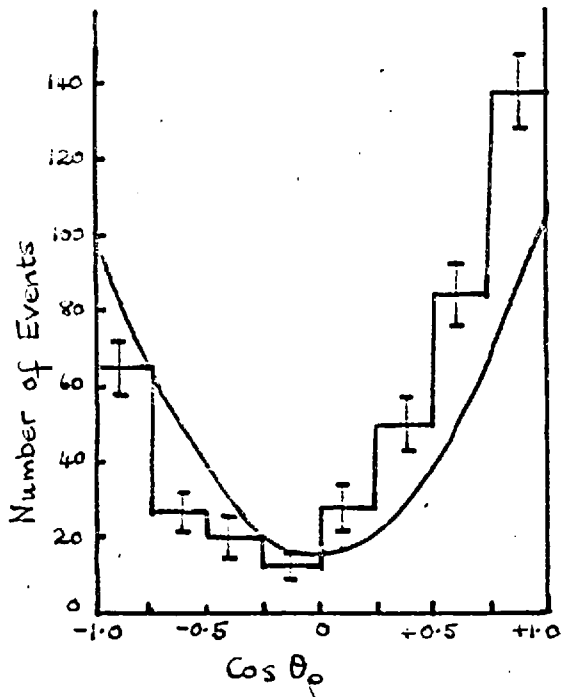
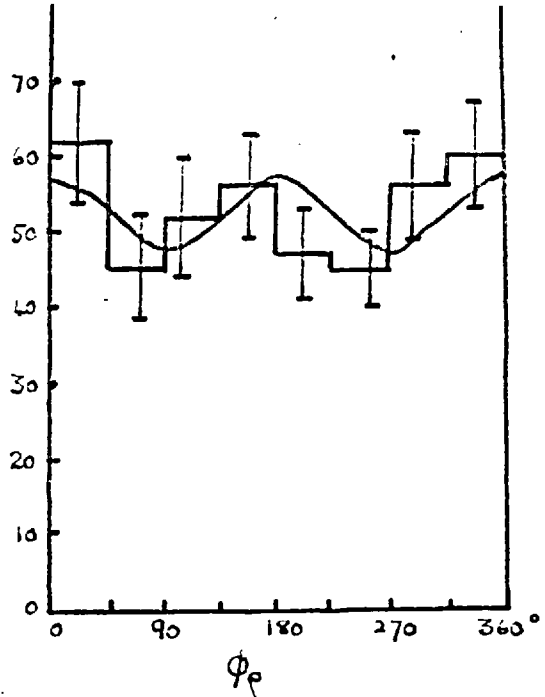


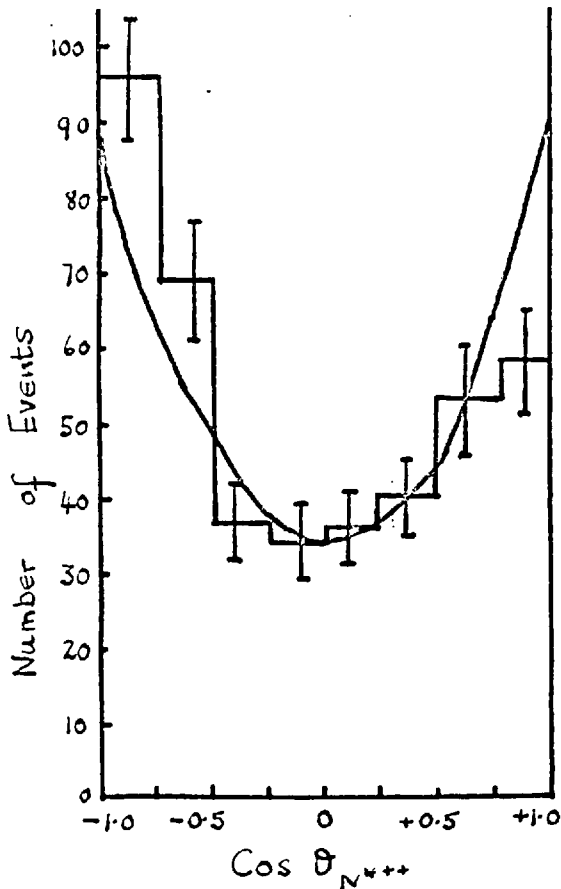
Fig 7.9



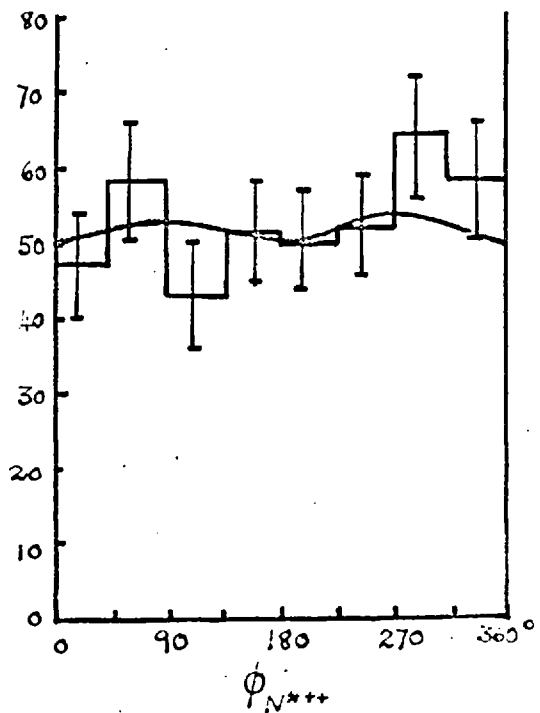
$\cos \theta_p$   
Fig 7.10



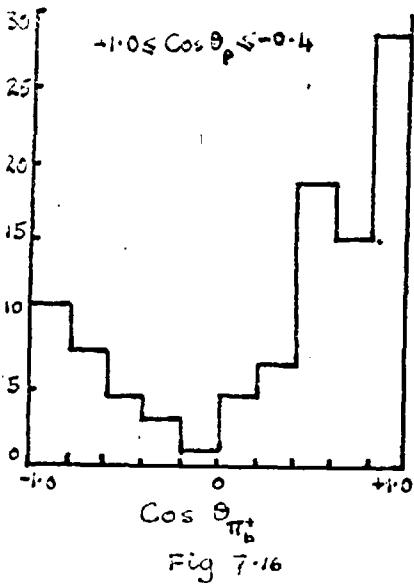
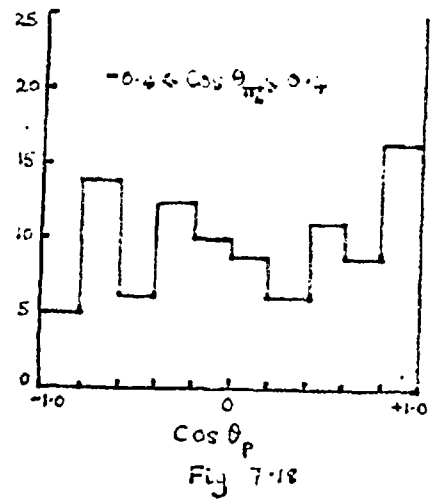
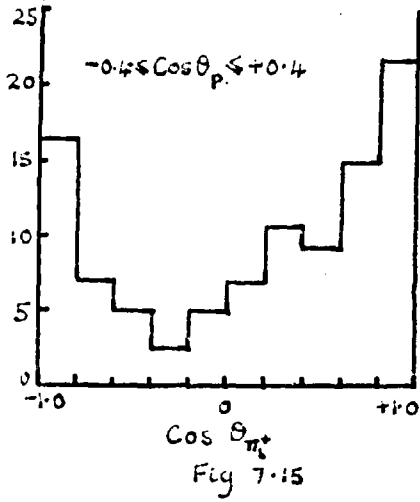
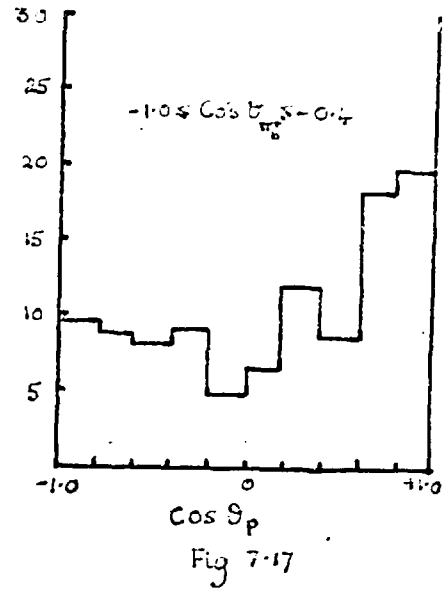
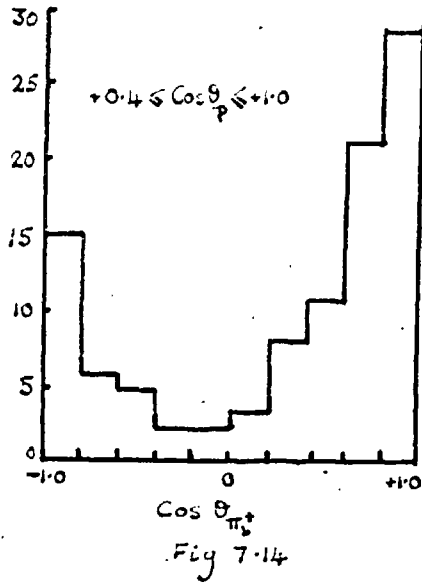
$\phi_p$   
Fig 7.11



$\cos \theta_{N^{*++}}$   
Fig 7.12



$\phi_{N^{*++}}$   
Fig 7.13



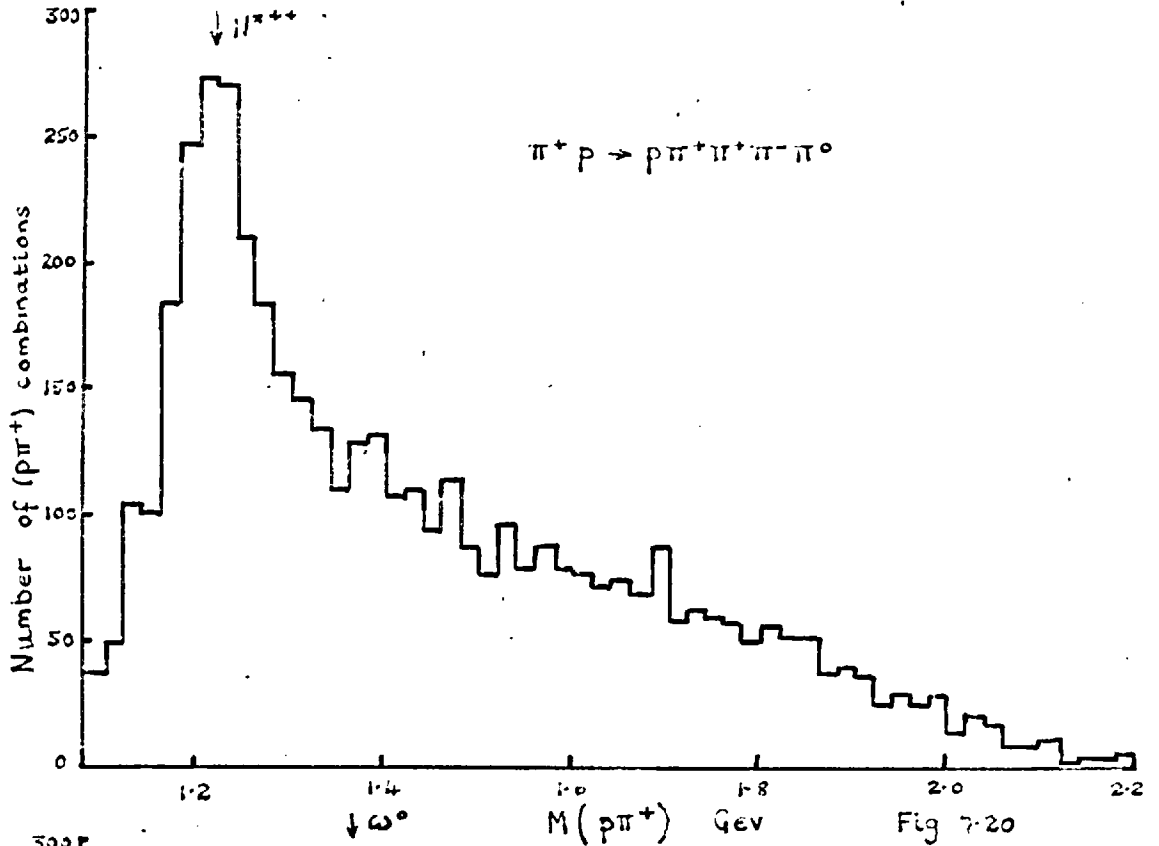


Fig 7.20

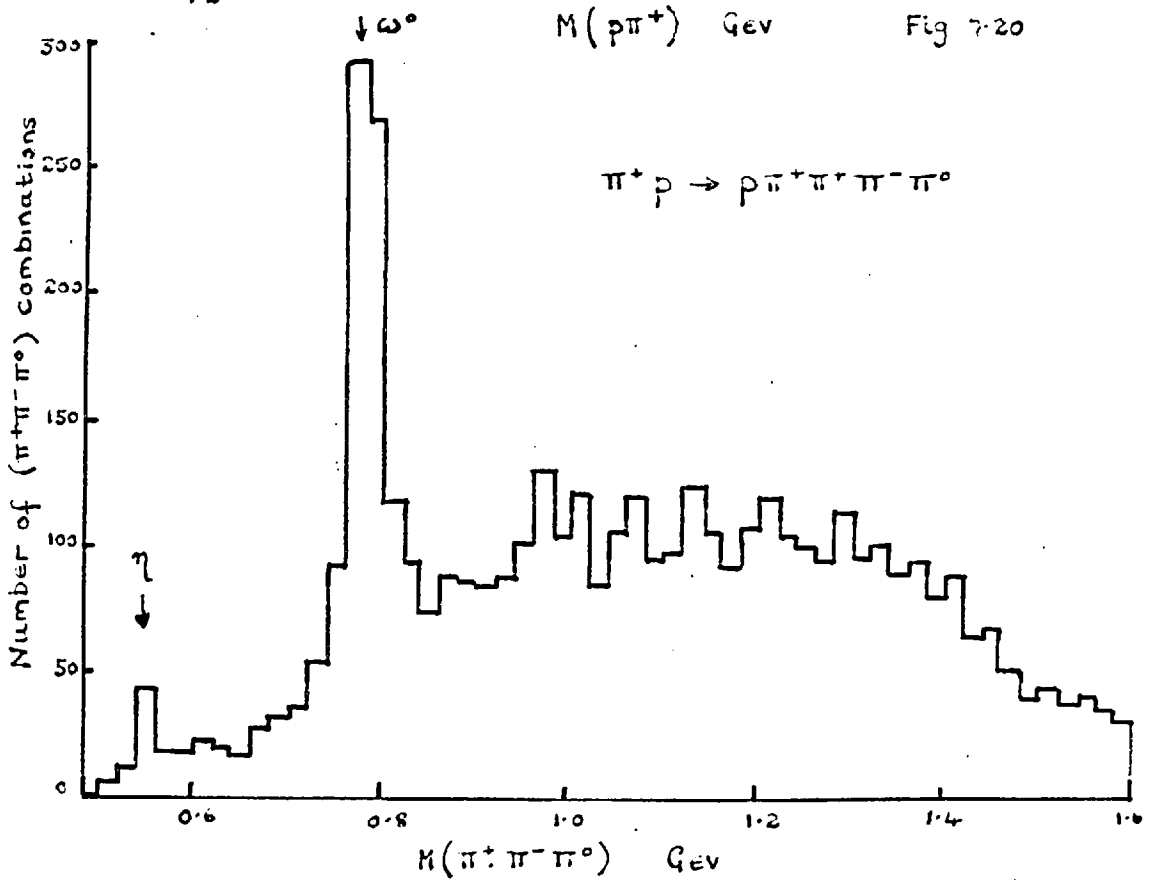


Fig 7.21

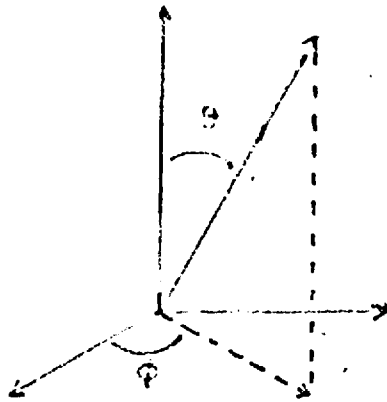


Fig 7-22

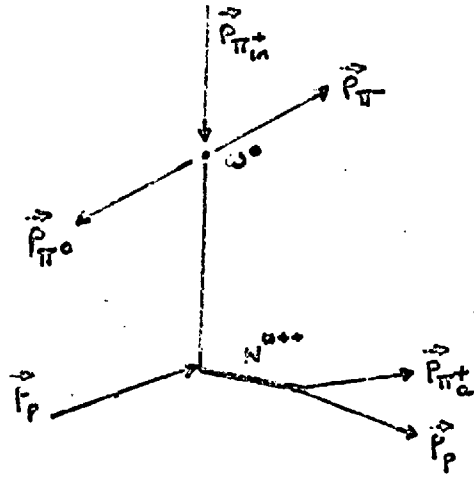


Fig 7-24

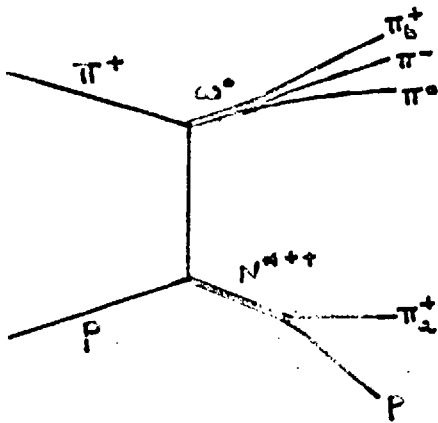


Fig 7-23

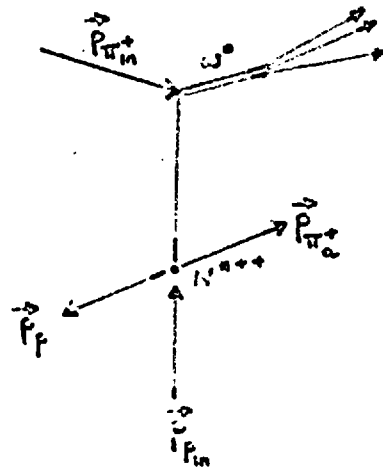
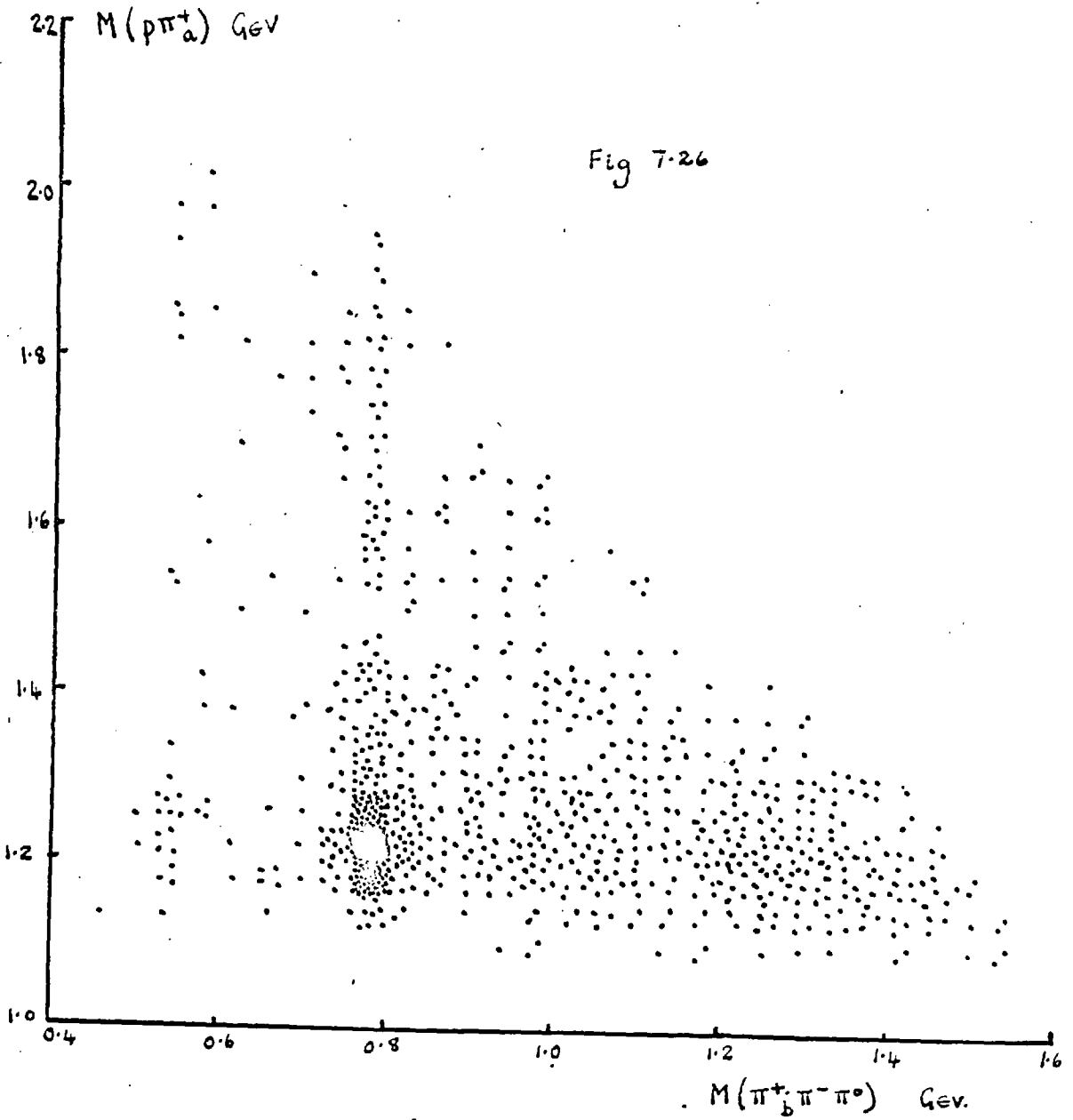
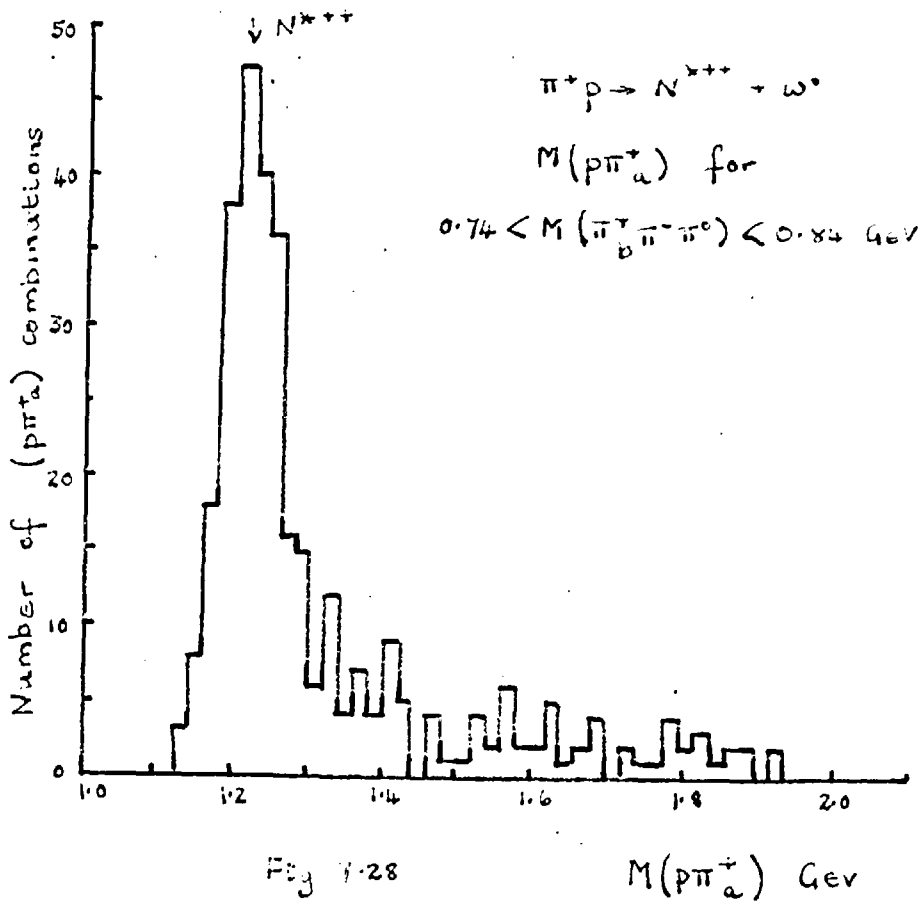
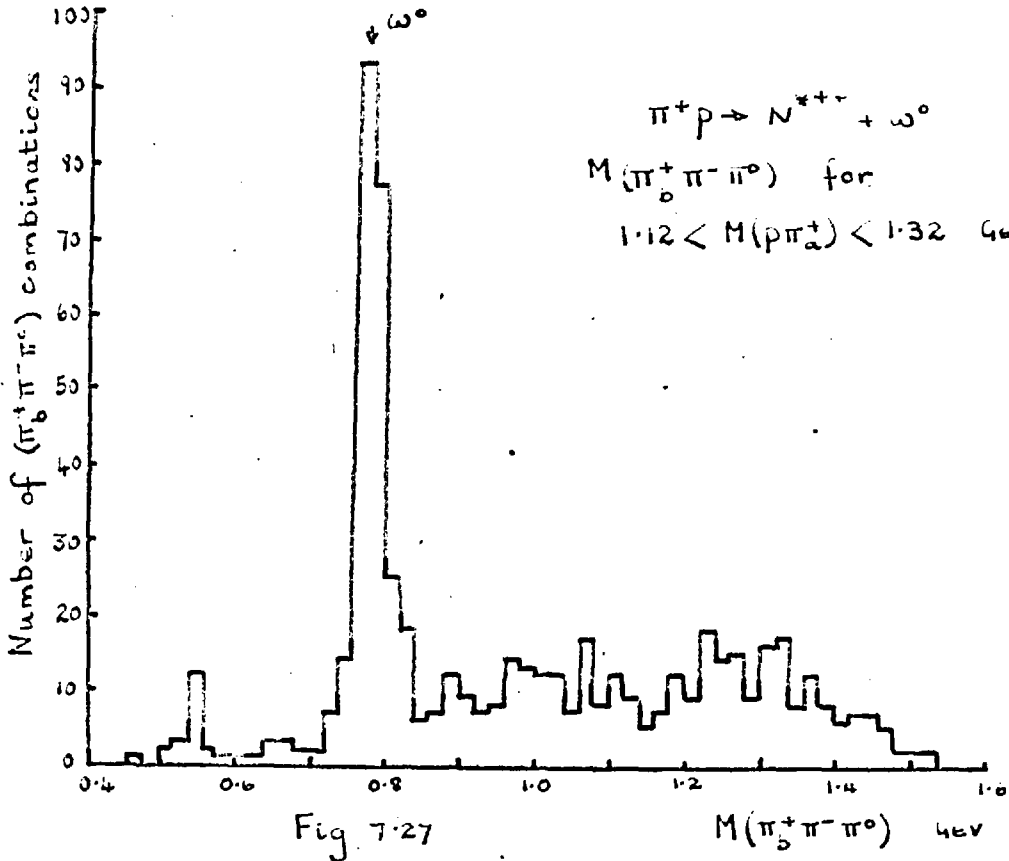
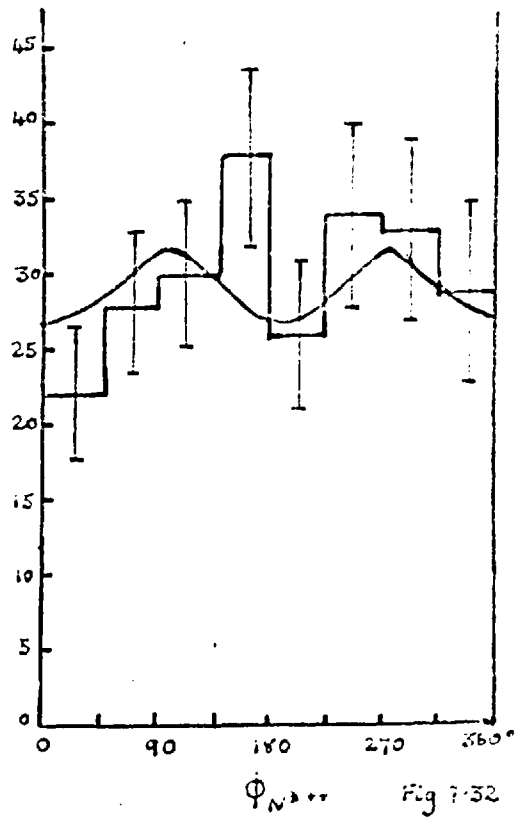
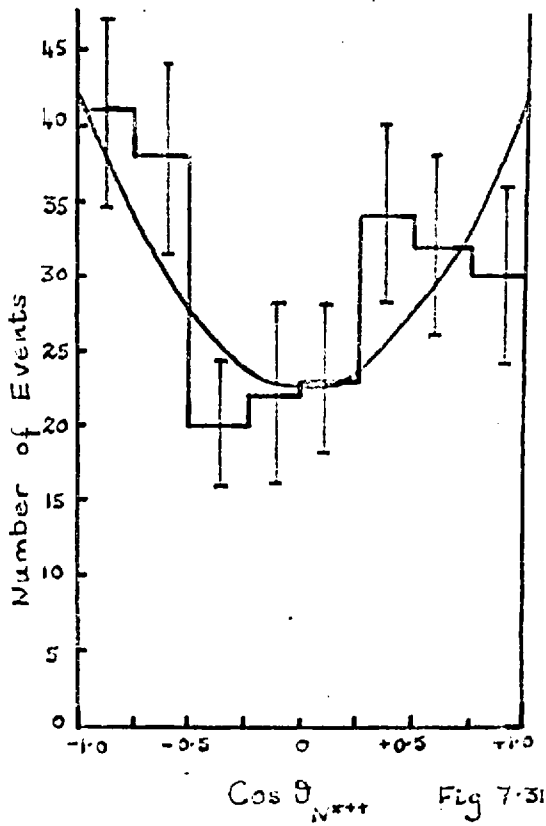
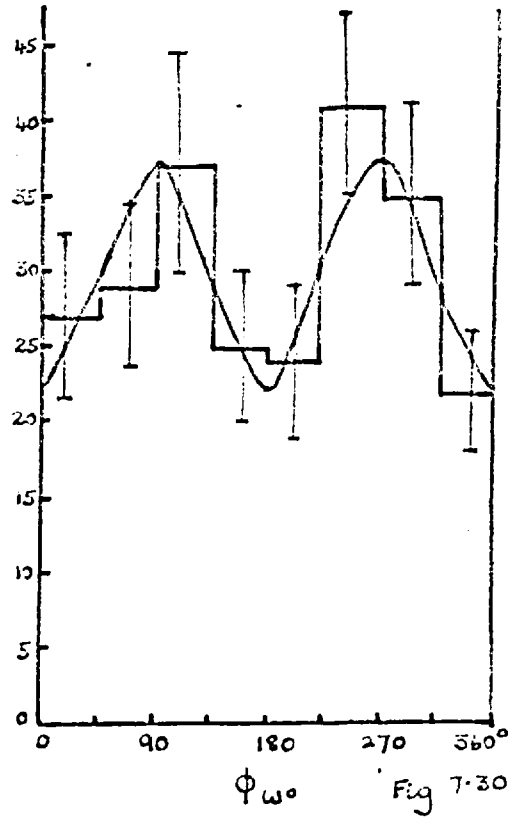
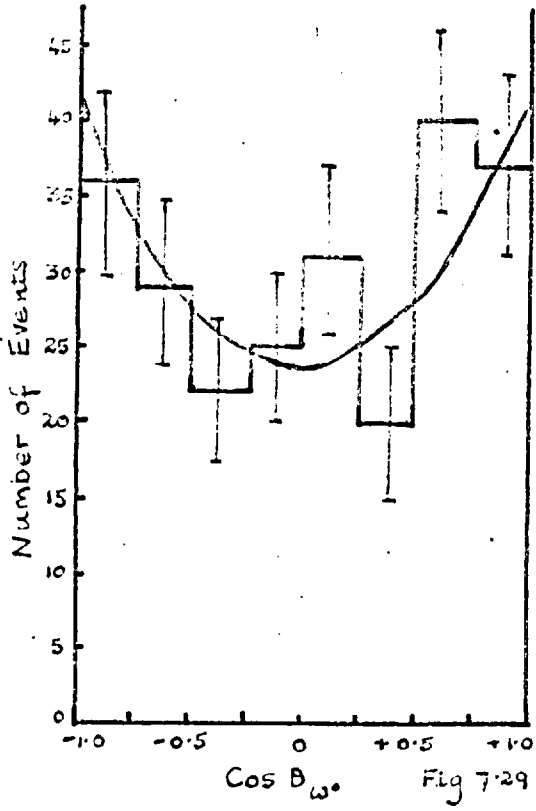


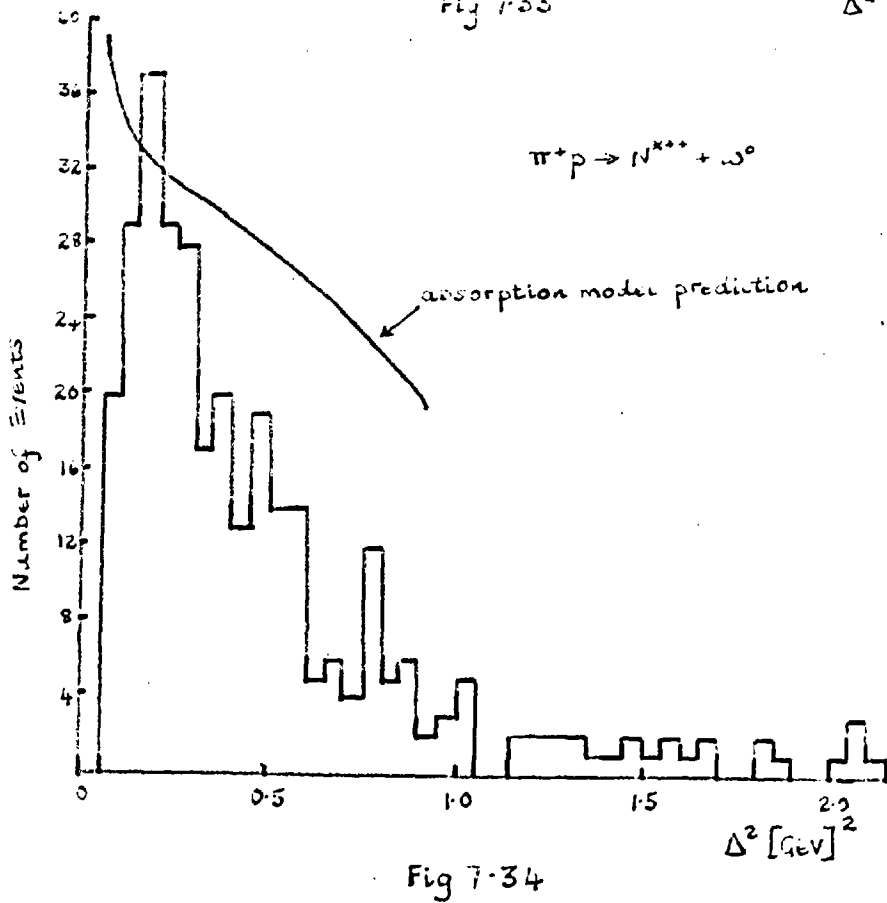
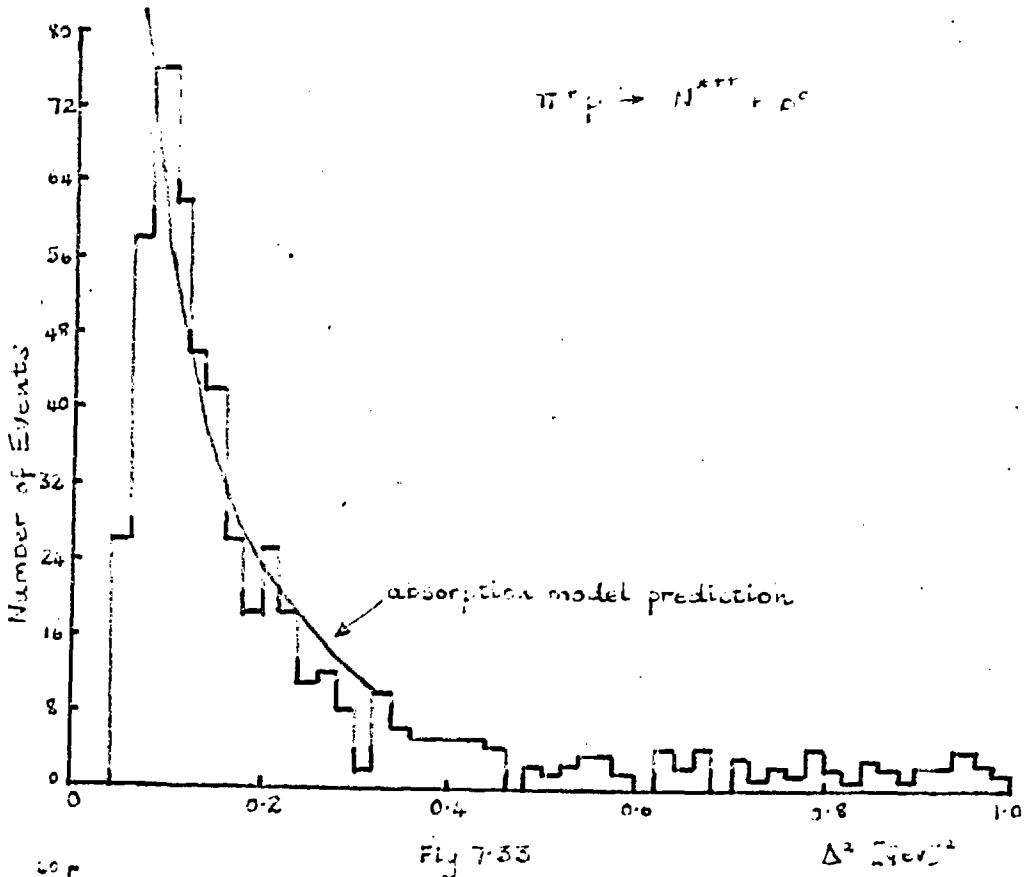
Fig 7-25



SCATTER DIAGRAM for  $M(p\pi_a^+) \vee M(\pi_b^+ \pi^- \pi^0)$   
for  $\Delta^2(p/p\pi_a^+) < 0.6 \text{ GeV}^2$







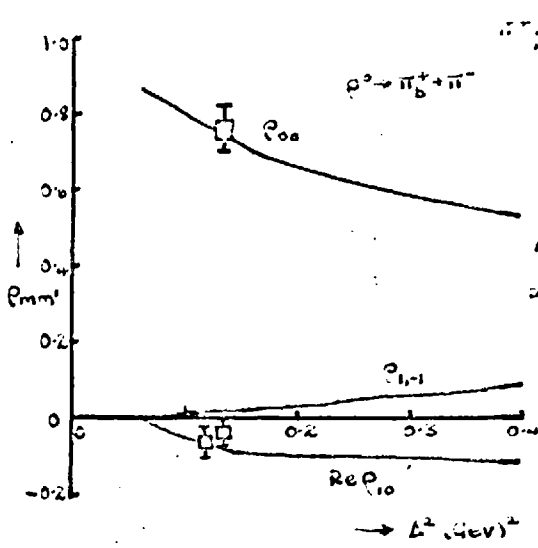


Fig 7-35.

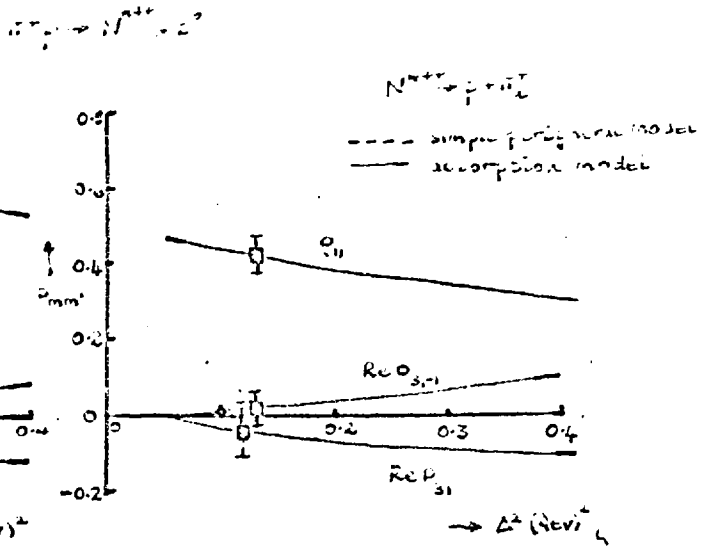


Fig 7-36

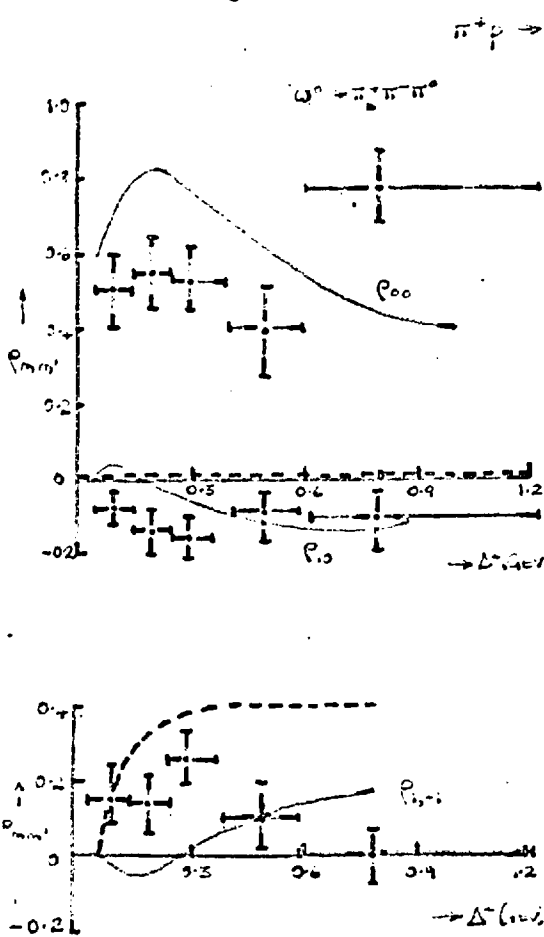


Fig 7-37

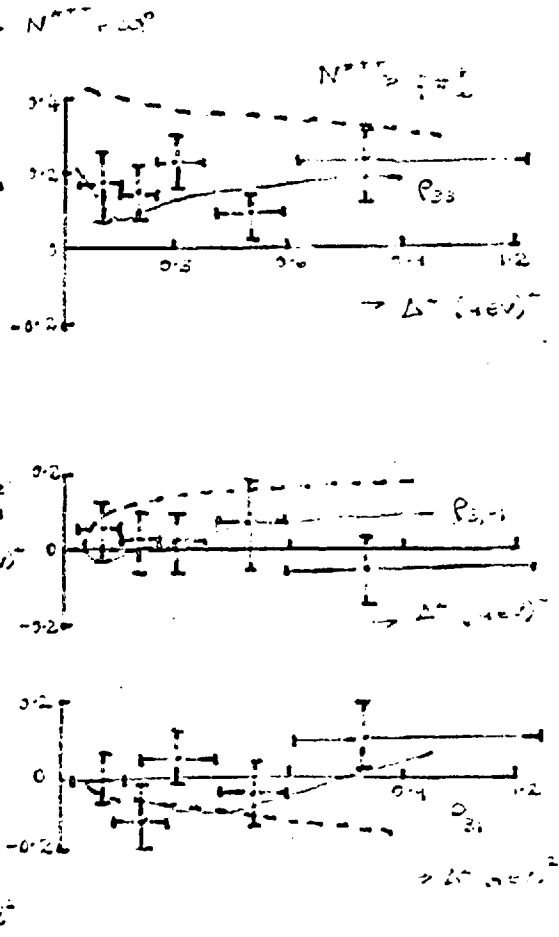


Fig 7-38

CHAPTER 8

K $\bar{K}$  DECAY MODES OF SOME NON-STRANGE MESONIC RESONANCES

8.1 Introduction

Many of the recently discovered mesonic resonances (e.g.  $f^0$ ,  $B$ ,  $A_1$ ,  $A_2$ ) could be expected to have  $K\bar{K}$  decay modes for certain quantum number assignments. In some cases where the spin and parity are unknown, the observation of a  $K\bar{K}$  decay mode can reduce the number of possible spin and parity assignments.

Goldhaber Lee and Yang (58) have determined the allowed  $K\bar{K}$  modes with zero strangeness, for different values of the charge, I-spin and G-parity.

There are eight possible states:-

$$Q = I_3 = 1 \quad K^+ \bar{K}^0; \quad \bar{K}^0 K^+$$

$$Q = I_3 = -1 \quad K^- \bar{K}^0; \quad K^0 \bar{K}^-$$

$$Q = I_3 = 0 \quad K^0 \bar{K}^0; \quad \bar{K}^0 K^0; \quad K^+ \bar{K}^-; \quad K^- \bar{K}^+$$

Any general state, for a particular value of  $Q$ , can be formed from these by superposition of the relevant states. If G-parity is now included, the actual eigenstates for  $S = 0$  can be calculated for particular values of  $Q$ ,  $I$  and  $G$ . These can be written in terms of  $K_1^0$  and  $K_2^0$  instead of  $K^0$  and  $\bar{K}^0$  so that the eigenstates for the observed decay modes will be as follows:

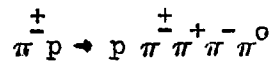
$Q = I_3$	$I$	$G$	cigenstate of the observed decay modes
+1	1	$\bar{+}1$	$\frac{1}{2} ((K^+K_1^0) - i(K^+K_2^0) \pm (K_1^0K^+) \mp i(K_2^0K^+))$
-1	1	$\bar{-}1$	$-\frac{1}{2} ((K_1^0K^-) + i(K_2^0K^-) \pm (K^-K_1^0) \mp i(K^-K_2^0))$
0	1	-1	$\frac{1}{2} ((K^+K^-) - (K^-K^+) + (K_1^0K_1^0) + (K_2^0K_2^0))$
0	1	+1	$\frac{1}{2} ((K^+K^-) + (K^-K^+) - i(K_1^0K_2^0) + i(K_2^0K_1^0))$
0	0	-1	$\frac{1}{2} ((K^+K^-) + (K^-K^+) + i(K_1^0K_2^0) - i(K_2^0K_1^0))$
0	0	+1	$\frac{1}{2} ((K^+K^-) - (K^-K^+) - (K_1^0K_1^0) - (K_2^0K_2^0))$

From this table it can be seen that for an  $I = 1$  resonance, if it had a  $K\bar{K}$  decay mode, then it should be detected in the  $K^+K_1^0$  and  $K^+K^-$  modes, and the neutral component would be seen as  $K_1^+K_1^0$  for  $C(\equiv G) = +1$  or  $K_1^+K_2^0$  for  $C(\equiv G) = -1$ .

For an  $I = 0$  resonance, the only observable decay modes are  $K^+K^-$ ,  $K_1^0K_1^0$  and  $K_1^0K_2^0$  and the relative production of  $K^+K^-:K_1^0K_1^0$  or  $K^+K^-:K_1^0K_2^0$  depends on the  $C$ -parity of the resonance.

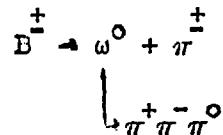
### 8.2 The Buddha Meson

The existence of an  $\omega\pi$  resonance at a mass of 1.215 Gev has been reported (25) in the reactions



but except for its  $I$ -spin and  $G$ -parity, the quantum numbers are uncertain.

The predominant decay mode is



which demands that  $I = 1$  and  $G = +1$ .

Attempts (9, 59) have been made to determine the spin and parity, but no definite assignments have been made. The experimental data suggests that  $J^P = 1^-$  but the  $2\pi$  and  $K\bar{K}$  decay modes expected of an  $I = 1$ ,  $J^{PG} = 1^{-+}$  particle have not been seen. If, however,  $J^{PG} = 1^{++}$  then the  $2\pi$  and  $K\bar{K}$  decay modes are forbidden for both strong and electromagnetic decays, while a  $J^P = 0^+$  assignment is forbidden for a particle with an  $\omega\pi$  decay mode.

In this experiment an attempt has been made to determine  $J^P$  for the Buddha from the analysis of the decay angular correlations of the  $\omega^0$  from the decay of the Buddha. Estimates are also given for the strength of the  $2\pi$  and  $K\bar{K}$  decay modes.

### 8.3 The Reaction $\pi^+p \rightarrow pB^+$ (9)

The  $\omega\pi^+$  decay mode of the Buddha was studied in the reaction at 4 GeV/c.

$\pi^+p \rightarrow p \pi_a^+ \pi_b^+ \pi_c^- \pi_d^0$  which was dominated by  $N^{*++}$  and  $\omega^0$  production as can be seen

in the scatter diagram Figure 8.1. This also shows that about

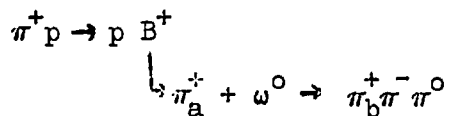
10% of the events proceed by the channel

$$\pi^+p \rightarrow N^{*++} + \omega^0 \quad (1)$$

which was discussed in detail in Section 7.4.

The  $\omega\pi^+$  decay mode of the  $B^+$  should be apparent in the effective mass distribution of the  $(\pi^+\pi^+\pi^-\pi^0)$  combination with the condition that at least one of the  $\pi^+\pi^-\pi^0$  effective masses lies in the  $\omega^0$  region (0.74 - 0.84 Gev). This distribution is shown in Figure 8.2 where a weak enhancement is observed at the Buddha mass. If both  $\pi^+\pi^-\pi^0$  effective masses lay in the  $\omega^0$  region only one point has been plotted.

In order to remove as much background as possible, all events which were of channel (1) were removed. This was done by replotting Figure 8.2 with the additional restriction that both  $p\pi^+$  effective masses lay outside the  $N^{*++}$  region (1.12 - 1.32 Gev). The resulting distribution is given in Figure 8.3 and the B-meson is now seen quite strongly, though there is still a large background. It was not possible to reduce the background any further by selecting events with low four momentum transfer to the proton. Figure 8.3 is compared with a phase space normalised to all events outside the Buddha region (1.16 - 1.36 Gev) and from this the cross-section for the reaction



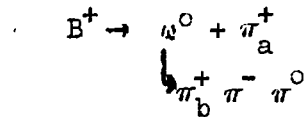
was estimated to be 0.09 millibarns  $\pm$  20%

#### 8.4 The Determination of the Spin and Parity of the Buddha

Although the background is so high ( $\sim 1:1$  with  $B^+$  production) an attempt was made to determine the spin and parity.

Different spin and parity assignments for the Buddha influenced the decay angular distributions of the  $\omega^0$  in the following way.

Consider the decay



then conservation of total angular momentum and parity demands that

$$\text{angular momentum conservation } |J, J_z\rangle = |1, 1\rangle + |0, 0\rangle + |L, L_z\rangle$$

$$\text{Parity conservation } P_B = (-1) (-1) (-1)^L$$

$$P_B = (-1)^L$$

where  $|L, L_z\rangle$  is the orbital angular momentum.

Now  $L_z = 0$  along the chosen direction of quantization (in this case the  $\omega^0$  line of flight), so that if the Buddha had parity  $P_B = (-1)^J$  which gives possible  $J^P$  assignments of  $1^-, 2^+$  etc then  $L = J$ . Consider  $J^P = 1^-$  for example; this then restricts the possible spin states for the  $\omega^0$  to be  $|1^\pm\rangle$  with respect to its line of flight, as the Clebsch-Gordon coefficient for the coupling of two  $|1, 0\rangle$  states is zero.

Similar arguments can be used for a  $J^P = 0^-$  assignment for

the Buddha, which results in the  $\omega^0$  being in a spin state  $|1, 0\rangle$  with respect to its line of flight.

For parity assignments  $P_B = (-1)^{J+1}$ , i.e.  $J^P$  assignments of  $1^+, 2^-$  etc., no unique spin states can be specified for the  $\omega^0$ , so that it is not possible to exclude these possible spin and parity assignments in the following analysis.

The decay angular distribution of the  $\omega^0$  was studied using the angle  $\beta$ ;  $\beta$  is defined as the angle between the normal to the  $\omega^0$  decay plane and the  $\omega^0$  line of flight (i.e. the direction of  $\pi_a^+$ ), where all vectors are defined in the  $\omega^0$  centre of mass.

Then  $\cos \beta$  is defined as

$$\cos \beta = \frac{\vec{p}_{\pi_a^+} \cdot (\vec{p}_{\pi^0} \times \vec{p}_{\pi^-})}{|\vec{p}_{\pi_a^+}| |\vec{p}_{\pi^0} \times \vec{p}_{\pi^-}|}$$

For  $P_B = (-1)^J$  assignments  $\cos \beta$  would be characterized by the spin spherical harmonic of the  $|1, \pm 1\rangle$  state, i.e. by  $|Y_1^{\pm 1}|^2 \propto \sin^2 \beta$ ; for  $J^P = 0^-$ ,  $\cos \beta$  will be characterized by  $|Y_0^1|^2 \propto \cos^2 \beta$ .

$\cos \beta$  has been calculated for the three regions of the  $\pi^+ \pi^+ \pi^- \pi^0$  effective masses which are shown in Figure 8.3; these regions are (A)  $0.96 < M(\pi^+ \pi^+ \pi^- \pi^0) < 1.16$  Gev; (B)  $1.16 < M(\pi^+ \pi^+ \pi^- \pi^0) < 1.36$  Gev (the Buddha region), (C)  $1.36 < M(\pi^+ \pi^+ \pi^- \pi^0) < 1.56$  Gev.

The distributions for  $\text{Cos}^2 \beta$  are shown in Figures 8.4, 8.5 and 8.6 for regions A, B and C. In Figure 8.5 the distribution for a normalised background is also given (the shaded area). This was determined by estimating the background under the Buddha from Figure 8.3 and then normalising the average of the distributions A and C to this number of events.

The decay angular distribution for the Buddha region (B) with the background subtracted is shown in Figure 8.7 and it is compared to a  $\text{Sin}^2 \beta$  distribution. The agreement between the curve and the distribution is not good, so that the only assignment that can be excluded is  $J^P = 0^-$  as this distribution does not have a  $\text{Cos}^2 \beta$  dependence.

The uncertain background prevents any definite conclusion being reached, but perhaps the B-meson has  $J^P = 1^-$ . This would be in agreement with Carmony's results <sup>(59)</sup> obtained from the analysis of the data using Halpern plots <sup>(60)</sup>, but the possibility that  $J^P = 1^+$  cannot be excluded. If the Buddha has  $J^P = 1^-$ , then it would be expected to have significant  $2\pi$  and  $K\bar{K}$  decay modes.

#### 8.5 The Search for the Decay Mode $B \rightarrow 2\pi$

To find the  $2\pi$  decay mode <sup>(4)</sup>, the effective mass distributions for the  $(\pi^{\pm} \pi^0)$  combinations respectively were made (Figures 8.8 and 8.9) for the following reactions at 4 GeV/c incident pion

momentum.

$$\pi^+ p \rightarrow p \pi^+ \pi^0 \quad (1278 \text{ events})$$

$$\pi^- p \rightarrow p \pi^- \pi^0 \quad (440 \text{ events})$$

These distributions are compared with Lorentz invariant phase spaces normalised to all events outside the  $\rho^+$  region respectively.

No significant enhancements can be seen in the Buddha region. This meant that an upper limit could be calculated for the  $B^+ \rightarrow \pi^+ \pi^0$  decay mode. It was estimated that an enhancement of 25 events over phase space could be detected, and as the width of the Buddha was known, the ratio for  $B^+ \rightarrow \pi^+ \pi^0$  could be

$$\frac{B^+ \rightarrow \pi^+ \pi^0}{B^+ \rightarrow \pi^+ \omega^0}$$

calculated using the known cross-sections for  $B^+ \rightarrow \pi^+ \pi^0$ . This gave

$$\frac{B^+ \rightarrow \pi^+ \pi^0}{B^+ \rightarrow \pi^+ \omega^0} \leq 40\%$$

This means that the  $2\pi$  decay mode is very weak, which is evidence against the spin parity assignment of  $J^P = 1^-$  for the Buddha proposed in the last section, and favours the  $J^P = 1^+$  assignment.

### 8.6 The Search for the $K\bar{K}$ decay mode of the B-meson

It has already been shown that the known quantum numbers of the Buddha are  $I = 1$  and  $G = +1$ , and referring to Section 8.1 it

can be seen that the observed  $K\bar{K}$  decay modes would be  $B \rightarrow K^+ K_1^0$ ,  $B \rightarrow K^+ K^-$  and  $B \rightarrow K_1^0 K_2^0$ .

If in this case, as strong  $K\bar{K}$  decay mode was observed then this would strengthen the  $J^P = 1^-$  assignment proposed in Section 8.4 for the spin and parity; however, if only a weak  $K\bar{K}$  decay mode is seen, then this would suggest that the Buddha's spin and parity are probably  $J^P = 1^+$ .

The following reactions are those in which this decay mode could be observed.

$$\pi^+ p \rightarrow K^+ p K_1^0 \pi^0 \quad 20 \text{ events} \quad (1)$$

$$\pi^+ p \rightarrow K^+ \pi^+ K_1^0 n \quad 27 \text{ events} \quad (2)$$

$$\pi^+ p \rightarrow p \pi^+ K_1^0 K_2^0 \quad 35 \text{ events} \quad (3)$$

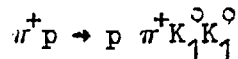
The effective mass distribution of the  $K\bar{K}$  combinations for these three reactions is shown in Figure 8.10 and the shaded area represents the events from channel (3).

A small enhancement is seen above the phase space in the region  $1.24 \rightarrow 1.36$  Gev, which is perhaps due to the  $K\bar{K}$  decay mode of the B-meson.

The only other mesonic resonances whose  $K\bar{K}$  decay modes could contribute to an enhancement in this region are the  $f^0$  and  $A_2$ .

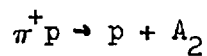
The  $f^0$  ( $M = 1.253$  Gev) has quantum numbers  $I = 0$ ,  $Q = 0$ ,  $J^P = 2^+$  and  $C = +1$  so that its  $K\bar{K}$  decay modes would be observed as  $f^0 \rightarrow K_1^0 K_1^0$  and  $f^0 \rightarrow K^+ K^-$ , this means that it cannot contribute to

this enhancement, but would be seen in the  $K_1^2 K_1^0$  effective mass distribution for the reaction



which was discussed in Section 6.3 where no evidence for this decay mode was seen.

The contribution to this enhancement due to the  $K\bar{K}$  decay mode of the  $A_2$  is more difficult to determine; the search for this decay mode is discussed in the next section so that it is sufficient to mention that as the  $A_2$  is only produced in the reaction



with preferentially low four momentum transfer to the proton, it is unlikely to be produced in reactions (1) - (3), so that this enhancement is probably not due to  $A_2$  production.

It is concluded that all of this enhancement can be attributed to the B-meson.

$$\text{Therefore } \frac{B \rightarrow K\bar{K}}{B \rightarrow \omega\pi} \leq 24\%$$

This value is consistent with a spin and parity  $J^P = 1^+$  for the B-meson, which was also preferred by the observation of the weak  $B \rightarrow 2\pi$  decay mode.

The result suggested for the spin and parity of the B-meson from the search for the  $2\pi$  and  $K\bar{K}$  decay modes is therefore in

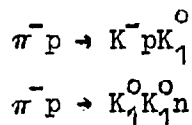
contradiction to that obtained from the analysis of the decay angular distribution of the  $\omega^0$ . However, as was stated in Section 8.4 this form of analysis could not definitely distinguish between  $J^P = 1^-$  and  $J^P = 1^+$  assignments for the B-meson.

This leads to the conclusion that when all available evidence is considered, it is most likely that the Buddha has spin and parity  $J^P = 1^+$ .

### 8.7 The Observation of the Decay Mode $A_2 \rightarrow K\bar{K}$

The existence of an  $I = 1, G = -1$   $\rho\pi$  resonance ( $A_2$ ) with a mass of 1.310 Gev has been reported by several groups (2, 23, 61). Therefore if this resonance had a  $K\bar{K}$  decay mode, this would be expected to be observed as  $A_2 \rightarrow K^+K^0$ ,  $A_2 \rightarrow K^+K^-$  or  $A_2 \rightarrow K_1^0K_1^0$ .

Chung et al. (61) at an incident  $\pi^-$  momentum of 3.77 Gev/c observed an enhancement at a  $K\bar{K}$  effective mass of 1.3 Gev in the following reactions.



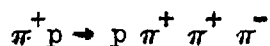
from which it was estimated that  $A_2 \rightarrow K\bar{K}$  30%

---

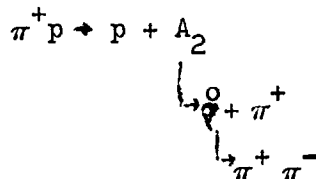
$A_2 \rightarrow \rho\pi$

The observation of this decay mode enabled the spin and parity assignment of  $J^P = 2^+$  for the  $A_2$  to be determined.

In the present experiment the  $A_2$  was observed in the reaction (2)

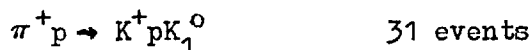


in the channel



with a cross-section of 0.24 millibarns, the  $\eta \pi$  decay mode was also seen.

The  $K\bar{K}$  decay mode was looked for in the reaction



The effective mass distribution of the  $K^+ K_1^0$  combination is shown in Figure 8.11 and it is compared with a phase space normalised to the events outside the  $A_2$  region (1.22 - 1.42 Gev). Although the statistics are poor, it can be postulated that the enhancement in the region 1.32 - 1.40 Gev is due to the  $A_2 \rightarrow K^+ K_1^0$  decay mode.

As further evidence that this enhancement is due to the decay of the  $A_2$ , the centre of mass production angle of the proton is shown in Figure 8.12. The proton is preferentially produced backwards so that this reaction is mainly produced with low four momentum transfer to the incoming proton. This implies that the events attributed to the  $A_2$  decay are also produced at low four momentum transfer, which is consistent with the results for the  $A_2 \rightarrow \rho \pi$  decay mode.

Therefore, if this enhancement is due only to the decay of

the  $A_2$ , then

$$\frac{A_2 \rightarrow K^+ K_1^0}{A_2 \rightarrow e \pi} \leq 6\%$$

This value is much lower than that reported by Chung et al.;  
but can be explained by the poor statistics.

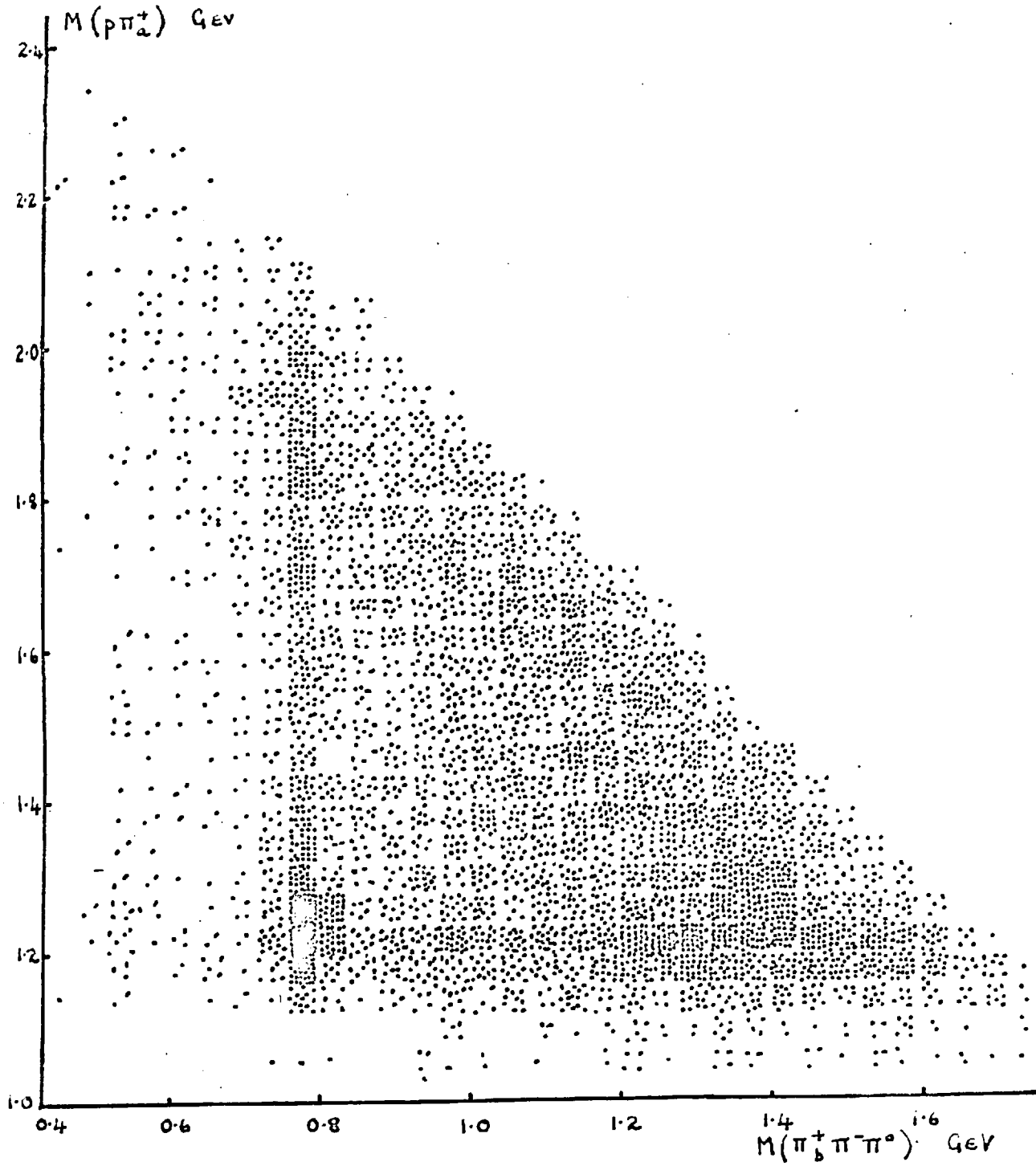


Fig 8.1

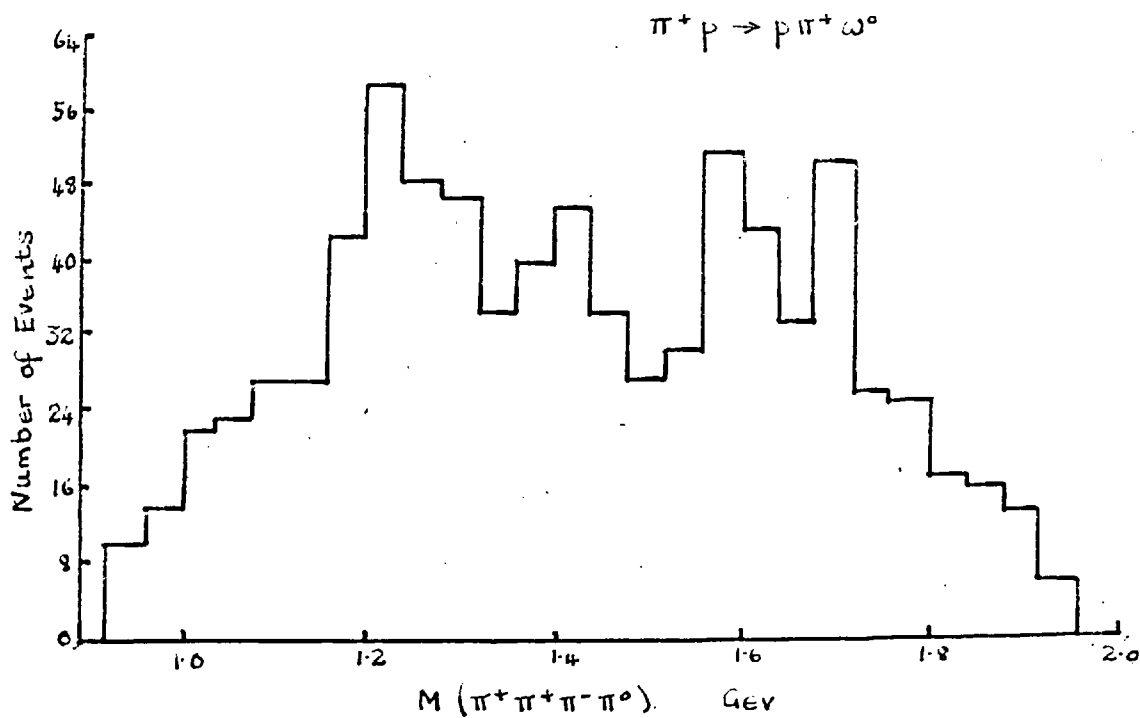


Fig 8.2

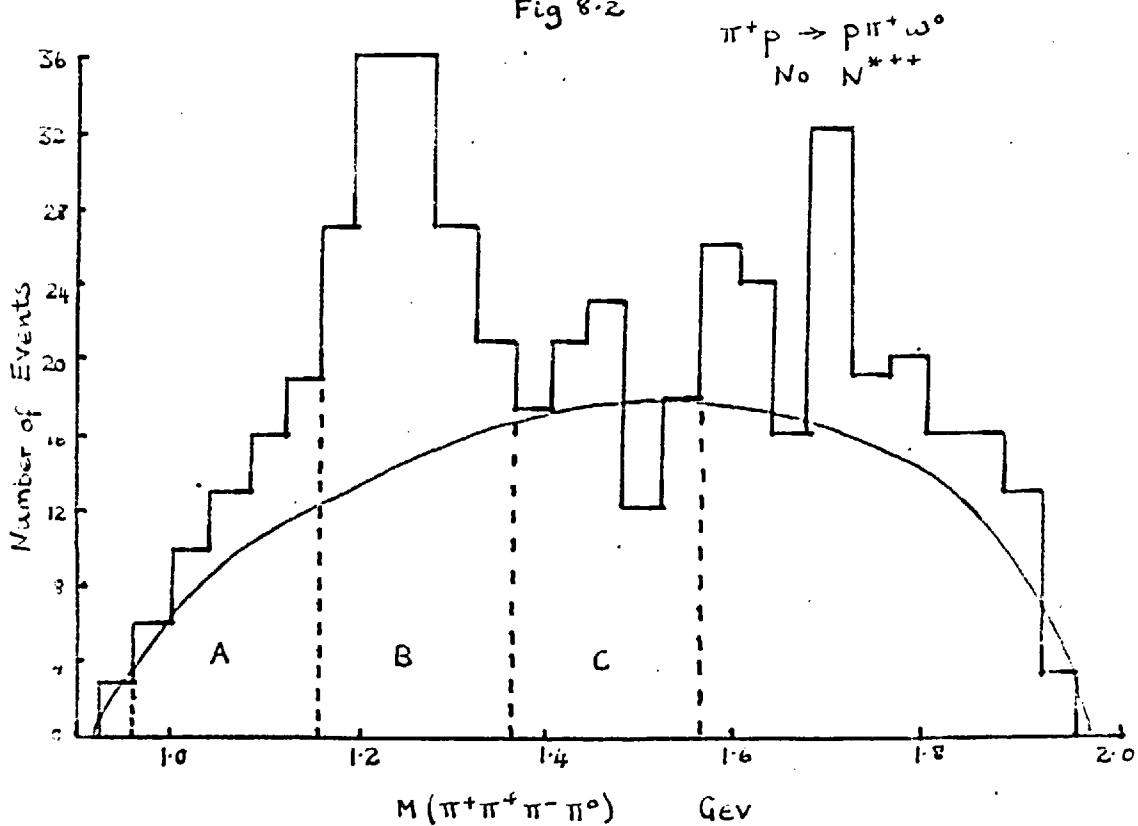


Fig 8.3

Region A

$0.96 \leq M(\pi^+\pi^+\pi^-\pi^0) \leq 1.16 \text{ GeV}$

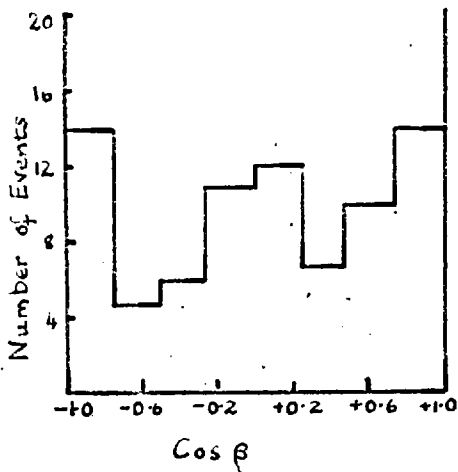


Fig 8.4

Region C

$1.36 \leq M(\pi^+\pi^+\pi^-\pi^0) \leq 1.56 \text{ GeV}$

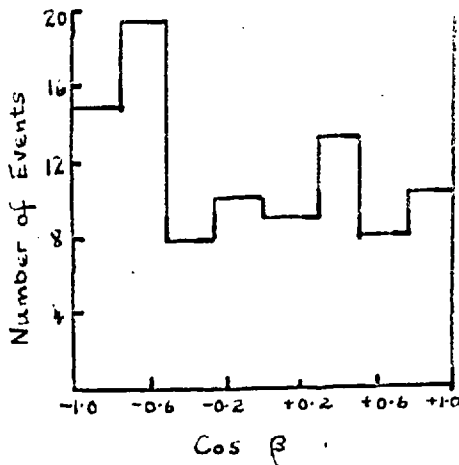
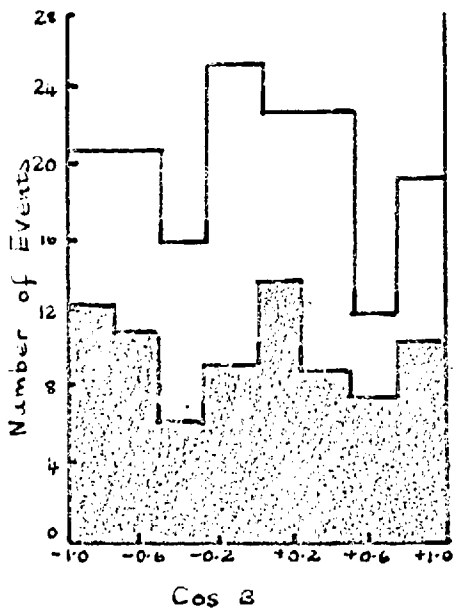


Fig 8.6

Region B (Buddha)

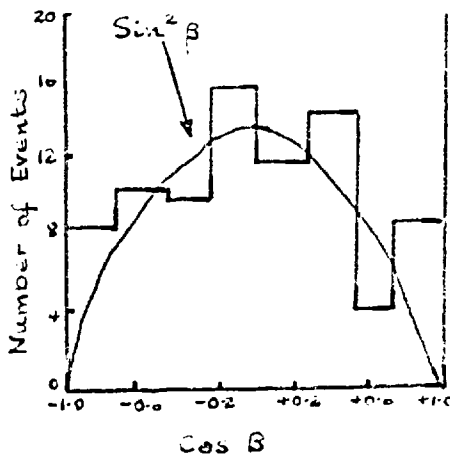
$1.16 \leq M(\pi^+\pi^+\pi^-\pi^0) \leq 1.36 \text{ GeV}$



Cos  $\beta$

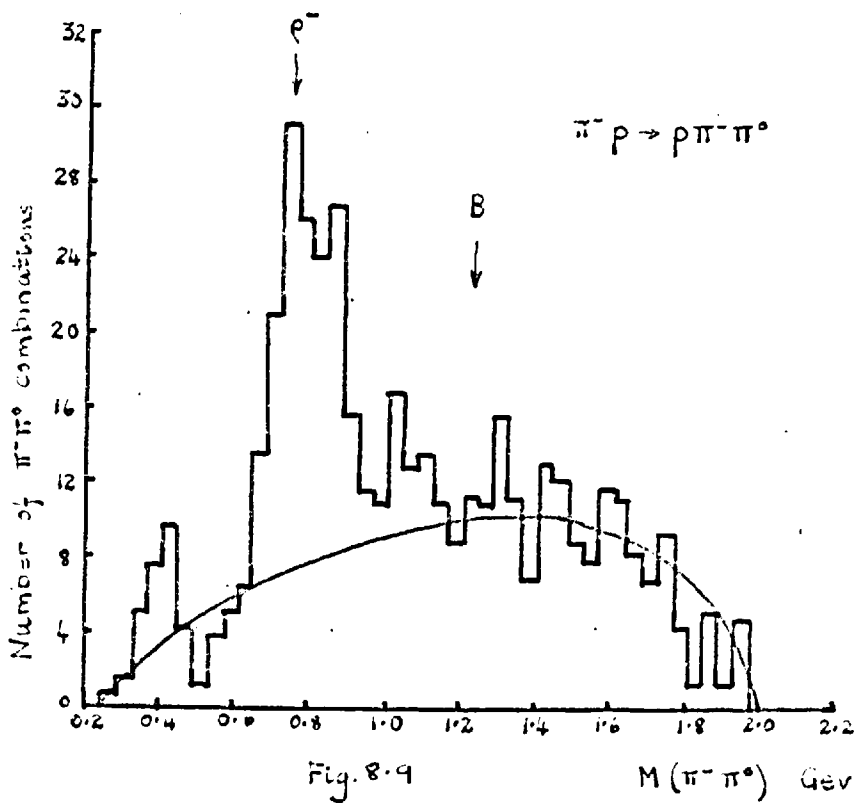
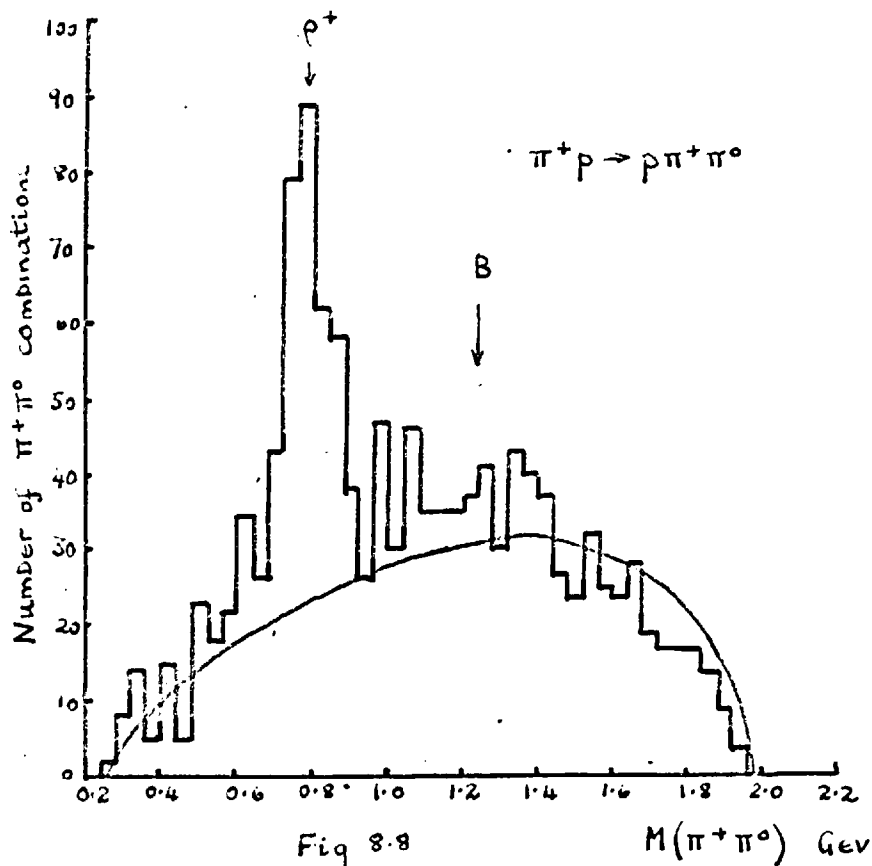
Fig 8.5

Buddha Region



Cos  $\beta$

Fig 8.7



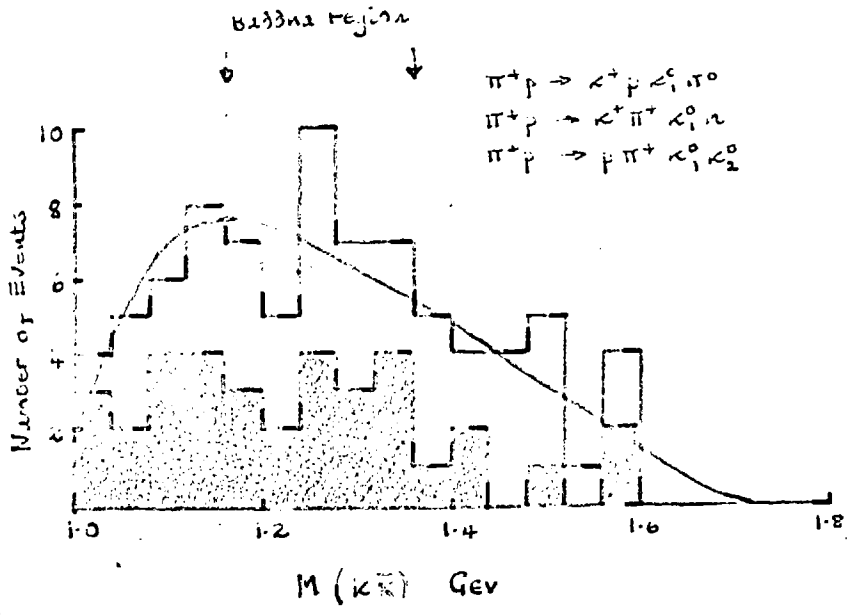


Fig. 8-10

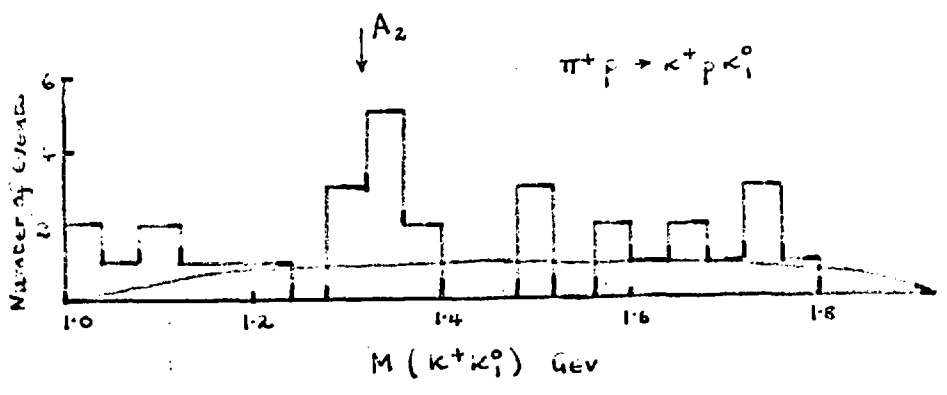


Fig 8-11

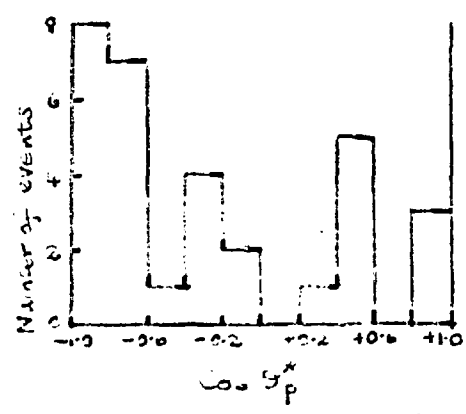


Fig 8-12

ACKNOWLEDGEMENTS

The author would like to thank Professor C.C. Butler for the opportunity of working in his laboratory and she is especially grateful for the encouragement of Dr S.J. Goldsack and Dr I. Butterworth.

The assistance of all the members of the collaboration is acknowledged, and in particular that of Mr G. Wolf of the Max-Planck Institut für Physik, Munich. The continued help of Mr Goihl and the computing staff of the Max-Planck Institut für Plasmaphysik, Garching is gratefully appreciated.

The author would like to thank all members of the High Energy Nuclear Physics Group in Imperial College for many helpful discussions and Miss Gladys Coster for her efficient book-keeping. . . .

Finally the author wishes to thank the Department of Scientific and Industrial Research for the maintenance grant between October 1961 and October 1964.

REFERENCES

1. Private communication Dr D. Luers<sup>11</sup>
2. AACHEN, BERLIN, BONN, BIRMINGHAM, HAMBURG, LONDON (IMPERIAL COLLEGE), MUNICH collaboration, Physics Letters 10 226 1964.
3. A-B-B-B-H-L-M collaboration, P.L. 10 229 1964
4. A-B-B-B-H-L-M collaboration, P.L. 10 240 1964
5. A-B-B-B-H-L-M collaboration, P.L. 10 248 1964
6. A-B-B-B-H-L-M collaboration, P.L. 11 167 1964
7. A-B-B-B-H-L-M collaboration, Nuovo Cimento 34 495 1965
8. A-B-B-B-H-L-M collaboration, N.C. to be published
9. A-B-B-B-H-L-M collaboration, Phys. Rev. to be published.
10. CHEW and LOW, Phys. Rev. 113 1640 1959
11. FERMI, Prog. theoret. Phys. Japan 5 570 1950; Phys. Rev. 92 452 1953; Phys. Rev. 93 1435 1964.
12. LINDENBAUM and STERNHEIMER, Phys. Rev. 105 1874 1957; Phys. Rev. 123 383 1961.
13. AACHEN, BONN, BIRMINGHAM, HAMBURG, LONDON (IMPERIAL COLLEGE), MUNICH collaboration N.C. 31 485 1964; P.L. 5 153 1963; P.L. 5 209 1963.
14. See for example, reference 1 of BERTANZA et al, Phys. Rev. 130 786 1963; and references 3 and 4 of WANGLER, Ph.D. thesis, University of Wisconsin 1964.
15. CRAWFORD et al, Phys. Rev. 128 368 1962; BALTAY et al, 127 607 1962; FOWLER et al, Bull. Am. Phys. Soc. April 1964.

- 16 FOELSCHE et al, preprint.
- 17 YAMANOOTO et al, Phys. Rev. 134 B383 1964.
- 18 Private communication Dr N. Xuong.
- 19 BERTIANZA et al, P.R.L. 10 176 1963.
- 20 SMITH et al, P.R.L. 10 138 1963.
- 21 HART et al, Phys. Rev. 126 747 1962.
- 22 LEE et al, P.R.L. 12 342 1964.
- 23 GOLDHABER et al, P.R.L. 12 336 1964.
- 24 ALFF et al, P.R.L. 332 1962.
- 25 ABOLINS et al, P.R.L. 11 381 1963; CHUNG et al,  
Siena conference report p. 201 1963, HESS et al, Dubna conference  
1964.
- 26 FOWLER et al, P.R.L. 10 110 1963.
- 27 Proceedings of the 1964 Easter School for Physicists  
CERN 64-13 Vol II p.8.
- 28 DALITZ, Proc. Phys. Soc. (London) A69 527 1956;  
Rev. Mod. Phys. 31 823 1959.
- 29 GOLDHABER et al, P.R.L. 9 330 1962.
- 30 for example; ZEMACH, Phys. Rev. 133 B1201 1964;  
BYERS and FENSTER, P.R.L. 11 52 1963.
- 31 GELLMANN, Phys. Rev. 125 1067 1962; NE'EMAN, Nuc. Phys.  
26 222 1961.
- 32 Les chambres a bulles Francaises au CERN, published in  
L'Onde Electrique, December 1961.

- 33 POWELL, report to D.S.I.R. on "A machine for the analysis of bubble chamber photographs".
- 34 M. IBOTSEN, Ph.D. thesis 1963.
- 35 THRESH; MOORHEAD, CERN report 60-33.  
GRIND; BOCK, GRIND Manual, CERN publication.  
BAKE, SLICE: Post - GRIND manual; CERN publication.  
SUMX; E. MALAMUD, CERN report.
- 36 DRAPER et al, U.C.R.L. memo 347 1961.
- 37 ROSSI, High Energy Physics p.68, p. 13-20.
- 38 F. CAMPAYNE, Ph.D. thesis 1965.
- 39 ROOS, Rev. Mod. Phys. 35 No. 2 1963; ROSENFELD et al,  
U.C.R.L. - 8030 Part 1 June 1964.
- 40 A-B-B-H-L-M collaboratinn, N.C. 31 729 1964.
- 41 GOEBEL, P.R.L. 1 337 1958.
- 42 DRELL, P.R.L. 342 1960; Rev. Mod. Phys. 33 458 1961.
- 43 SALZMAN and SALZMAN, Phys. Rev. 120 599 1960.
- 44 FERRARI and SELLERI, Suppl. del Nuovo Cimento 24 453 1962.
- 45 GOTTFRIED and JACKSON, N.C. 34 735 1964.
- 46 SOPKOVICH, N.C. 26 186 1962; DAR et al P.R.L.  
12 82 1964; P.R.L. 12 511 1964.
- 47 GOTTFRIED and JACKSON, N.C. 33 309 1964; P.L. 8 144 1964.
- 48 JACKSON and PILKUHUN, N.C. 33 906 1964.
- 49 JACKSON, N.C. in press.

- 50 GOTTFRIED, JACKSON and SVENSSON, Paper at the Dubna conference 1964, Abstract V - 7; GOTTFRIED, JACKSON, KEYSER and SVENSSON, to be published.
- 51 JACKSON, preprint to be published in Rev. Mod. Phys.
- 52 SVENSSON, preprint to be published.
- 53 TREIMAN and YANG, P.R.L. 8 140 1962.
- 54 LYNCH et al, P.L. 9 359 1964.
- 55 SAKURAI and STODOLSKY, P.R.L. 11 90 1963.
- 56 PUPPI, Annual Review of Nuclear Science Vol 13 1963.
- 57 GOLDHABER, lecture at a conference on Particle and High Energy Physics at Boulder, Colorado 1964.
- 58 GOLDHABER, LEE and YANG, Phys. Rev. 1125 1958.
- 59 CARMONY et al, P.R.L. 12 254 1964.
- 60 HALPERN, P.R.L. 12 252 1964.
- 61 CHUNG et al, P.R.L. 12 621 1964; DEUTSCHMAN et al, P.L. 12 306 1964.
- 62 BELYAKOV et al, CERN Conference report p. 336 1962.
- 63 Private communication Mr A. Eskryz.
- 64 HAQUE et al, P.L. 10 110 1963.
- 65 HESS et al, U.C.R.L. Report 11898 to be published.

FIGURE CAPTIONS

- Figure 2.1      Flow diagram for the analysis of strange particle events.
- Figure 2.2      The layout of the 4 Gev/c  $\pi^+$  beam; Q represents a magnetic quadropole and BM a bending magnet.
- Figure 2.3      Schematic diagram of the 82 cms. Hydrogen Bubble Chamber with the camera positions and coordinate system.
- Figure 2.4      A diagram to illustrate the quantities which define the  $\pi^+ \rightarrow \mu^+ \rightarrow e^+$  criterion.
- Figure 2.5      A diagram showing the helix reconstructed in THRESH with its parameters.
- Figures 3.1, 3.2 and 3.3      show the y, z and x-coordinates for the apex of the Imperial College strange particle events respectively. In Figure 3.2 the limits of the Fiducial volume are indicated.
- Figures 3.4, 3.5 and 3.6      show distributions for the fitted beam momentum, dip angle and azimuthal angle respectively for Imperial College events.
- Figure 3.7      Ionization curves for some elementary particles in liquid Hydrogen.
- Figures 3.8 and 3.9      show the probability of ( $\chi^2$ ) distributions for all  $\lambda$  and  $K^0$  V-fits.

- Figures 3.10 and 3.11 show the probability of ( $\chi^2$ ) distributions for the single and multivertex fits of the unambiguous 201 events.
- Figure 3.12 The normalised distributions for the probability of ( $\chi^2$ ) of all  $\lambda$  and  $K^0$  V-fits.
- Figures 3.13 and 4.14 show the distributions for the cosine of the production angle of the proton and  $\pi^+$  in the  $\lambda$  and  $K^0$  centre of masses.
- Figures 3.15 and 3.16 show the lifetimes plots for the  $\lambda$  and  $K^0$ ;  $\log_e N'$  plotted against  $L/p$ .
- Figures 3.17, 3.18 and 3.19 show ideograms for the missing mass squared for the reactions  $\pi^+ p \rightarrow K^+ p K^0 \pi^0$ ,  $\pi^+ p \rightarrow K^+ \pi^+ \lambda \pi^0$  and  $\pi^+ p \rightarrow p \pi^+ K^0 K^0$  respectively.
- Figures 3.20, 3.21 and 3.22 show ideograms for the missing mass squared for the reactions  $\pi^+ p \rightarrow \pi^+ \pi^+ \lambda K^0$  ( $\lambda$  seen);  $\pi^+ p \rightarrow K^+ \pi^+ K^0 n$  and  $\pi^+ p \rightarrow \pi^+ \pi^+ \lambda K^0$  ( $K^0$  seen).
- Figures 4.1, 4.2 and 4.3 show the Probability of ( $\chi^2$ ) distributions for all  $V^+$  fits, 210 and 410 single vertex and 210 and 410 Multivertex fits respectively.
- Figures 4.4 and 4.5 show the distributions for the cosine of the proton or  $\pi^+$  production angle in the  $\Sigma^+$  centre of mass for the decays  $\Sigma^+ \rightarrow p + \pi^0$  and  $\Sigma^+ \rightarrow \pi^+ + n$ .

- Figure 4.6      The distribution for the cosine of the  $\mu^\pm$  or  $\pi^\pm$  production angle in the  $K^\pm$  centre of mass for the decays  $K^\pm \rightarrow \mu^\pm + J$ ;  $K^\pm \rightarrow \pi^\pm + \pi^0$ .
- Figures 4.7, 4.8, 4.9 and 4.10      show the distributions of the angle  $\chi$  for decays with  $0^\circ \leq \theta \leq 6^\circ$ ,  $6^\circ \leq \theta \leq 10^\circ$ ,  $10^\circ \leq \theta \leq 20^\circ$ ,  $20^\circ \leq \theta \leq 180^\circ$  respectively.
- Figures 4.11 and 4.12      show the Lifetime plots for the decay modes  $\Sigma^+ \rightarrow p + \pi^0$  and  $\Sigma^+ \rightarrow n + \pi^+$ .
- Figures 4.13, 4.14 and 4.15      show the ideograms of the missing mass squared for the reactions  $\pi^+ p \rightarrow \Sigma^+ K^+ \pi^0$ ,  $\pi^+ p \rightarrow \Sigma^+ \pi^+ K^0$  and  $\pi^+ p \rightarrow K^+ p K^0$  (210 events only) respectively.
- Figures 4.16, 4.17 and 4.18      show the ideograms of the missing mass squared for the reactions  $\pi^+ p \rightarrow \Sigma^\pm K^+ \pi^+ \pi^\mp$ ,  $\pi^+ p \rightarrow \Sigma^\pm K^+ \pi^+ \pi^\mp \pi^0$  and  $\pi^+ p \rightarrow \Sigma^\pm \pi^+ \pi^+ \pi^\mp K^0$  respectively.
- Figure 6.1      The  $\lambda\pi^+$  effective mass distribution for the reaction  $\pi^+ p \rightarrow K^+ \pi^+ \lambda \pi^0$ .
- Figure 6.2      The  $Y_1^{*+}$  (1385) centre of mass production angle.
- Figure 6.3      Peripheral diagram for the reaction  $\pi^+ p \rightarrow K^*(888) + Y_1^{*+}(1385)$ .
- Figure 6.4      The scatter diagram of the  $\lambda\pi^+$  and  $K^+ \pi^0$  effective masses.
- Figure 6.5      The  $K^+ \pi^0$  effective mass distribution. The shaded area represents those events for which  $\lambda\pi^+$  lies in the  $Y_1^{*+}(1385)$ .

- Figure 6.6 and 6.7 show the  $\lambda\pi^+\pi^0$  effective mass distributions for all events and for those where  $\lambda\pi^+$  lies in the  $Y_1^*$  (1385).
- Figure 6.8 The centre of mass production angle for  $Y^{**}$ .
- Figures 6.9, 6.10, 6.11 and 6.12 show the distributions for the cosine of the centre of mass production angle for the  $\lambda$ ,  $K^+$ ,  $\pi^+$  and  $\pi^0$  respectively for the reaction  $\pi^+p \rightarrow K^+\pi^+\lambda\pi^0$ .
- Figure 6.13 The scatter diagram of the  $\lambda\pi_b^+$  and  $K^0\pi_a^+$  effective masses for the reaction  $\pi^+p \rightarrow \pi^+\pi^+\lambda K^0$ .
- Figures 6.14 and 6.15 show the effective mass distributions for the  $K^0\pi_a^+$  and  $\lambda\pi_b^+$  combinations (shaded for those events where  $K^0\pi_a^+$  lies in the  $K^*$ ).
- Figures 6.16, 6.17, 6.18 and 6.19 show the cosine of the centre of mass production angle for the  $K^*$ ,  $\lambda$ ,  $K^0$  and  $\pi^+$  respectively for the reaction  $\pi^+p \rightarrow \pi^+\pi^+\lambda K^0$ .
- Figure 6.20 The scatter diagram for the  $p\pi^+$  and  $K^0\bar{K}^0$  effective masses in the reaction  $\pi^+p \rightarrow p\pi^+K^0\bar{K}^0$ .
- Figures 6.21 and 6.22 show the effective mass distributions for the  $p\pi^+$  and  $K^0\bar{K}^0$  combinations.
- Figures 6.23, 6.24 and 6.25 show the cosine of the centre of mass production angle for the  $\pi^+$ ,  $p$  and  $K^0$  respectively in the reaction  $\pi^+p \rightarrow p\pi^+K^0\bar{K}^0$ .

- Figures 6.26 and 6.27 show the scatter diagrams for the  $K\pi$  and  $\Sigma\pi$  effective masses for the reactions  $\pi^+p \rightarrow \Sigma^+\pi^+K^0$  and  $\pi^+p \rightarrow \Sigma^+K^+\pi^0$ .
- Figures 6.28 and 6.29 show the  $K\pi$  effective mass distributions for the reactions  $\pi^+p \rightarrow \Sigma^+\pi^+K^0$  and  $\pi^+p \rightarrow \Sigma^+K^+\pi^0$ .
- Figures 6.30 and 6.31 show the cosine of the centre of mass production angle for the  $\Sigma^+$  in the reactions  $\pi^+p \rightarrow \Sigma^+\pi^+K^0$  and  $\pi^+p \rightarrow \Sigma^+K^+\pi^0$ .
- Figures 6.32 and 6.34 show the cosine of the centre of mass production angle for the  $K^0$  in the reactions  $\pi^+p \rightarrow \Sigma^+\pi^+K^0$  and  $\pi^+p \rightarrow \Sigma^+K^+\pi^0$ .
- Figures 6.33 and 6.35 show the cosine of the centre of mass production angle for the  $\pi^0$  in the reactions  $\pi^+p \rightarrow \Sigma^+\pi^+K^0$  and  $\pi^+p \rightarrow \Sigma^+K^+\pi^0$ .
- Figure 6.36 The peripheral diagram for the reaction  $\pi^+p \rightarrow \Sigma^+ + K^*$
- Figure 6.37 The vectors required to define  $\cos \theta$  and  $\cos \phi$ .
- Figures 6.38 and 6.39 show the distributions for  $\cos \theta$  and  $\phi$  for  $K^*$  production in the reaction  $\pi^+p \rightarrow \Sigma^+ + K^*$ .
- Figures 7.1 and 7.2 show the  $p\pi^+$  and  $\pi^+\pi^-$  effective mass distributions for the reaction  $\pi^+p \rightarrow p\pi^+\pi^+\pi^-$ .
- Figure 7.3 Scatter diagram for the  $p\pi_a^+$  and  $\pi_b^+\pi^-$  effective masses for  $\Delta^2 (p/p\pi_a^+) < 0.3 \text{ Gev}^2$ .

- Figure 7.4      The distribution for the  $\pi_b^+ \pi^-$  effective mass  
for those events where  $1.16 \leq M(p \pi_a^+) \leq 1.36$  Gev.
- Figure 7.5  
and 7.6      show diagrams giving the vectors used to define  
 $\cos \theta$  and  $\cos \phi$  for the decays  $\rho^0 \rightarrow \pi_b^+ \pi^-$  and  
 $N^{*++} \rightarrow p \pi_a^+$ .
- Figure 7.7      The peripheral diagram for the reaction  
 $\pi_p^+ \rightarrow N^{*++} + \rho^0$ .
- Figure 7.8  
and 7.9      show the projections from Figure 7.3 for the  
 $p \pi_a^+$  effective masses for which  $0.66 < M(\pi_b^+ \pi^-)$   
 $< 0.86$  and the  $\pi_b^+ \pi^-$  effective masses for which  
 $1.16 < M(p \pi_a^+) < 1.36$ .
- Figures 7.10  
7.12      show the distributions for  $\cos \theta$  for the decays  
 $\rho^0 \rightarrow \pi_b^+ \pi^-$  and  $N^{*++} \rightarrow p \pi_a^+$  compared with the  
theoretical expression.
- Figures 7.11  
and 7.13      show the distributions for  $\phi$  for the decays  
 $\rho^0 \rightarrow \pi_b^+ \pi^-$  and  $N^{*++} \rightarrow p \pi_a^+$  compared with the  
theoretical expression.
- Figures 7.14,  
7.15 and 7.16      show the distributions for  $\cos \theta_{\pi_b^+}$  for the  
three intervals of  $\cos \theta_p$ ;  $+0.4 \leq \cos \theta_p \leq +1.0$ ;  
 $-0.4 \leq \cos \theta_p \leq +0.4$ ;  $-1.0 \leq \cos \theta_p \leq -0.4$ .
- Figures 7.17,  
7.18 and 7.19      show the distributions for  $\cos \theta_p$  for the three  
intervals of  $\cos \theta_{\pi_b^+}$ .  $-1.0 \leq \cos \theta_{\pi_b^+} \leq -0.4$ ;  
 $-0.4 \leq \cos \theta_{\pi_b^+} \leq +0.4$ ;  $+0.4 \leq \cos \theta_{\pi_b^+} \leq +1.0$ .

- Figures 7.20 and 7.21 show the  $p \pi^+$  and  $\pi^+ \pi^- \pi^0$  effective mass distributions for the reaction  $\pi^+ p \rightarrow p \pi^+ \pi^- \pi^0$ .
- Figure 7.22 The cartesian coordinate system defining  $\cos \theta$  and  $\phi$ .
- Figure 7.23 The peripheral diagram for the reaction  $\pi^+ p \rightarrow N^{*++} + \omega^0$ .
- Figures 7.24 and 7.25 show diagrams giving the vectors required to define  $\cos \theta$  and  $\cos \phi$  for the decays  $\omega^0 \rightarrow \pi_b^+ \pi^- \pi^0$  and  $N^{*++} \rightarrow p \pi_a^+$ .
- Figure 7.26 The scatter diagram for the  $p \pi_a^+$  and  $\pi_b^+ \pi^- \pi^0$  effective masses for  $\Delta^2 (p/p \pi_a^+) \leq 0.6 \text{ GeV}^2$ .
- Figures 7.27 and 7.28 show the projections from Figure 7.26 for the  $p \pi_a^+$  effective mass where  $0.74 < M(\pi_b^+ \pi^- \pi^0) < 0.84 \text{ GeV}$  and the  $\pi_b^+ \pi^- \pi^0$  effective mass where  $1.16 < M(p \pi_a^+) < 1.36$ .
- Figures 7.29 and 7.31 show the distributions of  $\cos \theta$  for the decays  $\omega^0 \rightarrow \pi_b^+ \pi^- \pi^0$  and  $N^{*++} \rightarrow p \pi_a^+$  compared with the theoretical expressions.
- Figures 7.30 and 7.32 show the distributions of  $\phi$  for the decays  $\omega^0 \rightarrow \pi_b^+ \pi^- \pi^0$  and  $N^{*++} \rightarrow p \pi_a^+$  compared with the theoretical expressions.
- Figures 7.33 and 7.34 show the distributions of the four momentum transfer for the reaction  $\pi^+ p \rightarrow N^{*++} + \omega^0$  and  $\pi^+ p \rightarrow N^{*++} + \omega^0$ .

- Figures 7.35 and 7.36 show the variations of the matrix elements of the  $\rho^0$  and  $N^{*++}$  respectively with  $\Delta^2$  for the reaction  $\pi^+ p \rightarrow N^{*++}$  and  $\rho^0$ .
- Figures 7.37 and 7.38 show the variations of the matrix elements of the  $\omega^0$  and  $N^{*++}$  respectively with  $\Delta^2$  for the reaction  $\pi^+ p \rightarrow N^{*++} + \omega^0$ .
- Figure 8.1 The scatter diagram for the  $p \pi_a^+$  and  $\pi_b^+ \pi^- \pi^0$  effective masses for the reaction  $\pi^+ p \rightarrow p \pi^+ \pi^- \pi^0$ .
- Figures 8.2 and 8.3 show the  $\pi_a^+ \pi_b^+ \pi^- \pi^0$  effective mass distributions for events with at least one  $\omega^0$  and for those with both  $\omega^0$  and  $N^{*++}$  production respectively.
- Figures 8.4, 8.5 and 8.6 show the distributions of  $\cos \theta$  for the events in regions A, B and C in Figure 8.3. The shaded area in B represents the distribution for a normalised background.
- Figure 8.7 The  $\cos \theta$  distribution for the Buddha compared with a  $\sin^2 \theta$  distribution.
- Figures 8.8 and 8.9 show the distributions for the  $\pi^+ \pi^0$  effective mass for the reactions  $\pi^+ p \rightarrow p \pi^+ \pi^0$  and  $\pi^- p \rightarrow p \pi^- \pi^0$  compared with a phase space normalised to all events outside the  $\rho^+$  region.
- Figure 8.10 The  $K\bar{K}$  effective mass distributions for the three reactions  $\pi^+ p \rightarrow p K^+ K_1^0 \pi^0$ ,  $\pi^+ p \rightarrow K^+ \pi^+ K_1^0 n$  and

$\pi^+ p \rightarrow p \pi^+ K_1^0 K_2^0$ ; the shaded area represents those events from the last reaction.

Figure 8.11 The  $K^+ K_1^0$  effective mass distributions for the reactions  $\pi^+ p \rightarrow K^+ p K_1^0$ ; the phase space normalised to events outside the  $A_2$  region.

Figure 8.12 The cosine of the centre of mass production angle of the proton for the reaction  $\pi^+ p \rightarrow K^+ p K_1^0$ .